Modification of a High-Temperature Electrochemical Testing Station and Experimental Method Development for Solid Oxide Electrolysis Cell Anode Analysis

By

Graeme Craig Clancy

A thesis submitted to the

Department of Chemical Engineering

in conformity with the requirements for

the degree of Master of Applied Science

Queen's University

Kingston, Ontario, Canada

January 2016

Abstract

A method to fabricate solid oxide electrolysis cell (SOEC) anodes in a controlled process has been developed. Adjustment of deposition rate was found to alter the anode porosity and particle size distribution. A solid oxide fuel cell (SOFC) testing system was enhanced to complete steam electrolysis testing of the cells with prepared anodes.

To prepare anodes of desirable morphology and uniform thickness the effect of spraying parameters on anode morphology were studied. Sonication of the anode inks was found to reduce particle agglomerations in the ink dispersion. A technique for obtaining and analyzing SEM cross sections of SOECs was developed to study prepared anodes. Investigation of sprayed anodes revealed that the porosity decreased as the deposition rate was increased. Using ImageJ analysis software particle size distributions of prepared anodes were determined. Anodes deposited at higher deposition rates were seen to have larger particle sizes. A greater anode deposition rate increased the likelihood of particle settling and agglomeration, leading to the decreased porosity and increased particle size in the anodes.

A membrane humidifier was developed and tested to steadily supply steam to the electrolysis cell, the first such humidifier combined with a ProbotStat™ testing rig. Using the modified testing system, a testing method for SOEC analysis was developed. The process for producing polarization curves was studied to determine the desired testing conditions. During testing hysteresis between increasing and decreasing polarization curves, and anode conditioning during constant current electrolysis were seen for some cells. The appearance or absence of both phenomena were seen to be connected.

Acknowledgments

I would like to thank my supervisor, Dr. Brant Peppley, for his tremendous guidance and technical support during my time with FCRC. The knowledge of electrochemistry and technical writing he has shared with me has been vastly helpful during my degree, and will continue to serve me throughout my career.

In addition I would like acknowledge the assistance of the FCRC community and the Chemical Engineering Department at Queen's for aiding in my experimental work as well as encouraging curiosity and the pursuit of knowledge. In particular I would like to thank Dr. Jon Pharoah, for his thought provoking questions; Dr.Wojtek Halliop, for sharing his immense experience with electrochemical systems; and Ela Halliop for her guidance in experimental systems. In addition I would like to acknowledge the insightful discussions with numerous colleagues for enhancing my learning experience at Queen's.

I would like to thank Queen's University and particularly the members of Queen's University Outdoors Club for providing a positive community for me to complete my studies. I would like to acknowledge the Ontario China Research and Innovation Fund (OCRIF) for providing funding to allow the completion of my degree. Finally I would like to thank my family for their constant love and support during my graduate degree.

Table of Contents

List of Figures

Nomenclature

Roman

a_i	Activity of species i [-]
d_{pore}	Pore diameter [m]
$D_{i,j}$	Molecular diffusivity of species i in species j [$cm^2\ s^{-1}$]
$D_{i,j}^{Bos}$	Bosanquet diffusivity of species i in species j [$cm^2\ s^{-1}$]
E_N	Reversible Nernst potential [V]
E_A	Applied potential [V]
E°	Standard state reversible voltage [V]
E(z)	Local potential [V]
F	Faradays constant [$C\ mol^{-1}$]
ΔG	Change in Gibbs free energy of a reaction [$J\ mol^{-1}$]
ΔH	Change in enthalpy of a reaction [$J\ mol^{-1}$]
I	Current [A]
i	Current density [$A\ cm^{-2}$]
i_0	Exchange current density [$A\ cm^{-2}$]
k_{ox}	Kinetic constant of oxidation reaction [$m\ mol^{-1}\ s^{-1}$]
k_{red}	Kinetic constant of reduction reaction [$m\ mol^{-1}\ s^{-1}$]
Kn	Knudsen number [-]
M_i	Molar mass of species i [$kg\ mol^{-1}$]
n	Number of participating in a reaction [-]
$\mathcal{n}$	Electrode Polarization [V]
O_{ads}	Number of adsorbed oxygen atoms
p_i	Partial pressure of species i [pa]
P	Pressure [pa]
p_o	Standard atmospheric pressure [pa]
R	Gas constant [$J\ K^{-1}\ mol^{-1}$]
R_{ele}	Cells total electronic resistance [Ω]
R_{ion}	Cells total ionic resistance [Ω]
ΔS	Change in entropy of a reaction [$J\ K^{-1}\ mol^{-1}$]
S_{ads}	Number of available adsorption sites [-]
T	Temperature [K]
V_{Total}	Total electrode volume [m]
V_{Solid}	Solid electrode volume [m]

Greek

α_{ox}	Symmetry factor of the oxidation reaction [-]
α_{red}	Symmetry factor of reduction reaction [-]
ε	Porosity [-]
η_{act}	Activation overpotential [V]
η_{conc}	Concentration overpotential [V]
η_{ohmic}	Ohmic overpotential [V]
$\bar{\lambda}$	Mean free path of a particle [m]
μ_i	Chemical potential of species i [V]
ρ	Density [kg m^{-3}]
σ_{e^-}	Electronic conductivity [m^{-2}]
$\sigma_{O^{2-}}$	Ionic conductivity [m^{-2}]
φ_e	Electronic potential [V]
φ_i	Ionic potential [V]

Acronyms

AWS	Adjustable Watershed Segmentation
BEV	Battery electric vehicle
BL	Baseline (ink)
BSED	Back scattering electron detector
CCL	Current collecting layer
DAQ	Data acquisition unit
DI	Dilute (ink)
EIS	Electrical impedance spectroscopy
FCEV	Fuel cell electric vehicle
ICE	Internal combustion engine
IEA	International energy agency
IPA	Isopropyl alcohol
LSM	Lanthanum strontium magnate
NC	NextCell
OCV	Open circuit voltage
PdI	Polydispersity Index
PEM	Polymer electrolyte membrane
PVP	Poly-Vinyl Pyrrolidone
SEM	Scanning Electron Microscopy
SOEC	Solid oxide electrolysis cell
SOFC	Solid oxide fuel cell
TEC	Thermal expansion coefficient
TPB	Triple phase boundary
YSZ	Yttria stabilized zirconia

Chapter 1: Introduction

1.1: Motivation

The exceptional quality of life that the developed world enjoys is due in large part to our access to energy. Life expectancy has been correlated to energy use per capita as well as carbon emissions at the national level [1, 2]. As nations around the world become more developed their citizens are using more energy. The increase in global energy demand is being met mostly by fossil fuels. Worldwide 81.4% of energy came from combusting fossil fuels (coal, 29.0%; oil, 31.4%; and natural gas, 21.3%) in 2012 according to the International Energy Agency (IEA) [3]. The global population's insatiable need for energy supplied by carbon dioxide (CO_2) producing fossil fuels has increased the atmospheric level of CO_2 to levels that are disrupting our planetary heat balance. The greenhouse gas effect (caused by CO_2 and other insulating gases) is leading to warming of the earth's average temperature and disruptions of normal climatic patterns [4]. The energy produced from fossil fuel combustion is used mainly for heating, transportation, and electricity production [3]. As a means of reducing the dependence of the transportation sector on fossil fuels alternatives to the internal combustion engine (ICE) are becoming more common. Promising alternatives include fuel cell electric vehicles (FCEVs) and battery electric vehicles (BEVs). FCEVs operate by converting hydrogen and oxygen into electrical energy to power a vehicle. Unfortunately, the majority (95%) of hydrogen is produced from fossil fuels: by steam methane reforming, as a fraction during petroleum refining, or through coal gasification [5].

BEVs store electricity supplied from an electricity grid in a battery onboard to power the car. Globally electricity is produced using fossil fuels 67.9% of the time, limiting BEVs CO_2 emissions reduction compared to ICE [6]. Recently the fraction of electricity produced from fossil fuels has been falling due to continuously improving technologies for low CO_2 emitting electricity sources (solar PV, solar thermal, wind, *etc.*). These so called non-hydroelectric renewable energy sources, offering lower CO_2

emissions than fossil thermal plants, are dependent on the local weather patterns and are therefore variable. Unpredictable supply makes it difficult for electricity grid operators to match energy supply and demand. When supply is greater than demand due to greater than expected sun or wind, or demand is lower than expected it is beneficial to be able to store the electricity to be used later. Electrical energy storage on the grid can also help control the quality of power (voltage and frequency control), and reduce redundant transmission and distribution infrastructure used only for peak hours [6].

A promising method for storing energy is in the form of hydrogen gas. Hydrogen can be produced from electrocatalytically splitting water in an electrolysis process. Storing energy in the form of hydrogen allows for a greater storage capacity than traditional solid state batteries, which can be stored for a longer time (months as opposed to days) [7]. This stored hydrogen can be used later in a hydrogen fuel cell to produce electricity for the grid or used in a FCEV for transportation.

Production of hydrogen by water electrolysis using electricity from renewable resources provides a method for storing excess electricity and a method of producing hydrogen for FCEV with low CO_2 emissions. Two common methods for electrolysing water to produce hydrogen are polymer electrolyte membrane (PEM) electrolysis and solid oxide electrolysis (SOE). PEM electrolysis operates at lower temperatures and requires noble metals, such as platinum, to act as a catalyst. Solid oxide electrolysis cells operate at a higher temperature and utilize less expensive rare earth metals to act as a catalyst such as scandium, yttrium, and lanthanum. Operation at higher temperatures also gives SOE greater electrical efficiency than PEM electrolysis [8]. The greater heat inputs required for SOE make it best suited for stationary application, located near a source of industrial waste heat. For these reasons the use of SOE is seen as an excellent technology for large scale stationary production of hydrogen gas.

1.2: Solid Oxide Electrolysis Background

Electrolysis of water was first demonstrated in 1789 by Dieman and van Troojtwijk [9]. Since its first demonstration electrolysis has not become a common method for producing hydrogen. The ubiquitous

use of fossil fuels and associated well developed infrastructure, has helped methods such as steam methane reforming to become the most widely used for hydrogen production. Only recently has water electrolysis gained considerable attention. Improvements to fuel cell technology (PEM and solid oxide) have benefited electrolysis research. Electrolysis cells are similar, though not identical, to a fuel cell operating in reverse (applying a voltage and producing hydrogen opposed to using hydrogen to produce a voltage).

SOECs and PEM electrolysis cells each offer their own advantages and disadvantages. Solid oxide electrolysers operate at high temperatures, typically 600–900^{0}C, therefore requiring less electrical energy to split a water molecule compared to lower temperature PEM cells. The reduction in electrical energy demand is defined by the Gibbs free energy equation,

$$\Delta G = \Delta H - T\,\Delta S \tag{1.1}$$

where ΔG is the Gibbs free energy, which is proportional to electrical demand; ΔH is the enthalpy change; T is the temperature; and ΔS is the entropy change. The enthalpy change is the differences between the enthalpy of formation of the reactants and the products, likewise for the entropy change. PEM electrolysis cells operate from 0-80°C and require more electrical energy per unit of hydrogen produced compared to SOECs. A difference in operating temperature from 25°C to 1000°C represents a theoretical reduction in electrical demand (ΔG decrease) of 25.1% [10]. A graphical representation of the reduction in theoretically required Gibbs energy as a function of temperature can be seen in Figure 1.1. An additional opportunity provided by SOECs is the possibility of electrolytically splitting other molecules, carbon dioxide being of particular interest. The electrolysis of carbon dioxide and water produces carbon monoxide and hydrogen or synthesis gas. This mixture can be used in the Fischer-Tropsch process to produce a variety of value added chemicals.

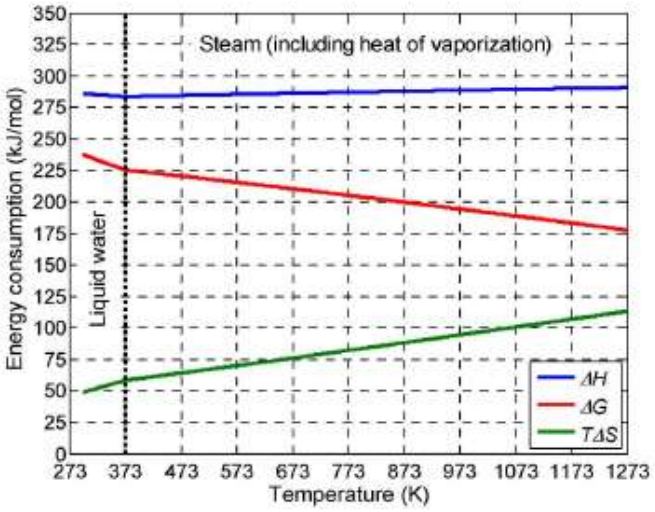

Figure 1.1: Theoretical energy consumption for the electrolysis of water as a function of temperature at a pressure of 1 atm [10].

The increased temperature responsible for SOECs improved electrical efficiency requires considerations of issues that are not of concern for lower temperature systems. Such high temperatures demand specialized materials and cell design to provide the electrochemical transport functions of an electrolysis cell while maintaining stability (mechanical and performance). Factors including thermal degradation, thermal expansion coefficients (TEC), transport coefficients at high temperatures, degradation under oxidizing and reducing conditions, and the relation of all of these factors between components must be considered for optimal cell performance.

To facilitate and separate the oxidation and reduction reactions occurring at the electrodes, a two electrode configuration separated by a dense electrolyte is used for SOECs. The key working components of each cell are the cathode (hydrogen electrode), electrolyte, and anode (oxygen electrode). Cells may have additional functional layers including current collecting layers (CCLs), positioned outside of the cathode and anode, acting as support layers and distributing electrons. SOECs may also have inter-diffusion layers located between the anode or cathode and the electrolyte, preventing undesired diffusion of cations [11-14]. A diagram of the three working components in a solid oxide cell in electrolysis operation feed with steam is shown in Figure 1.2.

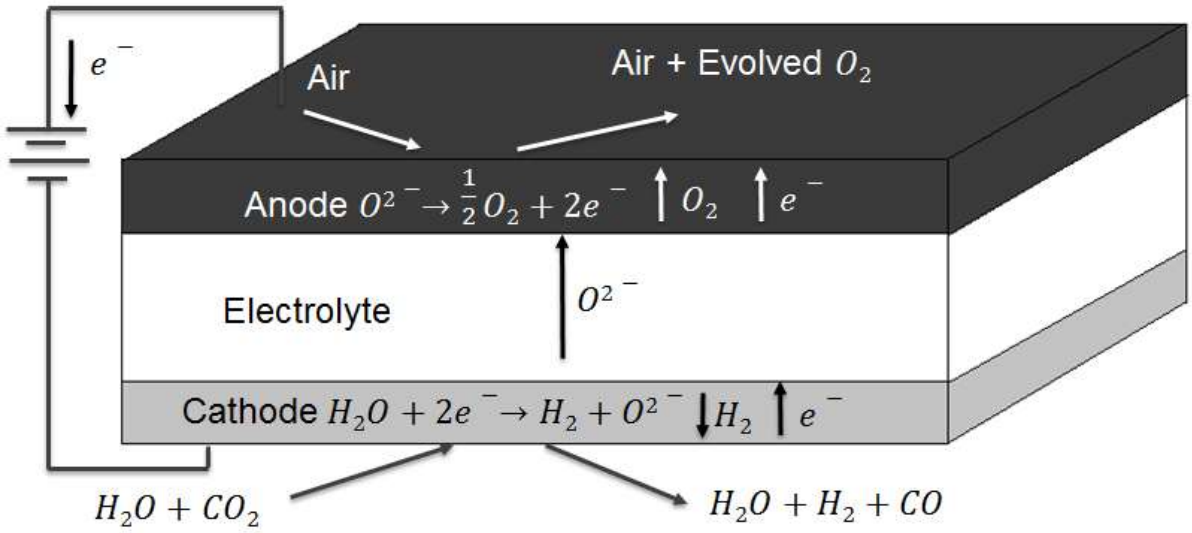

Figure 1.2: Schematic of solid oxide cell during water electrolysis operation.

In electrolysis operation a voltage is applied between the cathode and the anode, steam and a sweep gas are supplied to the cathode and anode respectively. Each mole of steam reduced produces a mole of hydrogen gas (H_2) and a mole oxygen ions (O^{2-}) by the addition of two moles of electrons (e^-). The evolved hydrogen and unconverted steam are carried away by a sweep gas, usually nitrogen with some hydrogen. The hydrogen in the sweep gas prevents oxidation of the cathode (often containing nickel). The O^{2-} ions are transported through the cathode and the electrolyte layer into the anode. In the anode the O^{2-} ions are oxidized and lose two electrons each to form oxygen gas (O_2) which is removed by a sweep gas, usually air. The overall reaction for the SOEC is split into two half-cell, cathode and anode, reactions seen in equations 1.2 and 1.3 respectively.

$$2H_2O + 4e^- \rightarrow 2H_2 + 2O^{2-} \quad (1.2)$$

$$2O^{2-} \rightarrow O_2 + 4e^- \quad (1.3)$$

If H_2 is present at the fuel electrode, O_2 is present at the oxygen electrode, and no voltage is applied, while at operating temperature (above 600 °C) the reverse of these half-cell reactions will occur and the cell will function as a fuel cell. Without a voltage applied to the cell, it will produce the reversible Nernst potential according to the Nernst equation (equation 1.4). The reversible potential is dependent on

temperature of the cell and the partial pressure of the products and reactants. The partial pressure of oxygen in this equation is raised to the power of a half because the stoichiometric ratio of oxygen to hydrogen production is one half.

$$E_n = E^0 - \left(\frac{RT}{nF}\right) \ln\left(\frac{a_{products}}{a_{reactants}}\right) \tag{1.4}$$

$$a_i = \frac{p_i}{P_o} \tag{1.5}$$

$$E_n = E^0 - \left(\frac{RT}{2F}\right) \ln\left(\frac{p_{O_2}^{0.5}\, p_{H_2}}{p_{H_2O}}\right) \tag{1.6}$$

Where $E°$ is the standard reaction potential, n is the number of electrons participating in the reaction, F is Faraday's constant, a is the activity of a species, p_i is the partial pressure of species i, and p_o is the total pressure. With the assumption that the gases in a SOEC act ideally, the activities are replaced with the partial pressures over the total pressure as seen in equation 1.5. In the case of electrolysis operation the consumption of reactants and formation of products is controlled by the amount of current supplied. The production and consumption rates can be found using Faraday's Law, equation 1.7. This calculation assumes that all of the electrons supplied are used for the reduction of water and oxygen evolution (100 % Faradaic efficiency).

$$\frac{dN}{dt} = \frac{I}{nF} \tag{1.7}$$

In this equation dN/dt is the time change of molar rate (consumption or production) of a species, and I is the current applied. For the reduction of water n = 2, since two electrons are needed to reduce each water molecule. This reduction produces one hydrogen molecule and one oxygen ion. For oxygen evolution n = 4, since four electrons are released in the formation of one oxygen molecule from two oxygen ions. A higher applied current during electrolysis will increase the reaction rate as well as increase the voltage. The increase in voltage is caused by a combination of activation losses, from the two half-cell reactions, and ohmic losses, mainly from the resistance in the electrolyte.

The charge transfer steps at both the cathode and anode occur at the triple phase boundary (TPB) [15]. This is the location where all three reacting species; ions, electrons, and gas can react. The efficient transport of each species to or from the TPB significantly affects the performance of the cell [16-19]. This will be examined in detail in Section 2.2: Species Transport. The microstructure of the electrodes is a strong determinant of species transport. The control and study of this microstructure is therefore an area of intense interest in the solid oxide electrolysis field. Including studies investigating the effect of; particle size on performance [15], sintering temperature on microstructure and performance [18], and the effect of TPB density and ionic conductivity on performance [19].

A single SOEC is operated using a voltage lower than what is typically available, in the order of 1 volt. To use a more common voltage SOECs are connected in series, in a stack configuration. When testing processes within a SOEC electrode a button cell scale are generally tested first (a button cell is a circular cell 20-25 mm in diameter). Followed by testing of a larger planner cell (up to 100 x 100 mm), and then stacks of planner cells. The work presented in this thesis has been completed on electrolyte supported button cells. The electrolyte diameter of the cells was 20 mm and electrodes diameters (active cell area) were 13 mm.

1.3: Thesis Objectives

The goal of this thesis is to gain an understanding of the processes leading to delamination of solid oxide electrolysis cell anodes. To gain this understanding a detailed method for preparing anodes with uniform structures must be established and a stable and reliable method for testing cells with prepared anodes must be designed. To understand the effect of electrode morphology on cell performance this work aims to develop a method for controlling the morphological characteristics of an anode. Understanding the fundamentals of the transport and how they are affected by adjustments to cell morphology will allow for the optimisation of SOEC anodes.

1.4: Thesis Structure

This thesis will begin with an examination of the literature on SOECs focusing on the oxygen electrode. The materials and preparation methods for electrodes will be discussed first. Followed by a review of the electrochemical reactions and transport in the anode. The various methods for testing SOECs will then be outlined.

Based on the findings from the literature electrodes prepared using a pressure assisted spray deposition method will be presented in Chapter 3. This deposition method has been mastered to produce electrodes with uniform and controlled structures. The parameters of greatest importance for the production of electrodes with the desired morphology will be explained along with the effects of varying deposition rate. The results of the electrochemical testing used to study the prepared anodes will be discussed Chapter 4. This chapter will examine the effect of the anode morphologies on the electrochemical performance of the cells.

1.5: References

[1] Pielke R. Roger Pielke Jr.'s Blog: Graph of the Day: Life Expectancy vs. Energy Use [Internet]. [cited 2015 Aug 30]. Available from: http://rogerpielkejr.blogspot.ca/2013/02/graph-of-day-life-expectancy-vs-energy.html

[2] Steinberger JK, Roberts JT, Peters GP, Baiocchi G. Pathways of human development and carbon emissions embodied in trade. Nature Clim Change. 2012 Feb;2(2):81–5.

[3] International Energy Agency. Key World Energy Statistics 2014. International Energy Agency; 2014.

[4] Pachauri RK, Allen MR, Barros VR, Broome J, Cramer W, Christ R, et al. Climate Change 2014: Synthesis Report. Contribution of Working Groups I, II and III to the Fifth Assessment Report of the Intergovernmental Panel on Climate Change [Internet]. Pachauri RK, Meyer L, editors. Geneva, Switzerland: IPCC; 2014 [cited 2015 Nov 2]. 151 p. Available from: http://epic.awi.de/37530/

[5] Wang Z, Naterer GF. Integrated fossil fuel and solar thermal systems for hydrogen production and CO2 mitigation. International Journal of Hydrogen Energy. 2014 Sep 3;39(26):14227–33.

[6] Yang Z, Zhang J, Kintner-Meyer M, Lu X, Choi D, Lemmon JP, et al. Electrochemical Energy Storage for Green Grid. Chemical reviews. 2011 Mar;111(5):3577–613.

[7] Dunn B, Kamath H, Tarascon J-M. Electrical Energy Storage for the Grid: A Battery of Choices. Science. 2011 Nov;334(6058):928–35.

[8] Manage MN, Hodgson D, Milligan N, Simons SJR, Brett DJL. A techno-economic appraisal of hydrogen generation and the case for solid oxide electrolyser cells. International Journal of Hydrogen Energy. 2011 May;36(10):5782–96.

[9] Levie R de. The electrolysis of water. Journal of Electroanalytical Chemistry. 1999 Oct;476(1):92–3.

[10] Ursua A, Gandia LM, Sanchis P. Hydrogen Production From Water Electrolysis: Current Status and Future Trends. Proceedings of the IEEE. 2012 Jan;100(2):410–26.

[11] Tietz F, Sebold D, Brisse A, Schefold J. Degradation phenomena in a solid oxide electrolysis cell after 9000 h of operation. J Power Sources. 2013 Feb;223:129-35.

[12] Hjalmarsson P, Sun X, Liu Y-L, Chen M. Influence of the oxygen electrode and inter-diffusion barrier on the degradation of solid oxide electrolysis cells. Journal of Power Sources. 2013 Feb 1;223:349–57.

[13] Ogier T, Bassat JM, Mauvy F, Fourcade S, Grenier JC, Couturier K, et al. Enhanced Performances of Structured Oxygen Electrodes for High Temperature Steam Electrolysis. Fuel Cells. 2013 Aug 1;13(4):536–41.

[14] Kim SJ, Choi GM. Stability of LSCF electrode with GDC interlayer in YSZ-based solid oxide electrolysis cell. Solid State Ionics. 2014 Sep 1;262:303–6.

[15] Gaweł DAW. The Development of a Coupled Physics and Kinetics Model to Computationally Predict the Powder to Power Performance of Solid Oxide Fuel Cell Anode Microstructures. [Kingston, Canada]: Queen's University; 2013.

[16] Moçoteguy P, Brisse A. A review and comprehensive analysis of degradation mechanisms of solid oxide electrolysis cells. International Journal of Hydrogen Energy. 2013 Dec 13;38(36):15887–902.

[17] Virkar AV. Mechanism of oxygen electrode delamination in solid oxide electrolyzer cells. International Journal of Hydrogen Energy. 2010 Sep;35(18):9527–43.

[18] Jørgensen MJ, Primdahl S, Bagger C, Mogensen M. Effect of sintering temperature on microstructure and performance of LSM–YSZ composite cathodes. Solid State Ionics. 2001 Jan 2;139(2):1–11.

[19] Lay-Grindler E, Laurencin J, Delette G, Aicart J, Petitjean M, Dessemond L. Micro modelling of solid oxide electrolysis cell: From performance to durability. International Journal of Hydrogen Energy. 2013 Jun 10;38(17):6917–29.

Chapter 2: Literature Review

The electrolysis of water to produce hydrogen and oxygen in a SOEC is a complex process comprised of many reaction and transport steps. In depth understanding of these reactions and the associated transport mechanisms is necessary for cell optimization. The transport of electrochemical species in a SOEC, a limiting factor in cell performance, has received significant attention [1]. Transport processes in the cell include the electronic, ionic, and gaseous transport within the electrodes as well as the ionic transport at the electrode-electrolyte interfaces and in the electrolyte. The microstructure and composition of the electrodes govern the transport processes in the electrode in combination with the operating conditions (temperature, pressure, gas composition, and gas flowrate). The effect of morphology (particle size, pore size, porosity, and chemical composition) on performance will be examined in Section 2.2. The delamination of the oxygen electrode (anode) is an often reported problem for SOECs. This delamination is detrimental to the performance of the SOEC and is preventing the wide scale adoption of SOE technology, it will be discussed in Section 2.4.

With an understanding of the effects morphology has on reaction and transport processes, cells can be tailored to optimize their performance and durability. It follows that the effect of material preparation and fabrication methods on the microstructure must be well understood and controllable. This chapter will outline common SOEC structures, materials, and preparation methods being employed in the studied literature. Proposed transport processes in SOECs and their relation to electrode microstructure will also be discussed. Followed by the testing methods used to verify these proposed transport processes and study cell performance. Finally the proposed degradation mechanism and potential solutions offered will be presented.

2.1: SOEC Materials and Preparation

The materials chosen to produce a SOEC effect the cell's mechanical strength, ionic and electronic conductivity, and sensitivity to heat fluctuations. SOEC electrodes are prepared by a variety of methods, each offering their own advantages in terms of scalability and morphological control. This section will review options for materials used in SOECs and the procedures commonly used to prepare SOEC electrodes.

2.1.1: SOEC Materials

Materials selection for SOECs requires consideration of physical, chemical, and electrical characteristics. Each of the active cell layers have their own desired properties. The cathode must be stable under reducing conditions and be able to efficiently transport oxygen ions, electrons, hydrogen, and water vapour. The electrolyte must be stable under oxidizing and reducing conditions and should transport only oxygen ions. The anode must be stable under oxidizing conditions and be able to transport oxygen ions, electrons, and oxygen. Furthermore, the cells will be shifting from low temperatures to high temperatures requiring the different components to have well-matched thermal expansions coefficients (TECs). With these characteristics in mind ceramics are a commonly chosen material. Ceramics are relatively inexpensive, stable at high temperatures, and are available with a variety of conductivities including ionic (oxygen ions) and electronic [2, 3].

In order to transfer ions, electrons, and gasses the electrodes of solid oxide cells are manufactured with a porous structure. The ionic and electronic species are transported through the solid phase and gas is transported through the pores. The solid phase is either a two component mixture of ionic and electronic conducting materials or a single mixed ionic electronic conducting (MIEC) material. In the case of a two component mixture, the ratio of pores, ionic, and electronic conducting materials giving the highest TPB length for various particle size distributions has been studied using computational simulations [1].

The materials for SOECs have been adopted from solid oxide fuel cell (SOFC) research, which has received more attention than SOEC research. The most common SOEC cathode is a mixture of electron conducting nickel and ion conducting yttria stabilized zirconia (Ni-YSZ). These components are mixed at Ni:YSZ volume ratios from 40:60 to 60:40 to ensure high conductivity of both species [2-4]. The electrolyte used most often for SOECs is ytrria stabilized zirconia [2, 5-7]. The standard anode for SOECs is a composite of electron conducting lanthanum strontium manganite, and yttria stabilized zirconia (LSM-YSZ). This composite much like that of the cathode is generally mixed in volume ratios from 40:60 to 60:40 LSM:YSZ [1, 8].

In addition to these materials borrowed from SOFC technology, new materials to improve cell performance are being studied. A selection of new materials being investigated and their characteristics are compared to LSM and YSZ in Table 2.1. A composite electrode which has been tested on several occasions is a Lanthanum Strontium Chromite Manganite, and Gadolinium Doped Ceria (LSCM-GDC), it has been used as both an anode and a cathode [9, 10]. This composite is attractive as it has been shown to be stable during cycling from electrolysis to fuel cell mode [9]. The GDC's improved ionic conductivity compared to YSZ (one order of magnitude) is another attractive factor of this composite [11].

An exciting group of materials offering an alternative to composites are mixed ionic and electronic conductors (MIECs). Some examples of MIECs are Lanthanum Strontium Cobalt Ferrite (LSCF), and Lanthanum Nickelate (LNO). In a study by Laguna-Bercero *et al.* [12] a LSCF anode was compared to a LSM anode and found to give a lower area specific resistance (ASR). LNO anodes were also found to have a lower ASR than LSM anodes [13].

Table 2.1: Properties of SOEC materials.

Material	Ionic Conductivity [S cm^{-1}]	Electronic Conductivity [S cm^{-1}]	TEC [10^{-6} K^{-1}]	Advantages	Sources
$Gd_{0.1}Ce_{0.9}O_{1.95}$ (GDC)	0.1 at 800 °C	-	12.04	High ionic conductivity	[10, 11, 14]
$La_{0.75}Sr_{0.25}Cr_{0.5}Mn_{0.5}O_{3-\delta}$ (LSCM)	-	10	10.1	Stable during red-ox cycling	[9-11, 14-16]
$La_{0.9}Sr_{0.1}MnO_{3+\delta}$ (LSM)	10^{-6}-10^{-7} at 900-1000 °C	190 at 900 °C	11.7	High electronic conductivity	[2, 11]
$La_{0.6}Sr_{0.4}Co_{0.2}Fe_{0.8}O_{3-\delta}$ (LSCF)	0.01 at 700 °C	275 at 700 °C	14-17	High ionic + electronic conductivity	[11]
$(ZrO_2)_{0.92}(Y_2O_3)_{0.08}$ (YSZ)	0.01 at 800 °C	-	10.5	Stable during temperature variation	[11]
$La_2NiO_{4+\delta}$ (LNO)	0.017 at 700 °C	40 at 700 °C	13-14.4	High ionic and electronic conductivity	[17, 18]

The performance advantages MIECs offer due to their reduced ASR make them very attractive options for SOECs. Unfortunately, the TECs of MIECs are not well matched with the current electrolyte YSZ. The potential for MIEC to be the dominant material for SOECs is dependent on further study of thermal cycling testing with these materials.

2.1.2: Electrode Preparation

Insuring an electrode's morphology is uniform is essential to study and optimize species transport. The production of electrodes must be a precisely controlled and repeatable process to achieve the desired uniformity. There are a variety of methods for producing electrodes under regulated conditions. In the literature the most widely used methods were screen printing, and spray deposition. Screen printing applies a slurry to a substrate through a mesh screen. The size of mesh can be varied to achieve different electrode thicknesses. The spray deposition method applies an ink by a pressure assisted system, where a carrier gas

delivers the ink to the substrate. The thickness of sprayed electrodes can be adjusted by varying the total time of spraying. In the case of composite electrodes both of these deposition methods use a slurry or ink mixture composed of two active ceramics (ion and electron conducting) and a pore former in an organic dispersant. In some cases the slurry also contains a binder to control the microstructure. Once deposited, electrodes are heated to high temperatures ablating the pore former and sintering the electrode structure. Sintering improves inter-particle and electrolyte-electrode contact.

Along with a diversity of ceramic materials various pore formers and dispersants are used in the preparation of SOEC anodes. Pore former is included to create a pore network for gas transport in the electrode. The amount and type of pore former used in an ink is varied based on the desired porosity and pore structure. The concentration of pore former in a LSM-YSZ composite anode was varied from 5 to 15 weight % in a study by Wang *et al.* giving porosities of 41 to 49% [8]. Studying a variety of pore formers Bo *et al.* [4] tested polymethyl methacrylate (PMMA), potato starch, ammonium oxalate, and ammonium carbonate. PMMA was found to give the most uniform pore size distribution and a high porosity.

The dispersants and binders chosen for slurries are dependent on the application. For example, screen printing requires a more viscous solution than spray deposition; therefore, using a more viscous dispersant. Screen printing methods have used dispersants including terpineol [16, 19] and proprietary organic solvents [23]. Studies using the spray deposition method have used ethanol [1, 20] and acetone [21] as solvents. Binders used for spraying methods include polyvinyl butyral, butyl benzyl phthalate, polyalkylene glycol, and polyvinyl pyrrilidone [1, 20].

After deposition electrodes are heated to high temperatures ranging from 900 °C to 1300 °C to remove pore former and improve inter-particle contact. The temperature that the electrodes are heated to has a major effect on cell performance and has been study in several works [19, 22, 23]. LSM-YSZ composite electrodes deposited by spray deposition and sintered at a range of temperatures were studied by Jørgensen *et al.* [23]. The study analysed physical differences using micrographs and performance differences using electrical impedance spectroscopy (EIS). By studying cells sintered at 1150, 1200, 1250,

and 1300 °C it was found that densification of the electrodes increased with increasing temperature. The cells sintered at lower temperatures had more micro-pores and finer grain sizes giving a greater TPB length than cells with large grains. The increased TPB of lower density electrodes was seen as a lower cell polarization resistances [23]. The polarization resistance of a cell is a measure of the electrodes combined resistance, this will be discussed further in the Section 2.3: SOEC Testing.

It should be acknowledged that the experiments that gave the relationship between sintering temperature, polarization resistance, and electrode densification did contain variability. The thicknesses of the electrode layers were different for all cells, ranging from 28 to 93 μm. To remove the variability of cell thickness and study polarization at lower sintering temperatures, *in-situ* sintering of cells was also completed. Unsintered cells were loaded into the testing apparatus and tested as they were heated. EIS measurements were taken every 100 °C from 600 to 800 °C and every 50 °C until 1050 °C. By using a single cell for all temperature measurements the variability in cell thickness was removed. The data from these tests show that the polarization resistance decreased steadily until between 950 and 1000 °C increasing slightly at 1050 °C. The decrease in polarization resistance with increasing temperature is thought to have been caused by the improved inter-particle and inter-layer contact. The increase seen at temperatures above 1000 °C is attributed to the coarsening of the electrode, reducing the pore volume [23]. In another study screen printed electrodes were sintered at temperatures ranging from 1150 to 1300 °C. The cells were studied visually with SEM and electrochemically with EIS. In agreement with the study by Jørgensen *et al.* it was found that increasing the sintering temperature increased grain size and densification of the electrode. However, the polarization resistance in these cells was found to be lowest at 1200 °C [19]. The variation in results from these studies can be explained by the different deposition method and precursor powders used.

2.2: Electrochemical Reactions and Species Transport

It is imperative that the degradation mechanisms occurring in the SOEC anode are more thoroughly understood to develop improved morphologies increasing cell lifetime and reliability. Any degradation

prevention strategy must be careful not to limit the performance of the SOEC, which is affected by the transport of reacting species. In the current section, the reaction kinetics and their connections to species transport will be discussed, followed by discussion of the gas species transport and the ionic and electronic conduction in the electrode.

2.2.1: Electrode Reaction Kinetics

The evolution of oxygen gas in the electrode occurs according to the anode half reaction. The reactant of the half reaction is one mole of oxygen ions (O^{2-}) and the products are half a mole oxygen gas (O_2) and two moles of electrons (e^-). Figure 2.1 below gives a representation of the microstructure, reaction, and transport in a SOEC.

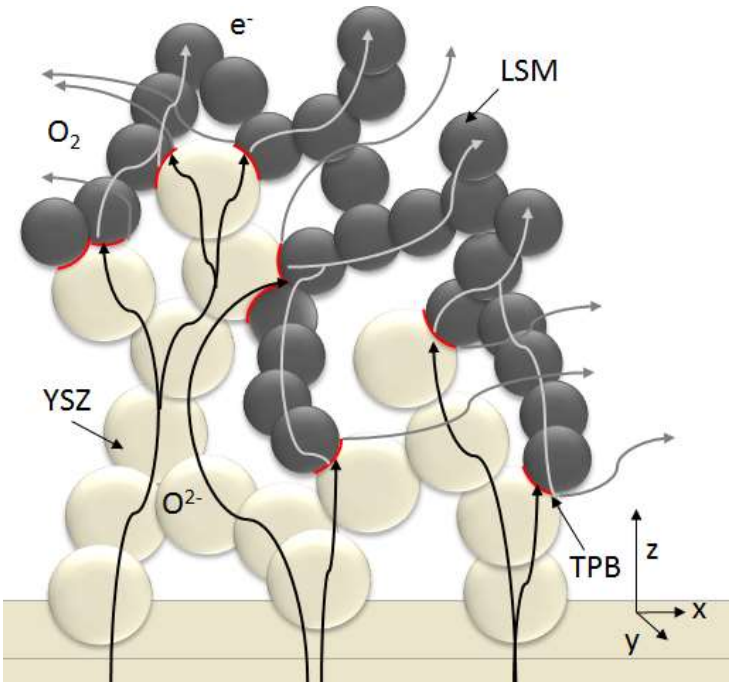

Figure 2.1: Schematic of an oxygen electrode in a SOEC at the electrolyte interface depicting oxygen ion, oxygen gas, and electron transport paths as black, dark grey, and light grey lines respectively; the triple phase boundary is shown as a red line.

In Figure 2.1 oxygen ions (black lines) are being transported through the YSZ structure from the electrolyte layer to the TPB (red lines). Also the evolved oxygen gas (dark grey lines) is being diffused through pores and electrons (light grey lines) are being transported from the TPB through the LSM structure.

The reaction occurring in the anode is widely agreed upon; however, the mechanism by which this oxidation reaction occurs in SOECs has not been confirmed to date. It has been proposed that the mechanism is the opposite of the mechanism for oxygen reduction in a SOFC electrode [21, 22]. This mechanism considers two rate limiting steps: a charge transfer step, and an associative desorption step shown below as equations 2.1 and 2.2 respectively.

$$2O^{2-} + 2S_{ads} \rightleftharpoons 2O_{ads} + 4e^{-} \tag{2.1}$$

$$2O_{ads} \rightleftharpoons O_2 + 2S_{ads} \tag{2.2}$$

The evolution of oxygen gas in the anode is dependent on the current as mentioned previously. The current density in a SOEC can be described using the information from the kinetic and rate constants above and the general Butler-Volmer equation. Adapting the equation for SOECs, Lay-Grindler *et al*. [24] have expressed the relation as,

$$i(z) = nF\left\{k_{ox}e^{\frac{\alpha_{ox}\mathrm{n}FE(z)}{RT}}\Pi_{ox}a_{ox}^{\upsilon_{ox}}(z) - k_{red}e^{\frac{\alpha_{red}\mathrm{n}FE(z)}{RT}}\Pi_{red}a_{red}^{\upsilon_{red}}(z)\right\} \tag{2.3}$$

this expression determines the current at a vertical position, z, under the assumption that the current density is constant in the x-y plane [24]. In equation 2.3, *n* is the moles of electrons transferred; *F* is Faraday's constant; k_{ox} and k_{red} are kinetic constants; α_{ox} and α_{red} are the symmetry factors of the reaction; *E(z)* is the local potential; a_{ox} and a_{red} are the chemical activities of the oxidizing and reducing species; and ν_{ox} and ν_{red} are the stoichiometry factors. As in the case of the Nernst equation the activities here are described in terms of partial pressures or molar fractions of products and reactants, given by equation 2.4 and 2.5 for the anode.

$$a_{ox}(z) = a_{o_2}(z) = \frac{p_{O_2}(z)}{P_0} \tag{2.4}$$

$$a_{red} = a_{O^{2-}} = 1 \tag{2.5}$$

For a more simplified form of the Butler-Volmer equation, an expression for the exchange current density is desired. The exchange current density is the current when the over potential is zero. At open circuit operation the exchange current density (i_0) from the Butler-Volmer equation is dependent on the reaction rates according to,

$$v_{red}^{i=0} = v_{ox}^{i=0} = i_0 = \mathrm{n}Fk_{ox}\, e^{\frac{\alpha_{ox}\mathrm{n}FE_n}{RT}} a_{ox}^{i=0} = \mathrm{n}Fk_{red}\, e^{\frac{\alpha_{ox}\mathrm{n}FE_n}{RT}} a_{red}^{i=0} \tag{2.6}$$

where E_n is the Nernst potential at OCV. By combining equations 2.3 and 2.6 the condensed form of the Butler-Volmer equation for kinetics of the electrochemical reaction in a SOEC oxygen electrode can be obtained [24],

$$i(z) = i_0 \left\{ e^{\frac{\alpha_{ox}\mathrm{n}F\eta(z)}{RT}} \frac{a_{ox}(z)}{a_{ox}^{i=0}} - e^{\frac{-\alpha_{red}\mathrm{n}F\eta(z)}{RT}} \frac{a_{red}(z)}{a_{red}^{i=0}} \right\} \tag{2.7}$$

where η is the activation overpotential, calculated as the difference between the reversible Nernst potential and local potential,

$$\eta_{act}(z) = E(z) - E_n = \left[\varphi_e(z) - \varphi_i(z)\right] - E_n \tag{2.8}$$

The activation overpotenital is the potential lost in order to overcome the activation barrier of the chemical energy [25]. Using this form of the Butler-Volmer equation (2.13) in combination with information on species transport, ionic potential, electronic potential, and oxygen concentration in the anode can be found.

In addition to activation overpotential there are losses in a SOEC related to concentration gradients (Concentration overpotential, η_{conc}) and ohmic losses (ohmic overpotential η_{ohmic}). The concentration overpotential is the result of concentration variation between the reaction site (TPB) and the gas channel. Diffusion of the gas through the pores causes a gradient of concentration from high at the TPB to the low at the gas channel [25]. The losses due to charge transport resistances are referred to as ohmic overpotential. The expression for ohmic potential follows the form of Ohm's Law,

$$\eta_{ohmic} = I\, R_{ohmic} = I\, (R_{ionic} + R_{electronic}) \tag{2.9}$$

2.2.2: Gas Species Transport

The porous transport of oxygen in a SOEC anode must be well understood because it directly affects the total pressure and species concentrations in the anode, which determine the partial pressure of oxygen. Understanding the oxygen partial pressure in the anode is important because of its effect on the cell performance. In the short term a high partial pressure will increase the cell voltage based on the Nernst equation. In the long term, a high oxygen partial pressure has the potential to cause cell degradation, these degradation mechanisms will be examined further in Section 2.4: Cell Degradation.

The oxygen in a porous SOEC anode is evolved in small pores, in the order of micrometers, making diffusion the dominant transport mechanism [23]. Due to the small pore diameter the diffusion in the pores cannot be assumed as simple molecular (Fickian) diffusion [1, 26-28]. In pores of small diameter the collision of gas molecules with the pore wall must be considered in addition to collisions with other gases. To account for the interaction of gas molecules with the solid pore walls the Knudsen number (Kn) is used [1]. A higher frequency of wall collisions (high Knudsen number) results in a lower diffusion rate. The Knudsen number defines this collision frequency as the ratio of a particles mean free path to the pore diameter,

$$Kn = \frac{\bar{\lambda}}{d_{pore}} \tag{2.10}$$

where $\bar{\lambda}$ is the particle's mean free path and d_{pore} is the pore diameter. In the tight pores where diffusion is neither purely Knudsen nor purely Fickian, diffusivity is adjusted with the Knudsen number using the Bosanquet equation,

$$D_{i,j}^{Bos} = \frac{D_{i,j}}{1+Kn} \tag{2.11}$$

where $D_{i,j}^{Bos}$ is the corrected Bosanquet diffusivity and $D_{i,j}$ is the bulk diffusivity. The diffusivity represents the diffusion of species i in a mixture of species i and j. In the anode case this is diffusion of O_2 in an O_2, N_2 mixture. The equation for bulk diffusivity according to Fuller *et al.* [29] is written as,

$$D_{i,j} = \frac{1\times10^{-7}\, T^{1.75}}{\left(v_i+v_j\right)^2 p}\left(\frac{1}{M_i}+\frac{1}{M_j}\right)^{0.5} \quad (2.12)$$

The Bosanquet diffusivity assumes equimolar counter diffusion in the gas mixture. For mixtures of species with similar molecular masses such as O_2 and N_2 this is a reasonable assumption.

To account for the decreased transport pathway of porous media Bruggeman's correction is commonly used,

$$D_{eff} = D\varepsilon^{1.5} \quad (2.13)$$

where, ε is the porosity of the medium. This correction estimates the limitations to transport through a packed bed of spheres of porosity (ε). The modeling of electrodes in SOECs as spherical particles has been shown to match well with experimental results [27], making the Bruggeman correction an appropriate method of finding effective properties.

Although diffusion is the dominant transport mechanism in porous electrodes it is not the only mechanism, convective transport also occurs. To simplify electrode transport models; however, the importance of convective transport in porous electrodes is often assumed to be negligible. This is done by assuming a constant pressure throughout the electrode thickness. This assumption reduces the accuracy of models because of pressures direct effect on Nernst potential. Calculating the pressure gradient across electrodes in SOFC, Resch [28] found that the pressure gradient could be as high as triple the atmospheric pressure. These high gradients were found only for thick electrodes (700 μm). The pressure gradients for electrodes comparable in thickness to SOEC anodes (in the range of 50 μm) were at most only 20% of atmospheric pressure. Although this gradient is small it should not be ignored, in modelling studies or when working to understand the causes of degradation, due to the importance of partial pressure with respect to performance, and possible degradation mechanisms.

2.2.3: Electronic and Ionic Conduction

The transport of ionic and electronic species are defined using their conductivity through a thickness (S cm^{-1}). As seen in Table 2.1 for YSZ and LSM anodes the conductivity of ionic species is considerably lower (four orders of magnitude) than that of electrons.

Zirconia used for ionic transport purposes is generally stabilized with Y^{3+} which replace some Zr^{4+} positions creating oxygen vacancies in the lattice and improving oxygen ion conductivity. The yttria stabilized zirconia in SOECs typically has an yttria content of 8 mol%. This level of substitution gives the highest ionic conductivity and stabilizes the lattice structure at room temperature [19]. The LSM used to transport electrons in the anode is a p-type conductor meaning that electron holes are the main charge carrier. By doping $LaMnO_3$ with Sr^{2+}, replacing La^{3+} positions in the lattice, the number of electron holes is increased and electronic conductivity is improved [30].

The material conductivities presented in Table 2.1 are for fully dense samples. Approximate effective conductivities of an electrode can be found from the solid material conductivity and the Bruggeman equation. For this calculation the porosity is taken as the volume fraction of the material. For a 50:50 volume ratio of LSM:YSZ anode with 30 % porosity that would be 35 % for each phase.

2.3: SOEC Testing

There are numerous techniques available for analyzing both the physical structure and the electrochemical performance of SOECs. The range of techniques currently employed to study the cells morphology will be discussed in Section 2.3.1 and Section 2.3.2 will describe the testing methods for studying the electrochemical performance.

2.3.1: Test Methods (*ex situ*)

The morphological characteristics that are of greatest interest for SOEC electrodes are those that influence the transport of the species participating in the electrolysis reaction (oxygen ions, electrons, and the oxygen gas). Species transport is a major factor responsible for the electrical efficiency and degradation in SOECs [1]. The microstructural characteristics of greatest interest are pore size, pore distribution, particle size distribution, electrolyte-electrode interface connectivity, and functional ceramic distribution. The pore size and pore distribution influence the diffusion of gas species in the electrode. The electrolyte-electrode connectivity affects the ionic transport between these layers. The particle size distribution controls the pathways for electronic and ionic transport in the electrodes.

Scanning Electron Microscopy (SEM)

Microstructural details of the electrode can be obtained using a variety of imaging and analyzing techniques. Scanning electron microscopy (SEM) is one common method for imaging of SOECs. During SEM a focused beam of electrons is used to scan a sample in a controlled chamber that is under vacuum. The electrons' interactions with the sample can be distinguished with a variety of detectors. Differences in interactions with the sample can then be translated into information about its morphology. A common detector for SOEC samples is a back scattering electron detector (BSED), which detects electrons reflected from the sample. Elemental differences in a sample are observed as differences in brightness caused by varying atomic numbers. Elements with higher atomic numbers appear brighter due to stronger reflection than low atomic number elements. The images obtained from SEM can be used to discern between a solid material and pores, since the pores will not reflect electrons. These images give valuable information on interface contact, particle size, pore size, and pore distribution. As mentioned the atomic number of a material will affect the brightness of the image, allowing the ability to discern materials. However, moderate differences in atomic number such as those between Strontium, Yttrium, and Zirconium with atomic numbers 38-40 are not detectable with SEM. These slight differences can be detected using X-ray mapping as discussed below.

2.3.2: Electrochemical Test Methods (*in situ*)

The optimization of SOECs aims to achieve high electrical efficiency and a long lifetime. Developing cells that meet these criteria demands an understanding of the electrochemical mechanisms occurring in the cell, to decrease electrical losses and the risk of degradation. The study of these mechanisms is completed by various methods. Each method applying a disturbance to the cells and measuring the response to that disturbance. This can be done with steady state (constant current) or transient (polarization) conditions. Each testing method provides different information about the cells behaviour.

Constant Current Electrolysis

Studies have operated electrolysis cells at constant currents ranging from -100 to -1500 mA cm^{-2} for times of tens of hours to 9000 hours to study the rates and mechanisms of degradation [31-34]. Long term studies measure the change in voltage over time in mV or percent increase per 1000 hours (mv kh^{-1} or % kh^{-1}). A variety of both in-situ and ex-situ testing before and after constant current electrolysis allow the correlation of cell performance degradation to changes in cell structure and individual process degradation. Further discussion of the correlations which have been made can be found in Section 2.4: Cell Degradation.

Polarization Curves

The standard analysis of a SOEC's performance is a polarization curve, which gives its electrochemical resistance. To obtain these curves a DC current (or voltage) is applied to a cell and the resulting voltage (or current) is measured. When applying a current it is swept from 0 mA cm^{-2} to as much as -1000 mA cm^{-2} (the current values in SOEC are given as negative, because the direction of charge transfer in a SOEC is the opposite of a SOFC). The curve resulting from these measurements provides valuable information on the power required to achieve a certain current density (mA cm^{-2}). The current density is important because it determines the rate of hydrogen production of a cell. The shape and slope of this curve can be affected by, and give important insights into factors such as steam limitations and cell degradation over time. A study by Yang *et al.* [32] made use of polarization curves to study an infiltrated oxygen electrode under different temperatures (800, 850, and 900 °C) and steam delivery rates (30, 50, 70, and

80% absolute humidity (AH)). It was found that under certain conditions after an initial linear period the slope of the curve increased sharply. This was attributed to steam starvation because at a temperature of 800 °C and low AHs (30%), it was seen at lower current densities than it was for higher AHs. At 900 °C the sharp increase in voltage was seen for all AH values due to the increases reaction rate at higher temperature, supporting the hypothesis that the increase in voltage was caused by steam starvation [32]. This increased voltage behaviour due to steam starvation has been reported in other literature as well [35]. The slope of the polarization curves (cell resistance) was found to decrease with increasing temperature. This relationship is expected because of the temperature dependence of the reaction, which follows the form of the Arrhenius equation, and the improved transport at higher temperatures. Cell polarization curves are also very useful tools for comparing cells of different composition including electrode materials, electrolyte materials, or fabrication methods. Studies have compared the performance of LSM and LSCF anodes [33]; LSM, $La_2NiO_{4+\delta.}$ and $Nd_2NiO_{4+\delta}$ anodes [36]; and LSM anodes to LSCF anodes with a GDC inter-diffusion layer [34].

Electrical Impedance Spectroscopy (EIS)

Polarization curves are valuable for gaining information on total cell resistance but they cannot give information about individual process occurring in a SOEC. EIS is commonly used in an attempt to separate the responses of the different process (oxidation reaction, reduction reaction, ion transport, and gas diffusion) within a SOEC. The processes in a SOEC are strongly interconnected however (with overlapping responses) and separating them with certainty is extremely difficult, if not impossible. Therefore, the certainty of any quantitative information gained from EIS cannot be guaranteed. Valuable qualitative information on electrochemical processes can be reliably extracted from EIS, despite the difficulties of quantitative analysis with EIS.

2.4: Cell Degradation

SOEC's higher efficiency and potential to electrolyse molecules other than water, such as CO_2, make them a preferred choice to lower temperature electrolysis systems for stationary applications. However, if the degradation issues currently facing SOECs are not solved their advantages will not be realized. The specific issues facing this technology are electrode contamination from external sources, diffusion of cations from the solid lattice, formation of unwanted species, and anode delamination. In this section these issues will be described in more detail along with potential compositional, microstructural, and design adjustments proposed in literature to mitigate these problems.

2.4.1: Causes of Degradation

The high temperature environment that SOECs operate in, which improve their efficiency, also increase the likelihood of undesired transport and reactions occurring. All components housing the SOECs must be made to withstand this extreme environment to prevent degradation. For example, it has been found that if the interconnecting materials between cells contain Chromium (Cr) it can become mobile and substitute itself into the electrode lattice. To resolve this coating materials have been applied to prevent the Cr from becoming mobile [37]. In a similar issue silica, originating from glass seals, being deposited in the cathode has also been reported [3]. In a review paper on SOECs it was found that the major lifetime issue of anode delamination was not caused by contaminates [38]. The focus for delamination prevention is now centred not on housing materials which can substituted or coated but on reactions within the cells leading to delamination. In the reviewed literature the delamination of SOEC anodes has been attributed mainly to three connected phenomena; high oxygen pressure at the electrolyte-anode interface, diffusion of cations (La^{3+}, Sr^{2+}, and Mn^{2+}), and the formation of unwanted species.

The high oxygen pressure is thought by some to occur in closed pores at the anode-electrolyte interface causing void propagation and eventually anode delamination [3, 37, 39-41]. Rashkeev *et al*. [39]

calculated that a closed void in the zirconia structure of the electrolyte 1 μm in diameter or larger with a pressure of 10^5 atm could lead to void propagation and likely delamination. A pressure of that magnitude was calculated to be possible in a zirconia structure with a lanthanum impurity. This was determined using a relationship for the pressure and temperature dependant Gibbs free energy (equation 2.14) to find the surface oxygen equilibrium pressure for zirconia with La, Sr, and Mn impurities [39].

$$\Delta G(p,T) = E^{surface-2O_2} - E_{mol}^{O_2} - E^{surface} + \mu_{O_2}^{(0)} + kTln\frac{p_{O_2}}{p_{O_2}^{(0)}} \tag{2.14}$$

Where $E^{surface-2O^{2-}}$,$E_{mol}^{O_2}$, and $E^{surface}$ are total energies for a surface with two oxygen vacancies, a single oxygen molecule in a vacuum, and a surface without defects respectively; $\mu_{O_2}^{(0)}$ and $p_{O_2}^{(0)}$ are the oxygen chemical potential and oxygen pressure at standard conditions; and $p_{O_2}$is the partial pressure of oxygen gas in equilibrium with the zirconia surface. The equilibrium pressure of oxygen was highest for a zirconia structure with a lanthanum impurity, roughly 10^5 atm. The critical radius of a closed pore with a pressure of 10^5 atm was estimated as roughly equivalent to the binding energy of the zirconia bonds divided by the pressure multiplied by the distance between breaking bonds and the average length of breaking bonds. The critical radius is the radius above which void propagation would occur [39]. This analysis suggests that the delamination is caused by a closed pore in the electrolyte with an electron conducting impurity.

In a comprehensive study of oxygen electrode delamination Vikar [40] explained that under anodic polarization (electrolysis operation) the chemical potential of oxygen (μ_{O_2}) in the electrolyte at the anode interface is higher than in the anode. The inability of the ionic conducting electrolyte to accept electron holes creates a high resistance to ion transport giving the difference in oxygen chemical potential. The high chemical potential in the electrolyte at the anode interface creates a high equilibrium partial pressure for oxygen. Vikar described this formation of this high oxygen chemical potential created in the electrolyte at the anode surface using an equivalent circuit to model a solid oxide cell [40]. A schematic representation of the electronic potentials (φ) and chemical potentials (μ) is shown as in Figure 2.2.

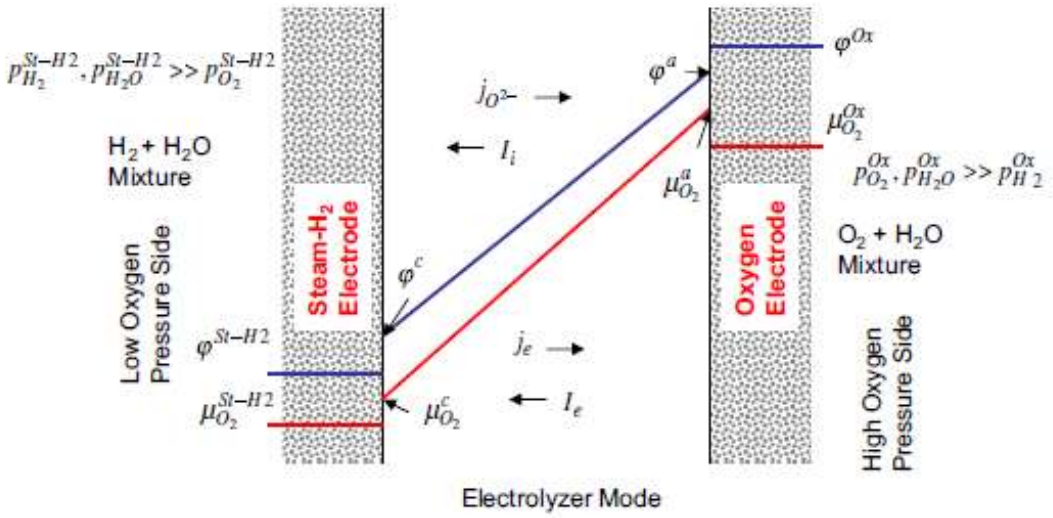

Figure 2.2: Oxygen chemical and electronic potential variations in a SOEC cell [40].

This analysis is in agreement with a study by Knibbe *et al.* that states the high electromotive potential created at the interface allows for the evolution of oxygen in the grain boundaries of the electrolyte, leading to fractures [42]. This study presents the idea that the partial pressure in the electrolyte at the anode interface ($P_{O_2}^a$) is proportional to the partial pressure within the anode at the interface ($P_{O_2}^{Ox}$) according to equation 2.15 [42],

$$P_{O_2}^a = P_{O_2}^{Ox} e^{\frac{4nF}{RT}} \tag{2.15}$$

$$P_{O_2}^a = P_{O_2}^{Ox} e^{\frac{4F}{RT}\left\{(\varphi^{ox}-\varphi^a)-\frac{(E_A-E_N)r_i^a}{R_i}\right\}} \tag{2.16}$$

where n is equal to the oxygen electrode polarization. Virkar reasons that the electrode polarization term should be replaced with one including electrical potentials, ionic resistances (r_i^a is the ionic resistance at the anode electrolyte interface and R_i is the cells total ionic resistance), the applied potential (E_A) and the Nernst potential (E_N) (equation 2.26). Arguing that this term better describes the effect that the voltages, and the ionic and electronic potentials have on the chemical potential of oxygen which, directly affects the oxygen partial pressure.

In agreement with the analysis by Rashkeev *et al.* [39] metals with the ability to conduct electrons have been found in electrolyte grain boundaries. Mn was detected in YSZ electrolyte grain boundaries in one study using energy dispersive X-ray spectroscopy (EDS) after electrolysis operation [42].

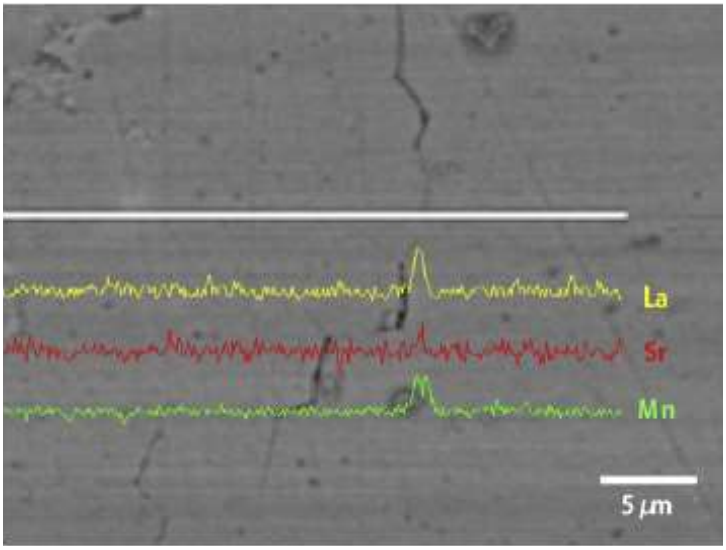

Figure 2.3: SEM and EDS of increased La, Sr, and Mn intensity in electrolyte grain boundary the white line shows the location of the EDS scan[43].

In another study La, Sr, and Mn inclusions were all found in grain boundaries of the YSZ electrolyte using EDS, shown in Figure 2.3 [43]. These cations originating from the anode are believed to be transported towards the electrolyte surface by the ionic flux towards the electrolyte induced by anodic polarization [43, 44].

Cation mobility has also been seen to cause densification in SOEC anodes, potentially increasing any high oxygen partial pressure that exists in the anode [43]. High oxygen pressure LSM has been found to cause cations (La^{3+}, Sr^{2+}, and Mn^{2+}) to separate from the lattice and become mobile [45, 46]. High oxygen partial pressure causes inclusion of nonstoichiometric excess oxygen in the lattice leading to mobility of cations and cation vacancies in the lattice [41, 43, 47, 48]. The equilibrium of excess oxygen is thought to obey the following defect model [45],

$$\frac{3}{2}O_2 \leftrightarrow La_{1-x}Sr_xMnO_{3+\delta} + V_{La}''' + V_{Mn}''' + 6h^{\cdot} \quad (2.17)$$

where V_{La}''' is a vacancy in the A site (La or Sr), V_{Mn}''' is a vacancy in the B site, and $h^{\bullet}$ is an electron hole. The relationship of oxygen partial pressure to cation deficiencies is supported by a study from Mizusaki *et al.* [45]. This study annealed LSM at 1000 °C and p_{O_2} ranging up to 10^5 Pa and found that the A site deficiency increased with increasing oxygen partial pressure to a maximum of 10% deficiency [45].

Cations migrating from the lattice have been found to form unwanted species such as Strontium Zirconate ($SrZrO_3$, SZ) and, more often, Lanthanum Zirconate ($La_2Zr_2O_7$, LZ) at the electrolyte-anode interface [15, 49, 50]. These zirconates are electronically insulating compounds limiting transport in the anode. LZ has a relatively low thermal expansion coefficient, 7.0×10^{-6} K^{-1} [44] compared to 10.5×10^{-6} K^{-1} and 12×10^{-6} K^{-1} for YSZ and LSM respectively [11]. Electrically insulating phases of differing TECs such as SZ and LZ can lead to charge concentrations and mechanical stresses within the anode, leading to a fracture or delamination. A thermodynamic analysis of the La-Mn-Y-Zr-O system found that increasing the yttria content of YSZ or decreasing the lanthanum content of lanthanum manganite could supress the formation of LZ. However, these adjustments would significantly decrease to materials ionic and electronic conductivities [50]. High oxygen partial pressure in the anode has been cited as a cause of degradation [43, 47] and it can help explain the mobilization of cations. However, no basis for partial pressure build up in the anode (except for in closed pores) has been suggested in the reviewed literature.

The degradation mechanisms for SOECs in all of these studies, excluding external contamination, are related to either high oxygen partial pressure or cation diffusion, with evidence that the two are connected. Reduction of oxygen partial pressure in the anode and the electrolyte; reduction of electronic and ionic fluxes in the anode; and prevention of cation diffusion to the electrolyte are all potential methods to mitigate the degradation of SOECs. The currently employed and potential new strategies to mitigate SOEC degradation are outlined below.

2.4.2: Material Development Strategies for Mitigating Degradation

To address the lifetime issues of SOECs (specifically anodes) a variety of adjustments to the standard cell materials and design (YSZ-LSM composite anode with a YSZ electrolyte) have been proposed and tested. To avoid the high oxygen chemical potential in the electrolyte at the anode-electrolyte interface Virkar has suggested a tri-layered electrolyte. Reasoning cells with a dense p-type MIEC on the anode side of the electrolyte and a dense n-type MIEC on the cathode side of the electrolyte will reduce the ionic resistance at these interfaces. The dense MIEC's ability to accept electron charge carriers will lower the ionic resistance at the interface. This reduction in ionic resistance will give a smaller oxygen chemical potential and therefore a smaller oxygen partial pressure in the electrolyte. Potentially preventing the propagation of voids in the electrolyte boundary layers [51].

Other degradation mitigation strategies have focused on preventing cation diffusion into the electrolyte. In an attempt to prevent the diffusion of Mn into the electrolyte layer Li *et al.* [49] applied a Mn-YSZ sol-gel layer between the YSZ electrolyte and LSM anode of a SOEC. Comparing this cell to one having the same electrolyte and anode with no inter-layer. The sol-gel layer was seen to reduce the infiltration of Mn into the electrolyte but not stop it. It also slowed the formation of LZ, but did not prevent it entirely. The layer was able prevent delamination during a 200 hr study at 0.8 V [49].

To entirely prevent LSM and YSZ from interacting with each other and forming LZ or SZ, cells have been prepared with anodes containing a lanthanum based electron conductor and an ion conductor other than YSZ separated from a zirconia electrolyte by an interdiffusion layer. For example, a LSCF-GDC anode with a GDC interdiffusion layer [34]. As mentioned previously GDC is a better ionic conductor than YSZ and therefore it has been used in composite electrodes as the ionic conducting phase in several studies [10, 34, 52]. GDC has also been used as an interdiffusion layer between the anode and electrolyte [31, 44, 53, 54]. Ogier *et al.* [53] tested a variety of cells with interdiffusion layers of GDC, yttria doped ceria (YDC), and those without interdiffusion layers. It was found that all cells with the interdiffusion layer had lower polarization resistances than those without. It was also seen that cells with an interdiffusion layer

showed improved connectivity to the electrolyte surface compared to those without. During the short experiments in this study no LZ or SZ formation was reported [53]. In another study after testing a cell with a LSCF anode, GDC interdiffusion layer, and YSZ electrolyte for 9000 hours, SZ was found at the GDC-YSZ interface. The SZ formation was concentrated at pores and a crack in the GDC layer, suggesting the Sr diffusion occurred on the surface or in the gas phase. Use of a dense GDC layer without cracks should prevent the Sr diffusion and SZ formation [31].

2.5: Summary

This chapter introduced the important physical and chemical properties of materials used in SOECs. Commonly used anode materials and more recently tested materials were presented and compared based on their physical and chemical properties. Current methods for preparing SOEC anodes and their relation to cell microstructure were examined. Emphasizing the requirement for a uniform microstructure to achieve ideal performance. The transport processes occurring in a SOEC and their reliance on the cell microstructure were discussed, along with the dependence of reaction mechanisms on the species transport. The controlled electrode morphology required to systematically study the transport within a SOEC was explained.

A description of the testing methods used to study the relationship of performance to the morphology of a SOEC was given. Both the *in-situ* and *ex-situ* testing methods and the advantages and limitations were explained. The degradation plaguing SOECs and the proposed mechanisms leading to degradation were presented and the evidence to support them was discussed. A variety of attempted and proposed strategies for preventing degradation of SOECs were discussed.

2.6: References

[1] B. Kenney, M. Valdmanis, C. Baker, J. G. Pharoah and K. Karan. Computation of TPB length, surface area and pore size from numerical reconstruction of composite solid oxide fuel cell electrodes. *J. Power Sources 189(2),* pp. 1051-1059. 2009.

[2] A. Hauch, S. D. Ebbesen, S. H. Jensen and M. Mogensen. Solid oxide electrolysis cells: Microstructure and degradation of the Ni/Yttria-stabilized zirconia electrode. *Journal of the Electrochemical Society 155(11),* pp. B1184-B1193. 2008.

[3] A. Hauch, S. H. Jensen, J. B. Bilde-Sørensen and M. Mogensen. Silica segregation in the Ni/YSZ3 electrode. Journal of the Electrochemical Society 154(7), pp. A619-A626. 2007.

[4] Y. Bo, Z. Wenqiang, X. Jingming and C. Jing. Status and research of highly efficient hydrogen production through high temperature steam electrolysis at INET. Int J Hydrogen Energy 35(7), pp. 2829-2835. 2010.

[5] A. Ursua, L. M. Gandia and P. Sanchis. Hydrogen production from water electrolysis: Current status and future trends.

[6] N. J. Maskalick. High temperature electrolysis cell performance characterization. *Int J Hydrogen Energy 11(9),* pp. 563-570. 1986.

[7] M. Ni, M. K. H. Leung and D. Y. C. Leung. Technological development of hydrogen production by solid oxide electrolyzer cell (SOEC). *Int J Hydrogen Energy 33(9),* pp. 2337-2354. 2008.

[8] Wang J, Zhang Y, Liang T, Deng C, Xu J. Effect of oxygen partial pressure on the electrochemical impedance of La0.8Sr0.2MnO3−δ/Zr0.92Y0.08O2 porous composite anodes in solid oxide electrolysis cell. J Power Sources. 2012 6/15;208:415-20.

[9] C. Jin, C. Yang and F. Chen. Characteristics of the hydrogen electrode in high temperature steam electrolysis process. *Journal of the Electrochemical Society 158(10),* pp. B1217-B1223. 2011.

[10] X. Yue and J. T. S. Irvine. (La,sr)(cr,mn)O3/GDC cathode for high temperature steam electrolysis and steam-carbon dioxide co-electrolysis. *Solid State Ionics 225,* pp. 131-135. 2012.

[11] Manoj K. Mahapatra, Singh Prabhakar. Fuel cells: Energy conversion technology. In: Future Energy: Improved, Sustainable and Clean Options for Our Planet. Second ed. Elsevier; 2014. p. 511.

[12] Laguna-Bercero M, Kilner JA, Skinner SJ. Performance and characterization of (la, sr)MnO3/YSZ and La0.6Sr0.4Co0.2Fe0.8O3 electrodes for solid oxide electrolysis cellsâ€ . Chem Mater. 2010 02/09; 2013/10;22(3):1134-41.

[13] Chauveau F, Mougin J, Mauvy F, Bassat J, Grenier J. Development and operation of alternative oxygen electrode materials for hydrogen production by high temperature steam electrolysis. Int J Hydrogen Energy. 2011 201107;36(13):7785-90.

[14] S. Xu, S. Chen, M. Li, K. Xie, Y. Wang and Y. Wu. Composite cathode based on fe-loaded LSCM for steam electrolysis in an oxide-ion-conducting solid oxide electrolyser. *J. Power Sources 239,* pp. 332-340. 2013.

[15] S. Xu, S. Li, W. Yao, D. Dong and K. Xie. Direct electrolysis of CO2 using an oxygen-ion conducting solid oxide electrolyzer based on La0.75Sr0.25Cr0.5Mn0.5O3 − δ electrode. *J. Power Sources 230,* pp. 115-121. 2013.

[16] Tao S, Irvine JTS. A redox-stable efficient anode for solid-oxide fuel cells. Nat Mater. 2003 print;2(5):320-3.

[17] Zhao H, Li Q, Sun L. Ln2MO4 cathode materials for solid oxide fuel cells. Science China Chemistry. 2011 06/01;54(6):898-910.

[18] Kharton VV, Kovalevsky AV, Avdeev M, Tsipis EV, Patrakeev MV, Yaremchenko AA, et al. Chemically induced expansion of La2NiO4+Î´-based materials. Chem Mater. 2007 04/01;19(8):2027-33.

[19] Piao J, Sun K, Zhang N, Xu S. A study of process parameters of LSM and LSM–YSZ composite cathode films prepared by screen-printing. J Power Sources. 2008 1/3;175(1):288-95.

[20] McCoppin J, Young D, Reitz T, Maleszewski A, Mukhopadhyay S. Solid oxide fuel cell with compositionally graded cathode functional layer deposited by pressure assisted dual-suspension spraying. Journal of Power Sources. 2011 20110415;196(8):3761-5.

[21] Liu Q, Yang C, Dong X, Chen F. Perovskite Sr2Fe1.5Mo0.5O6-d as electrode materials for symmetrical solid oxide electrolysis cells. Int J Hydrogen Energy. 2010 201010;35(19):10039-44.

[22] Esquirol A, Kilner J, Brandon N. Oxygen transport in La0.6Sr0.4Co0.2Fe0.8O3−δ/Ce0.8Ge0.2O2−x composite cathode for IT-SOFCs. Solid State Ionics. 2004 11/30;175(1–4):63-7.

[23] Jørgensen MJ, Primdahl S, Bagger C, Mogensen M. Effect of sintering temperature on microstructure and performance of LSM–YSZ composite cathodes. Solid State Ionics. 2001 1/2;139(1–2):1-11.

[24] Lay-Grindler, E, J. Laurencin, G. Delette, J. Aicart, M. Petitjean. L. Dessemond. Micro Modelling of Solid Oxide Electrolysis Cell: From Performance to Durability. International Journal of Hydrogen Energy. 2013. 38(17): 6917–6929.

[25] O'Hayre RP. Fuel cell fundamentals. John Wiley & Sons; 2006. 438 p.

[26] Suwanwarangkul R, Croiset E, Fowler MW, Douglas PL, Entchev E, Douglas MA. Performance comparison of Fick's, dusty-gas and Stefan–Maxwell models to predict the concentration overpotential of a SOFC anode. Journal of Power Sources. 2003 Jul 15;122(1):9–18.

[27] Gaweł DAW. The Development of a Coupled Physics and Kinetics Model to Computationally Predict the Powder to Power Performance of Solid Oxide Fuel Cell Anode Microstructures [Master's]. [Kingston, Canada]: Queen's University; 2013.

[28] Emmanuel Resch. Numerical and Experimental Charaterisation of Convective Transport in Solid Oxide Fuel Cells [Master's]. [Kingston, Canada]: Queen's University; 2008.

[29] Fuller EN, Schettler PD, Giddings JC. New Method for Prediction of Binary Gas-Phase Diffusion Coeffecients. Ind Eng Chem. 1966 May 1;58(5):18–27.

[30] Jiang SP. Development of lanthanum strontium manganite perovskite cathode materials of solid oxide fuel cells: a review. J Mater Sci. 2008 Oct 18;43(21):6799–833.

[31] Tietz F, Sebold D, Brisse A, Schefold J. Degradation phenomena in a solid oxide electrolysis cell after 9000 h of operation. J Power Sources. 2013 2/1;223:129-35.

[32] Yang C, Jin C, Coffin A, Chen F. Characterization of infiltrated (La0.75Sr0.25)0.95MnO3 as oxygen electrode for solid oxide electrolysis cells. Int J Hydrogen Energy. 2010 201006;35(11):5187-93.

[33] Xu C, Wang Y, Jin L, Ding J, Ma X, Wang WG. Degradation of solid oxide electrolyser cells with different anodes. ECS Transactions. 2012 May 04;41(33):97-102.

[34] Hjalmarsson P, Sun X, Liu Y, Chen M. Influence of the oxygen electrode and inter-diffusion barrier on the degradation of solid oxide electrolysis cells. J Power Sources. 2013 2/1;223(0):349-57.

[35] Shin E, Ahn P, Seo H, Jo J, Kim S, Woo S, et al. Polarization mechanism of high temperature electrolysis in a Ni–YSZ/YSZ/LSM solid oxide cell by parametric impedance analysis. Solid State Ionics. 2013 2/7;232(0):80-96.

[36] Chauveau F, Mougin J, Bassat JM, Mauvy F, Grenier JC. A new anode material for solid oxide electrolyser: The neodymium nickelate Nd2NiO4+δ. J Power Sources. 2010 2/1;195(3):744-9.

[37] Mawdsley JR, Carter JD, Kropf AJ, Yildiz B, Maroni VA. Post-test evaluation of oxygen electrodes from solid oxide electrolysis stacks. International Journal of Hydrogen Energy. 2009;34(9):4198–207.

[38] Moçoteguy P, Brisse A. A review and comprehensive analysis of degradation mechanisms of solid oxide electrolysis cells. International Journal of Hydrogen Energy. 2013;38:15887-902.

[39] Rashkeev SN, Glazoff MV. Atomic-scale mechanisms of oxygen electrode delamination in solid oxide electrolyzer cells. International Journal of Hydrogen Energy. 2012; 37(2):1280–91.

[40] Virkar AV. Mechanism of oxygen electrode delamination in solid oxide electrolyzer cells. International Journal of Hydrogen Energy. 201009;35(18):9527–43.

[41] Chen K, Jiang SP. Failure mechanism of (La,Sr)MnO3 oxygen electrodes of solid oxide electrolysis cells. International Journal of Hydrogen Energy. 2011 Aug;36(17):10541–9.

[42] Knibbe R, Traulsen ML, Hauch A, Ebbesen SD, Mogensen M. Solid Oxide Electrolysis Cells: Degradation at High Current Densities. Journal of the Electrochemical Society. 2010 Aug 1;157(8):B1209–17.

[43] Kim J, Ji H-I, Dasari HP, Shin D, Song H, Lee J-H, et al. Degradation mechanism of electrolyte and air electrode in solid oxide electrolysis cells operating at high polarization. International Journal of Hydrogen Energy. 2013 6;38(3):1225–35.

[44] Martin M. Materials in thermodynamic potential gradients. The Journal of Chemical Thermodynamics. 2003 Aug;35(8):1291–308.

[45] Mizusaki J, Mori N, Takai H, Yonemura Y, Minamiue H, Tagawa H, et al. Oxygen nonstoichiometry and defect equilibrium in the perovskite-type oxides La1−xSrxMnO3+d. Solid State Ionics. 2000;129(1–4):163–77.

[46] Mitchell JF, Argyriou DN, Potter CD, Hinks DG, Jorgensen JD, Bader SD. Structural phase diagram of (La)(1-x)(Sr)(x)(Mn)(O)(3+delta): Relationship to magnetic and transport properties. Phys Rev B. 1996 Sep 1;54(9):6172–83.

[47] Keane M, Mahapatra MK, Verma A, Singh P. LSM–YSZ interactions and anode delamination in solid oxide electrolysis cells. International Journal of Hydrogen Energy. 2012 Nov;37(22):16776–85.

[48] Mitterdorfer A, Gauckler LJ. La2Zr2O7 formation and oxygen reduction kinetics of the La0.85Sr0.15MnyO3, O2(g)|YSZ system. Solid State Ionics. 1998 Spring;111(3–4):185–218.

[49] Li N, Keane M, Mahapatra MK, Singh P. Mitigation of the delamination of LSM anode in solid oxide electrolysis cells using manganese-modified YSZ. International Journal of Hydrogen Energy. 2013 20;38(15):6298–303.

[50] Chen M, Nicholas Grundy A, Hallstedt B, Gauckler LJ. Thermodynamic modeling of the La–Mn–Y–Zr–O system. Calphad. 2006 Dec;30(4):489–500.

[51] Virkar AV. Reversible Fuel Cells with Tri-Layer Electrolytes. ECS Trans. 2015 Jun 2;68(1):3253–60.

[52] Kim-Lohsoontorn P, Kim Y-M, Laosiripojana N, Bae J. Gadolinium doped ceria-impregnated nickel–yttria stabilised zirconia cathode for solid oxide electrolysis cell. International Journal of Hydrogen Energy. 2011 Aug;36(16):9420–7.

[53] Ogier T, Bassat JM, Mauvy F, Fourcade S, Grenier JC, Couturier K, et al. Enhanced Performances of Structured Oxygen Electrodes for High Temperature Steam Electrolysis. Fuel Cells. 2013 Aug 1;13(4):536–41.

[54] Kim SJ, Choi GM. Stability of LSCF electrode with GDC interlayer in YSZ-based solid oxide electrolysis cell. Solid State Ionics. 2014 Spring;262:303–6.

Chapter 3: Variation of SOEC Anode Microstructure

The transport of products and reactants of the oxygen evolution reaction in a SOEC anode is a strong determinant of the cell's performance. Increasing the transport rate of all reaction participants would significantly improve cell performance, although increasing all transport rates is a difficult task. The three distinct species in the reaction (O^{2-}, e^-, and O_2) each travel through a different pathway. An increased transport pathway for one species is likely to limit the transport pathway of the other two species, requiring a careful balance of all three pathways. In the porous LSM-YSZ composite electrodes considered in this work the ions are transported through the YSZ solid network, the electrons are transported through the LSM solid network, and the oxygen is transported through the pore network. Limitations in transport (especially high resistances near the anode-electrolyte interface) are thought to cause degradation in the anode as discussed in Section 2.4 [1-3]. The morphology of the anode dictates the transport pathways. The ability to control morphology is therefore desirable, because it allows for the tailoring of transport pathways. With this control the changes in transport and performance caused by varying the microstructure can be systematically studied. This chapter will discuss the methods developed for producing uniformly structured electrodes of varied morphology.

3.1: Controlling Anode Porosity and Microstructure

Systematic study of the effect of prepared electrode parameters (porosity, particle agglomerate size, and interface morphology) on cell performance, is made possible by the ability to control the porosity and morphology of a SOEC anode. It is expected that an increase in cell porosity will increase the rate of oxygen transport; however, a higher porosity is also expected to reduce the transport of electrons and ions in the electrode. Preparing electrodes with small particle agglomerates is expected to increase the TPB length and

lower polarization resistance relative to an electrode with large agglomerates, due to a lower reaction overpotential. Anodes prepared with a varied porosities and particle sizes can be used to test these hypotheses. An ideal electrode morphology can be selected by studying the effects of microstructure on the transport of each species and cell performance.

3.2: Experimental

To achieve control of anode morphology a detailed anode preparation method is required. This section will discuss the ink formulations chosen, and ink processing completed for anode preparation using spray deposition. A detailed explanation of the spray deposition apparatus and its various parameters will be then be given. Followed by a description of the sintering procedure for the cells. Finally the characterization techniques used to examine prepared anodes will be described.

3.2.1: Ink Formulation

The ink formulations that were prepared for this work are based on the ink used by Kenney [4]. In that study electrodes with uniform, controllable, and repeatable microstructures were prepared with a pressure assisted ink deposition method in a study of oxygen transport in solid oxide fuel cell cathodes [4]. The inks in the current work were composed of Lanthanum Strontium Manganite $(La_{0.8}Sr_{0.2})_{0.95}MnO_3$ (LSM) from Praxair Surface Technologies, as the electron conductor; Yttria Stabilized Zirconia $(Y_2O_3)_{0.08}(ZrO_2)_{0.92}$ (YSZ) from Tosho Ceramics, as the ion conductor; Poly-Vinyl Pyrrolidone (PVP) from Praxair Surface Technologies, working as a binder; and Iso-Propyl Alcohol (IPA), as the dispersion medium. The inks were mixed on a weight percent (wt %) basis. The first ink prepared, referred to as baseline (BL) ink, contained: 0.55 wt % LSM, 0.55 wt % YSZ, and 0.03 wt % PVP the balance (98.87 wt %) was IPA. The BL ink was varied in order to produce less porous electrodes. The variation (Dilute Ink, DI) was prepared using a 25% increase in solvent volume, the ceramic and binder masses were unchanged.

It is expected that the increase in solvent concentration will increase the probability of ceramic particles sinking and agglomerating in the film deposited during spraying, leading to a less porous structure.

3.2.2: Ink Processing and Systematic Control of Deposition

After the ink materials were initially mixed they were ball milled for 20 hours using 6 mm zirconia milling media to ensure complete mixing and improve particle size uniformity. After ball milling the inks were sonicated for 10 min at 42 kHz in a Branson 3510 sonicator. The time between sonication and spraying was limited to a maximum of 5 minutes. Particle diameters of sonicated and unsonicated BL inks were measured with a Zetasizer Nano ZS (Malvern Instruments) and compared to verify that the sonication was able to disrupt particle agglomerates. Particle size distribution estimates for each ink are based on ten samples. The ink that was sonicated prior to particle size measurement had a lower polydispersity index (PdI) than that of the unsonicated ink. The PdI is measure of particle size distribution width, or variation in particle sizes measured. The PdI of the sonicated ink was 0.135 ± 0.080 (mean ± standard deviation). The ink that was not sonicated before the particle size measurement had a PdI of 0.296 ± 0.267. The particle diameter of the sonicated ink was also much lower and showed less deviation than the unsonicated ink. The sonicated ink had a particle diameter of 207 ± 18.3 nm compared to 1163 ± 355 nm for the unsonicated ink. These distributions show that the particles in the inks have a tendency to agglomerate and require sonication to achieve small and uniform particle size.

Ink spraying was started after the pre-spraying treatment (ball milling for 20 hours and sonicating for 10 min at 42 kHz) was completed. The inks were deposited onto 20 mm diameter electrolyte disks. The two electrolytes used were 0.25-0.30 mm thick YSZ disks and 0.13-0.17 mm thick proprietary Hionic™ disks (half cells purchased with cathodes), both supplied by Fuel Cell Materials. The samples sprayed on YSZ disks were used to determine ideal spraying parameters for a uniform anode morphology. The samples sprayed on the half cells were used for electrochemical testing, which will be discussed in Chapter 4. An air brush (AB724 Unico-Air) was used to spray the anode ink. A schematic and an image of the of the air

brush setup can be seen in Figure 3.1. Ink loaded into the airbrush filled the ink cup and the volume between nozzle opening and the cup, a spring loaded valve prevented ink from flowing into the air supply tubing. A bubbler was placed in the spray cup to ensure mixing of the ink and prevent particle settling. When the airbrush pin was lifted (controlled automatically with a solenoid, connected to a timer providing spray pulses with a pause in between) the spring loaded valve (blocking the air supply) was opened and the ink in the volume between the nozzle and the cup was sprayed. The hydrostatic pressure of the ink in the cup forced more ink into the volume between cup and the nozzle opening, if the pin is lifted the pressurized air sprays this ink. To ensure a constant volume of ink in the spray cup a pump was used to add ink at the same rate that ink was sprayed. The ink was deposited onto a restricted circle to give anodes of repeatable area. The circle had a diameter of 13 mm, restricted using a stainless steel guide and a rubber seal placed between the electrolyte and the guide. The seal prevented the ink from spreading outside the desired electrode area. The electrolyte being sprayed was mounted on a rotating platform to prevent non-uniform deposition.

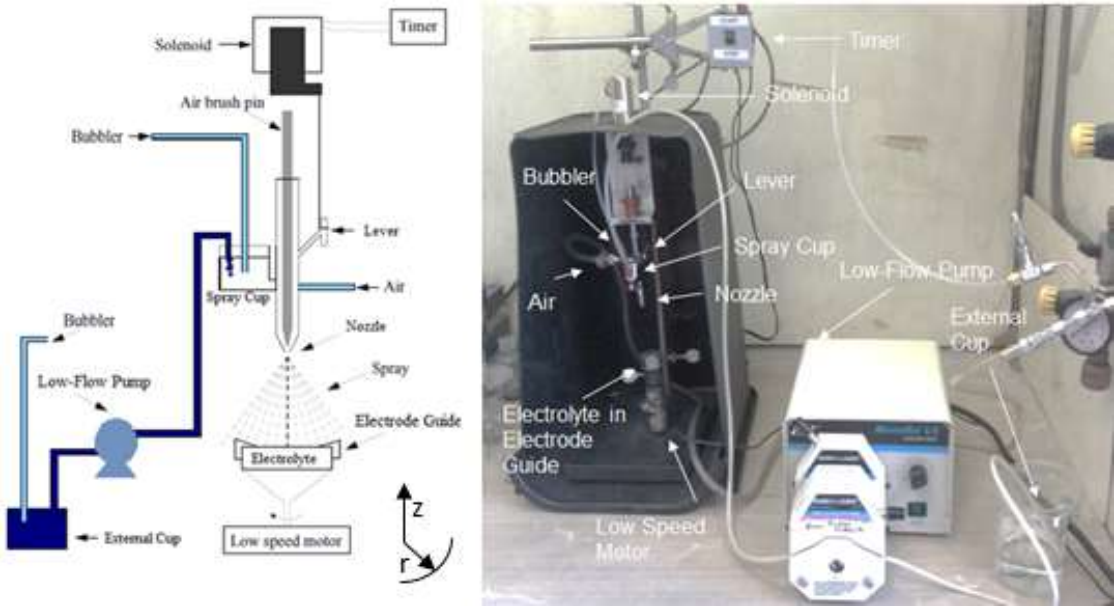

Figure 3.1: Air brush spraying setup for used for electrode deposition, schematic (adapted from [1])

The spray deposition of the ink was controlled by adjusting the air flow rate, the area of the air brush opening for ink spraying (varied by changing the height the air brush pin was lifted), the height of the nozzle above the electrolyte, and the spray pulse time. The pressure of the air was held constant at 10 psi. The experimental method for developing the spraying protocol for anode deposition is outlined in Table 3.1. Starting from initial spraying conditions one parameter at a time was changed, to address any issues seen, until the ideal parameters for ink deposition were selected. The air flow rate was measured using a rotameter.

Table 3.1: Development of experimental spraying method for porous anodes

Parameters changed and experimental observations	Spray pulse duration [s] (pause=1.0 s)	Height of nozzle above electrolyte [mm]	Air flow rate [LPM]	Pin height [mm]
Initial spraying parameters, liquid pooling seen ↓	1.0	55	8.5	0.4
Height increased to prevent liquid pooling, non-uniform anode thicknesses seen ↓	1.0	120	8.5	0.4
Pin height adjusted, effect on interface connectivity seen, large ink droplets seen ↓	1.0	120	8.5	0.2-0.45
Air flow rate adjusted, effect on ink droplet size and morphology observed ↓	1.0	120	4-9.5	0.4
Spray pulse rate lowered to prevent liquid pooling ↓	0.2	120	9.5	0.4
Height lowered to prevent ink being sprayed outside of electrode area (wasted) ↓	0.2	70	9.5	0.4
Pin height adjusted to improve anode thickness uniformity ↓	0.2	70	9.5	0.3-0.4
Optimal parameters selected and repeated to produce anodes for physical and electochemical analysis	0.2	70	9.5	0.35

The height the air brush pin was lifted in the z direction (pin height) was varied between 0.2 and 0.45 mm. The higher the pin was lifted the greater the difference between the fixed radius of the nozzle opening (r_2) and the radius of the pin at the height of nozzle opening (r_1), as shown in Figure 3.2.

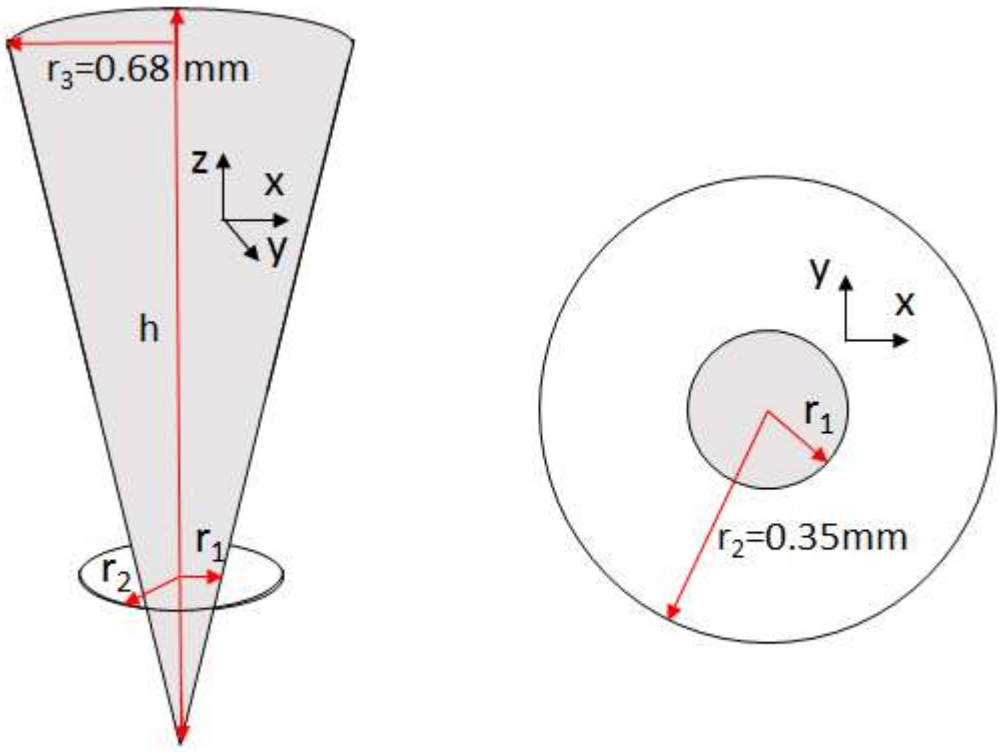

Figure 3.2: Schematic showing the effect of pin height on area for ink flow(pin shown in grey), r2 represents the radius of the nozzle opening and r1 represents the radius of the pin at the same height as nozzle opening, h (height of the tapered point of pin) = 14.64, r2(radius of nozzle opening) = 0.345 mm

At a height of 0 mm the two radii are equal (0.345 mm) and no area is open for ink flow. As the pin height is increased so is the area open for spraying of ink (white area in right hand side of Figure 3.2). A relationship of change in height to open area was found based on measurement of the height of the tapered section of the pin (14.64 mm), the diameter at top (1.35 mm), the height where r_1 is equal to r_2 (7.48 mm

from the tip), and the knowledge that diameter at the tip is 0 mm. The area open for spraying (A_{flow}) can be calculated based on the difference in radii according to equation 3.1, where r_1 (in mm) can be found as a function of pin height (h_p) according to equation 3.2.

$$A_{flow} = \pi (r_2^2 - r_1^2) \tag{3.1}$$

$$r_1 = 0.345 - \left(\frac{0.675}{14.64} \cdot \Delta z\right) \tag{3.2}$$

During spraying an increase in this area led to a higher flow rate of ink and larger ink droplets, this is discussed further in the results section. The height the pin would be lifted was set before spraying each anode. The height was varied by adjusting the length of the connection from the solenoid to the lever. A greater pin height was achieved by decreasing the length of the connection.

The height of the nozzle above the electrolyte was tested at 120 and 70 mm. The duration of the spray pulse and pause times were controlled by the timer connected to the solenoid. Spray pulse times of 0.2 and 1.0 s were tested both with a pause of 1.0 s. The pause between spray pulses allowed the IPA to evaporate leaving only the ceramic particles and binder.

3.2.3: Cell Sintering

After electrodes were deposited onto the electrolyte they were sintered at high temperature before electrochemical testing or imaging. Sintering improves inter-granular contact and electrode-electrolyte interface contact, while removing any remaining IPA and PVP. Cells were heated at a rate of 3 °C min^{-1} to 100 °C and held at 100 °C for one hour to evaporate any remaining IPA. Followed by heating at 3 °C min^{-1} to 1100 °C, holding the temperature at 1100 °C for 3 hours, and cooling the cells at a rate of 3 °C min^{-1} to room temperature. The heating and cooling rates were chosen to avoid damage to the cells that could be caused by the different thermal expansion coefficients of the components. The temperature of 1100 °C was based on published results for YSZ/LSM composite electrodes showing that the lowest polarization resistances were seen for cells sintered between 950 and 1200 °C [5, 6].

3.2.4: Characterization Techniques

The ability to see the differences in microstructure caused by variation of the cell fabrication method is extremely useful for determining ideal fabrication parameters. An effective method for observing morphology on a micrometer scale is scanning electron microscopy (SEM). In this work anode cross sections were examined with a MLA Quanta 650 FEG-ESEM (FEI). SEM imaging was completed with a back scattering electron detector (BSED) at low vacuum (0.75 torr). The voltage for the SEM was varied between 5 kV and 15 kV in order to give clear images. Cells were scored with a carbide tip and split along the centre of the electrode in preparation for SEM imaging. The spilt cells were then mounted in epoxy. After the epoxy was set the samples were polished using sandpaper of increasing grit: 200, 400, and 600 followed by six micron and one micron diamond polishing to provide a smooth surface for imaging.

An approximation of electrode porosity was required to study the effect of ink formulation and spraying parameters on porosity. The porosity (ε) of the anodes were estimated as one minus the solid electrode volume divided by the total electrode volume as shown in equation 3.3. The total electrode volume was determined based on the electrode thickness (the arithmetic mean of nine SEM measurements) and the electrode area according to equation 3.4. The diameter of the electrode was found using a digital micrometer (Vertex Tools). The solid volume of the electrode was found by dividing the electrode mass by the density (from supplier specifications) of the solid LSM-YSZ composite according to equation 3.5. The electrode mass was found by subtracting the mass of the electrolyte prior to deposition from the mass of the electrolyte and electrode after sintering.

$$\varepsilon = 1 - \frac{V_{solid}}{V_{total}} \tag{3.3}$$

$$V_{total} = th_{electrode} * \pi * r^2 \tag{3.4}$$

$$V_{solid} = \frac{W_{electrode}}{\rho_{electrode}} \tag{3.5}$$

Particle diameter analysis was completed using ImageJ software to study the anodes morphological characteristics. SEM images of anode cross sections were imported into ImageJ to determine particle diameters. The threshold values (adjustment from grey scale to black and white) of the images were adjusted to match the porosity to the value calculated with the method described above, the result can be seen in Figure 3.3 b.

The black and white image was then processed with adjustable watershed segmentation (AWS). Watershed segmentation splits particles using a largest inscribed circle method, based on a Euclidean distance map (EDM). Starting from local maxima in the EDM a circle's radius is increased until it touches the edge of a particle or another increasing circle. If multiple largest circles are inscribed in a single particle it is segmented at a neck between the largest circles (if the size of the neck is small enough relative to the smallest inscribed circle).

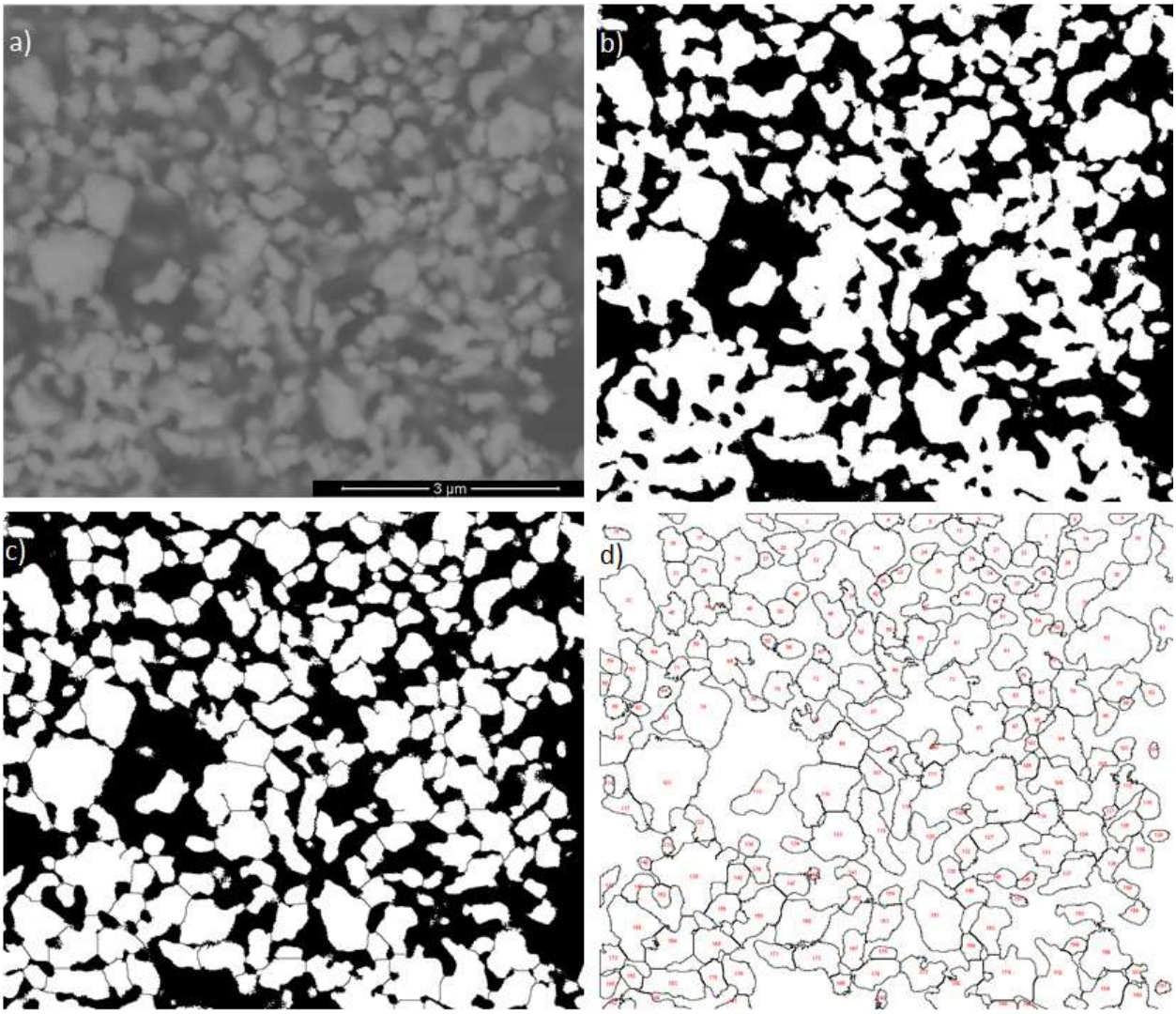

Figure 3.3: Processing of an SEM image for particle size analysis, a) shows the unchanged image, b) shows the image after tolerance adjustment, c) is the binary image after watershed segmentation, and d) gives the contours of particles analysed.

For AWS the ratio of the smallest inscribed circle's radius to the radius of a circle inscribed in the neck can be controlled. The higher this ratio the fewer the number of segmentations. The ratio of the radii was set to 3 for this work because this was found to consistently produce structures that best matched the morphology (Figure 3.3 c).

AWS is a useful tool for separating particles; however, it does have limitations. The global porosity (a 3-D property) may not be the same as the local porosity of the area being sampled (a 2-D property). The

watershed tolerance is similarly limited as it may not correctly segregate all particles to match exactly the raw SEM image. To address these limitations after threshold adjustment and AWS images were compared to raw images, if they did not closely resemble the unaltered image (porosity and segmentation) they were not used. Two SEM images were analysed for each anode to prevent the use of anomalous particle size data.

The ImageJ "Analyze Particles" function was used, after segregation and screening of the images to determine the Feret's diameter of the pores and particles. Only particles with an area greater than 0.020 μm^2 were counted (the upper 90% of particles assuming a spherical particle using particle diameter analysis of inks discussed above). Any particle size below this was attributed to pixilation of the image. Total areas sampled for all anodes were greater than 400 μm^2, giving a total sample size greater than 700. Figure 3.3 a, c) show how well the particles of unaltered and segregated images match, on a relatively small sample area. The small scale of Figure 3.3 (roughly 6 μm by 6 μm) was chosen to display the ability of AWS to segregate particles. This same technique was also used for image analysis of larger areas (up to 10 times larger).

3.3: Results

The spraying parameters of SOEC anodes prepared by pressure assisted spray deposition were studied to produce anodes with small particle sizes and uniform anode thicknesses. This section will discuss the spraying parameters found to be most important for preparing uniform anodes. Anodes prepared with two ink formulations of different dilutions will be compared. Followed by analysis of the effect deposition rate had on the porosity and particle size of the prepared anodes.

3.3.1: Anode Morphology

Oxygen gas, produced at TPB locations in the porous anode structure, escapes the anode by diffusion and limited convection. Cell performance is dependent on the efficient transport of O_2 gas through

the anode into the flow channel. The diffusion of gas is reliant on the porosity of the electrode, which provides the network for gas transport. Control of the electrode porosity is needed to systematically study the effects of porosity on the cell performance and lifetime.

Similarly transport of ionic and electronic species is dependent on the solid matrix in the anode, which is determined by the volume fraction of the solid lattice and the size of particles. The control of particle sizes will allow study of its effect on the performance (specifically polarization resistance) of the anodes.

As mentioned above the height the spray brush pin was lifted was found to be an important parameter for anode preparation because it controlled the open area for ink flow of the air brush. At greater heights a larger area was open for ink flow (Figure 3.2), allowing for a greater flowrate of ink and larger ink droplets. Poor anode-electrolyte interface contact was seen in anodes prepared with larger pin heights (greater than 0.35 mm). The larger ink droplets sprayed with a greater pin height were seen to cause significant amounts ink to pool on the electrolyte surface. Ink pooling caused incomplete contact at the interface as can be seen in Figures 3.4 c, d). It is though that this poor contact is the result of ceramic particles agglomerating, leaving areas where no ceramic particles are in contact with the electrolyte. During the deposition of the anode in Figure 3.4 b-d) the spray pin height was decreased after five minutes when ink was seen to be pooling. This change in pin height restricted the area open for ink to flow, resulting in: smaller ink droplets, a lower ink flow rate, and a more uniform microstructure.

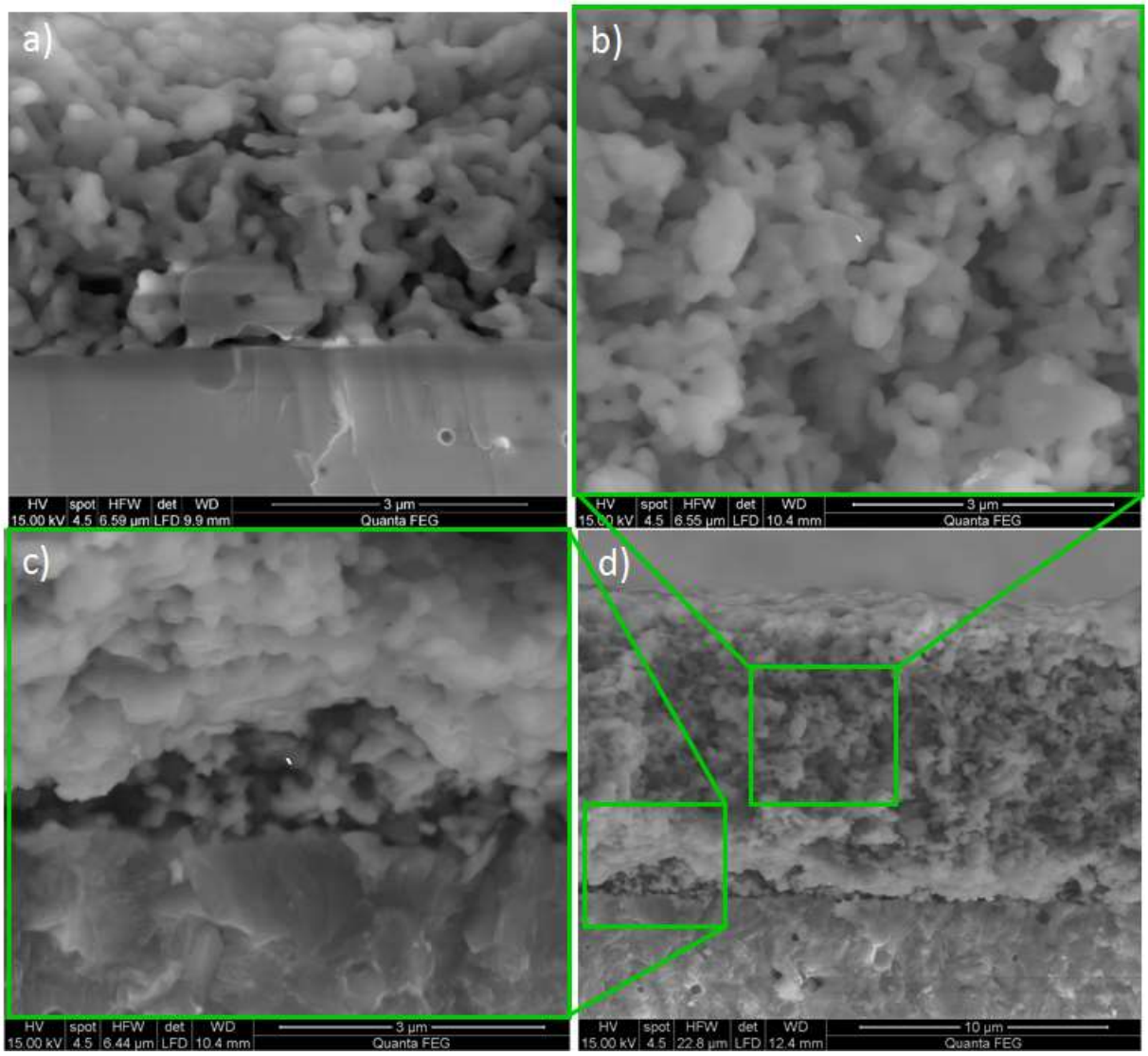

Figure 3.4: The effect of pin height on microstructure uniformity and interface contact the anode in a) was sprayed with a pin height of 0.4 mm the anode in b-d) was sprayed with a pin height of 0.45 mm for the first 5 min, and 0.35 mm for the remainder both cells were sprayed with a nozzle height of 120 mm, an air flow rate of 8.5 LPM, and a spray pulse duration of 1.0 s. c-d) show the poor interface contact resulting from a greater pin height.

The flow rate of the air in the spray deposition setup was also seen to have a significant effect on anode morphology. A lower flow rate of air was seen to produce larger ink droplets in comparison to a high flow rate. Figure 3.5 shows an anode produced with a lower air flowrate than those show in Figure 3.4. The relatively large particle agglomerate sizes (Figure 3.5 a) and non-uniform thickness (Figure 3.5 b, bottom anode) are evident from these SEM images. The larger ink droplets produced with a lower flow rate are

thought to have allowed ceramic particles to move around more freely than in a single small droplet. The particle movement made it possible for ceramic particles to agglomerate creating a non-uniform electrode with larger solid agglomerates.

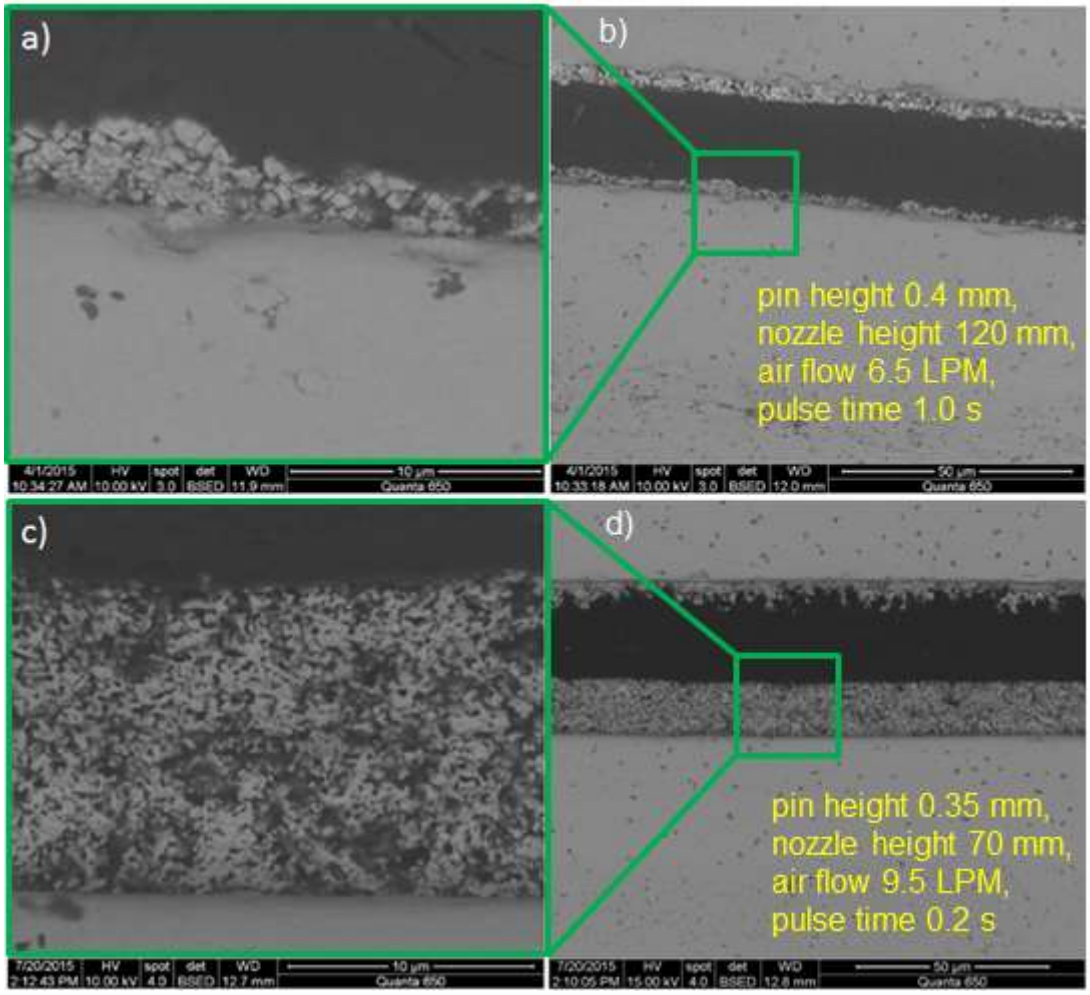

Figure 3.5: The effect of spraying parameters on anode morphology, a-b) anode produced with a pin height of 0.4 mm, nozzle height of 120 mm, an air flowrate of 6.5 LPM, and a spray pulse duration of 1.0 s; c-d) anode of the preferred structure (uniform thickness) produced with a pin height of 0.35 mm, nozzle height of 70 mm, an air flowrate of 9.5 LPM, and a spray pulse duration of 0.2 s.

At a nozzle height of 120 mm above the electrolyte a large amount of ink was being sprayed outside of the 13 mm diameter electrode area. To prevent ink wastage the nozzle height was reduced to 70 mm. At this reduced distance the spray pulse duration was lowered to 0.2 s to ensure no liquid pooling was caused.

Spraying with a greater air flowrate (9.5 LPM) and a reduced nozzle height, pin height, and spray pulse duration (70 mm, 0.35 mm, and 0.2 s respectively) was seen to consistently give uniform anodes, similar to that seen in Figure 3.5 c-d.

Comparing the porosities of the two ink formulation (baseline, BL and dilute ink, DI), the porosities were not seen to be significantly different. The mean porosity of six BL anodes was 0.54 ± 0.11. For four DI anodes the mean porosity was 0.55± 0.10. These porosities overlap significantly, suggesting that varying the solvent concentration of inks is not an effective way of controlling porosity. The deposition rate of ceramic particles (μg cm^{-2} min^{-1}) was; however, seen to effect the porosity of the anode.

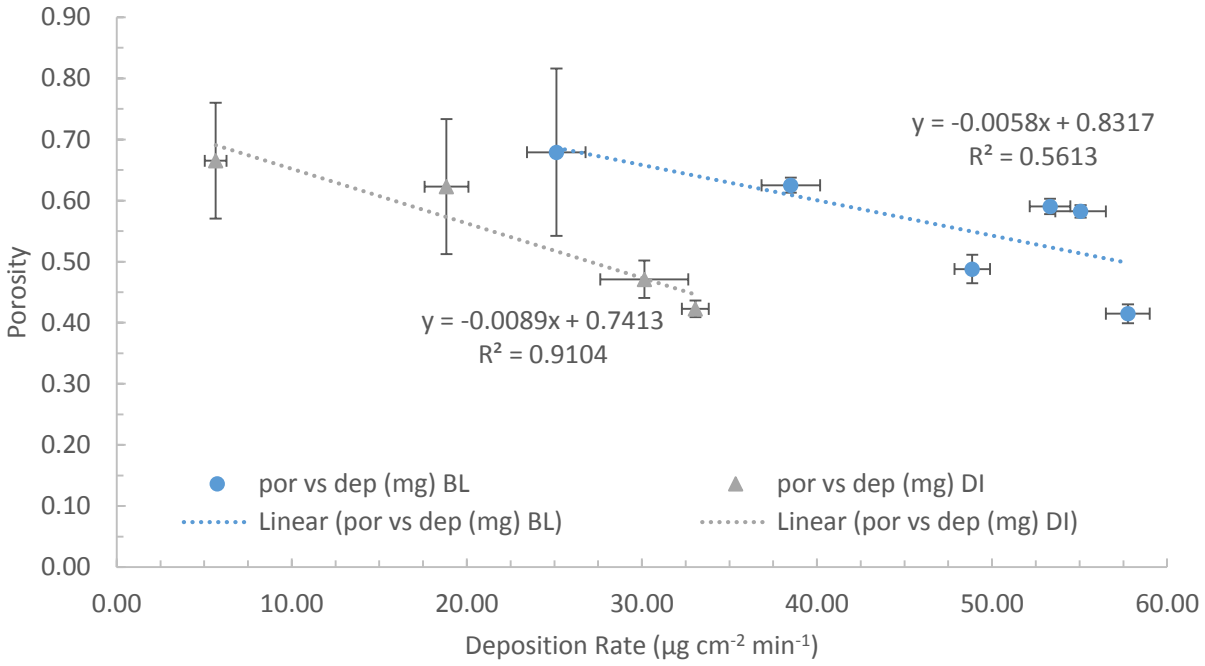

Figure 3.6: Relation of ink deposition rate (μg cm^{-2} min^{-1}) to anode porosity for the Baseline (BL) and Dilute ink (DI) formulations, the error bars presented for the porosity were found using a thickness one standard deviation from the mean thickness, the error bars for the deposition rate are the values for electrode masses one standard deviation from the measured mass (based on 3 measurements).

It can be seen in Figure 3.6 that a decrease in deposition rate is correlated to an increase in anode porosity for both the BL and DI anodes. The variability in deposition rate between anodes was caused by

varying the volume of ink in the spray cup. A larger volume of ink created a greater pressure (hydraulic head) giving a higher flow rate.

The varying degree of particle rearrangement seen to cause particle agglomerates and non-uniform electrodes in Figure 3.5 is also thought to have caused the variation in porosity seen in Figure 3.6. It is hypothesised that an increased deposition rate lead to a liquid film on the substrate surface that was thicker than that of a low deposition rate. With specific gravities of 4.4 (LSM) and 5.9 (YSZ) the dense ceramic particles were able to sink to the bottom of the film and agglomerate (as was shown to happen during the sonication tests in Section 3.2.2) in a thicker liquid film, giving less porous structures. In the case of a thinner film there was less room for particle movement and agglomeration creating a more porous anode. All the BL anodes were produced with the same pin height (0.35 mm), nozzle height (70 mm), air flowrate (9.5 LPM), and pulse duration (0.2 s). During the preparation of the DI anodes the nozzle height was 120 mm, the pulse duration was 1.0 s, the air flow rate was adjusted between 4 LPM and 8.5 LPM, and the spray pin height was adjusted between 0.35 and 0.45 mm.

If the longer spray pulse times are taken into consideration and the deposition rate is given as rate in terms of number of pulses each of which has a pause time of 1.0 s ($\mu g\ cm^{-2}\ pulse^{-1}$) the deposition rates of the two inks are much more similar. This is a better comparison than deposition on a per unit time basis because the drying times between pulses is the same for both cases (1.0 s). In Figure 3.7, where deposition rates were adjusted for number of pulses, the correlation between deposition rate and porosity (slope of the line of best fit) is similar for both anode inks. However, due to the varied thickness of the DI anodes prepared with low deposition rates there is large error associated with the porosities reducing the significance of the similarities. The BL anodes produced at a spray pulse of 1.0 s were very thin and uneven giving errors too large to be statistically significant (porosity ± 0.17 at a minimum). A direct comparison of the two inks with the same spraying parameters cannot be made because of non-uniformity of the BL anodes prepared with a spray pulse of 1.0 s.

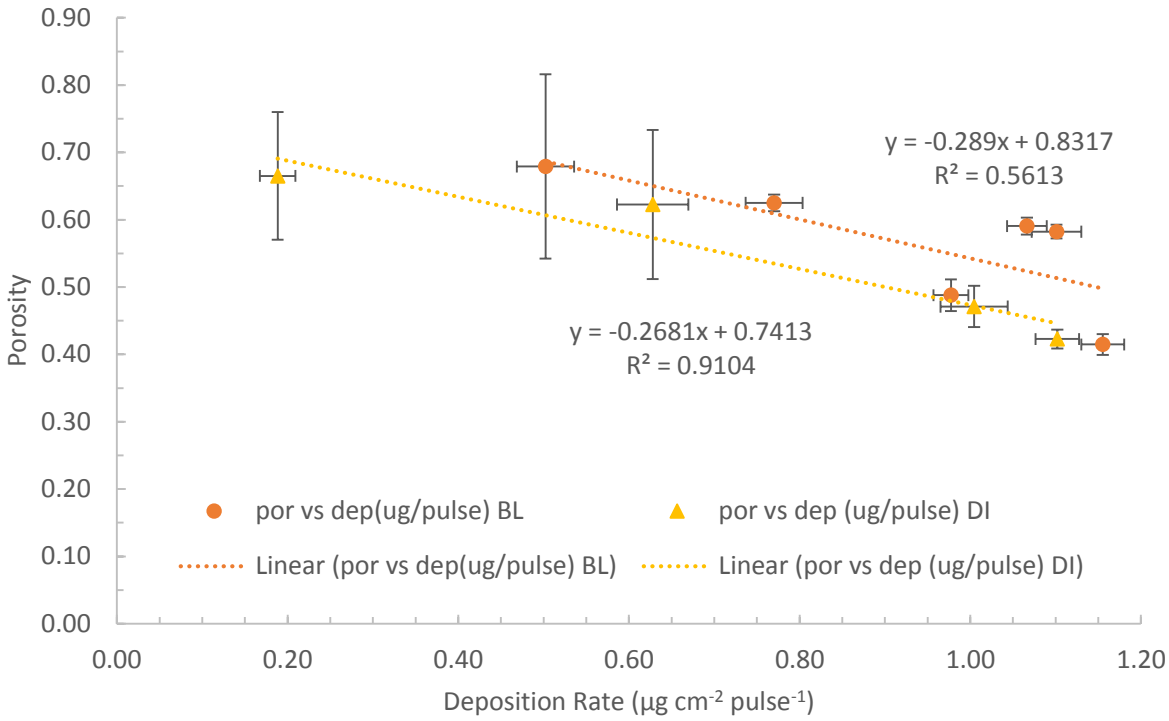

Figure 3.7: Relation of ink deposition rate (µg cm^{-2} $pulse^{-1}$) to anode porosity for the Baseline (BL) and Dilute (DI) ink formulations, each pulse has a drying time of 1.0 s for all spray pulse times therefore this is a better comparison than Figure 3.6.

Particle diameter analysis was completed using ImageJ software to study the effects of deposition rate on particle agglomeration. SEM images of anode cross sections were imported into ImageJ and analysed using the method discussed in Section 3.2.4 to calculate the Feret's diameters of the particles. It was noted that for the BL anodes produced with the same spraying parameters the deposition rate affected the particle size distribution of the sintered anodes.

The particle size distribution of anodes produced with a lower deposition rate were skewed toward smaller values than those produced with a higher deposition rate. A histogram comparing the anodes with the lowest and highest deposition rates (cells BL-31-03#3 and BL-24-03#2, deposition rates of 0.502 and 1.155 µg cm^{-2} $pulse^{-1}$ respectively) is shown in Figure 3.8.

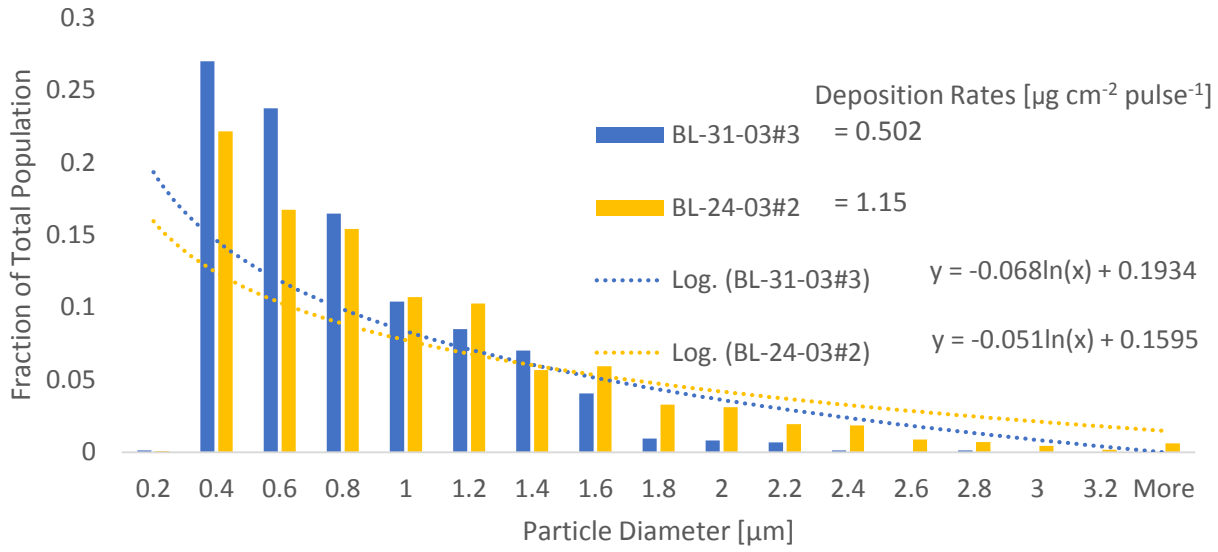

Figure 3.8: Particle size distributions of anodes produced with the same ink formulation and spraying parameters, with deposition rates 0.502 and 1.155 µg cm^{-2} $pulse^{-1}$ for cells B-31-03#3 and B-24-03#2 respectively.

The greater fraction of particles with large diameter particles seen for anodes deposited at a higher deposition rate, supports the hypothesis of particle agglomeration in the ink film discussed above. The greater deposition rate (thicker liquid film) allows for more particle rearrangement (sinking) and agglomeration, leading to more large particles. The lower fraction of small particle diameters (for anodes with a high deposition rate), gives a fitted curve with a smaller negative coefficient than the anode prepared with a low deposition rate, which is skewed towards small particle sizes.

Table 3.2: Relationship of Particle Distribution to Deposition Rate

Cell	BL-31-03#3	BL-24-03#1	BL-31-03#4	BL-30-04#2	BL-24-03#2
Deposition Rate	0.502	0.770	1.10	1.07	1.15
Log coefficient	-0.068	-0.073	-0.058	-0.056	-0.051
Particle Diameter (Mean)	0.702	0.713	0.822	0.858	0.908

The correlation of increasing deposition rate to increasing particle size can be observed as the lower negative coefficient of the fitted natural logarithm curves seen for higher deposition rates, as shown in Table 3.1. Additionally the mean particle diameter was seen to increase when the deposition rate was increased.

3.4: Conclusions

A highly controlled spray deposition method for preparing porous oxygen electrodes for solid oxide electrolysis cells composed of lanthanum strontium manganite and yttria stabilized zirconia has been developed. The importance of the various spraying parameters have been defined. The parameters seen to give the preferred microstructure were: a pin height of 0.35 mm, a nozzle height of 70 mm above the substrate, and an air flowrate of 9.5 LPM. A characterization technique was developed to quantify particle size distributions in produced anodes. An increase in deposition rate was shown to produce anodes with lower porosity and larger particle agglomerates.

3.5: References

[1] Virkar AV. Mechanism of oxygen electrode delamination in solid oxide electrolyzer cells. International Journal of Hydrogen Energy. 201009;35(18):9527–43.

[2] Kim J, Ji H-I, Dasari HP, Shin D, Song H, Lee J-H, et al. Degradation mechanism of electrolyte and air electrode in solid oxide electrolysis cells operating at high polarization. International Journal of Hydrogen Energy. 2013 6;38(3):1225–35.

[3] Martin M. Materials in thermodynamic potential gradients. The Journal of Chemical Thermodynamics. 2003 Aug;35(8):1291–308.

[4] B. Kenney, "An Experimental and Modelling Study of Oxygen Reduction in Porous LSM/YSZ Solid Oxide Fuel Cell Cathodes" (2009)

[5] Piao J, Sun K, Zhang N, Xu S. A study of process parameters of LSM and LSM–YSZ composite cathode films prepared by screen-printing. J Power Sources. 2008 1/3;175(1):288-95.

[6] Jørgensen MJ, Primdahl S, Bagger C, Mogensen M. Effect of sintering temperature on microstructure and performance of LSM–YSZ composite cathodes. Solid State Ionics. 2001 1/2;139(1–2):1-11.

Chapter 4: Electrochemical Behaviour of Solid Oxide Electrolysis Anodes with a Controlled Structure

A standard SOFC button cell testing apparatus (ProboStat™ from NorECs) has been modified for SOEC testing. The operating conditions have been controlled to allow stable testing. Commercially available cells as well as cells with the same electrolyte and cathode as the commercial cells, but anodes prepared for this work have been tested. Polarization, short term electrolysis, and electrical impedance spectroscopy (EIS) measurements have been made. This chapter will discuss the adjustments to the experimental apparatus, and the selection of experimental parameters for SOEC testing. The results observed for various anode morphologies will be compared and the effect of anode morphology on performance will be discussed.

4.1: Solid Oxide Electrolysis Test Station

Numerous parameters must be carefully monitored and controlled to collect usable data on the operation of the SOECs, necessitating the need for a specialized testing system. To obtain quality data during testing it is important to maintain a steady supply of steam to the cathode, air to the anode, and current across a SOEC. The cell and the electrical connections in the testing apparatus must be immobilized to ensure constant electrical contact, for reliable data collection. The anode chamber must be sealed from the cathode chamber and the external atmosphere to ensure a controlled environment. Temperatures, currents, voltages, and flowrates must be measured continuously during testing to ensure their stability. Apparatus materials must be stable at high temperatures because temperatures will be in the range of 800 °C throughout testing.

Methods for electrochemically testing a SOEC measure the cell's response to a change in current, or voltage. The measurements can be completed under different operating conditions (temperature,

pressure, gas concentrations) and compared to understand reaction and transport mechanisms in the cell. A response occurs quickly (ms) and can be small in magnitude (mV) making the precision of measurements important. This section will discuss the setup of the test station used to meet all of these requirements.

4.1.1: Feed Subsystem and Humidifier

The supply of sweep gases and reactants was strictly controlled to ensure minimal variation of constant parameters. The air supplied to the anode was controlled using a mass flow controller (Aalborg GFC17A-BAL6) to maintain a constant flow rate. In order to deliver steam to the cathode water was added to a carrier gas (5% H_2 in N_2). Initially to humidify the carrier gas liquid water was added. The water was vaporized as it traveled toward the cathode through the section of the ProboStat™ encased in the furnace. However, this flash vaporization of the water produced large disturbances in the voltage results. The water supplied formed droplets producing a slug flow condition in the supply tube. The vaporization of these slugs of water with pockets of carrier gas between caused inconsistent steam supply, giving the disturbances in voltage.

A humidifier was developed for these experiments to address the inconsistent steam supply. The carrier gas was passed through a Nafion® tube (Perma Pure) in a bath of heated water. Nafion® was selected as a membrane because of its ability to selectively transport water. The water in the humidifier was heated by circulating water through a temperature controlled external water bath (Grant Instruments). Water vapour permeated through the Nafion® humidifying the carrier gas. The water vapor was driven across the membrane by the gradient in steam partial pressure between the carrier gas and the heated water. Over the length of the tubing the water vapor partial pressures were equilibrated. The manufacturer of the Nafion® tubing states that humidities will equilibrate in 100 to 200 ms; since, the residence time of the gas in the Nafion® tube for these experiments was greater than 10 seconds equilibration of water partial pressure can

be assumed.[1] The partial pressure of water vapour in the humidifier was controlled by adjusting the temperature of the water bath according to the Antoine equation,

$$\log_{10} P^{sat} = A - \frac{B}{T+C} \quad (4.1)$$

where A, B, and C are constants specific for water in the temperature range of 1-100 °C. The temperature of the humidifier was set between 70 and 81 °C.

To verify the assumption that the steam flow rate could be estimated using the Antoine equation, humidified gas was passed through a packed bed of dehydrated Dririte™ to absorb the steam. The packed bed was weighed before and after the humidified gas was passed through it for 40 to 60 minutes.

Table 4.1: Humidification System Testing

Water Temperature (°C)	Carrier Gas Flowrate [SCCM]	H_2O partial pressure [atm]	Time [min]	H_2O Expected [g]	Uncertainty	H_2O Experimental [g]	Absolute Difference	Percent Difference
80.6	10.0	0.478	60.0	0.442	0.012	0.4469	0.005	1.13
80.9	10.0	0.485	60.0	0.454	0.013	0.4814	0.027	6.02
80.3	8.0	0.473	45.0	0.260	0.008	0.2761	0.016	6.16
80.2	15.0	0.471	45.0	0.484	0.010	0.4504	-0.034	-6.93
79.3	18.0	0.454	40.0	0.482	0.009	0.4968	0.014	3.00
							S.D	4.79

In the five tests run the mass of water absorbed by the Dririte™ matched closely (within 7%) to the theoretical mass expected based on the Antoine equation. The uncertainty of the expected masses (based on the error in the thermocouple and MFC measurements) amounts to as much as half of the difference seen between experimental and expected masses. Considering the small difference in masses, relative to the uncertainty, the expected steam delivery was considered a reasonable assumption of the amount of

[1] $\tau = \frac{V}{\dot{V}} = \frac{\frac{A}{L}*L}{\dot{V}} = \frac{1.7145\frac{cm^3}{ft}*1.5\ ft}{10\frac{cm^3}{60\ s}} = 20.29\ s$

steam supplied to the cathode. All steam flow rates provided in this thesis were found using this method. The data for this testing can be seen in Table 4.1.

The voltages obtained at a constant current density for experiments where steam was supplied as humidified gas were significantly more stable than experiments with liquid water vaporized as it traveled through the testing apparatus. The reduced voltage fluctuation (40 mV) of humidified gas supply can be clearly seen in comparison to the large (100 mV) fluctuation in the liquid water supply experiment in Figure 4.1.

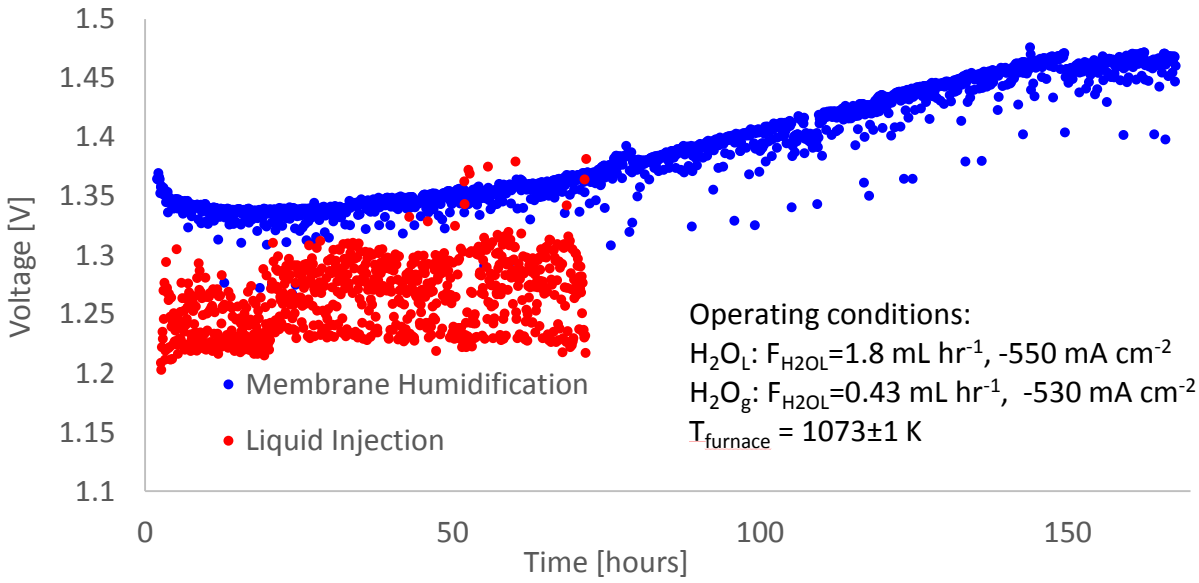

Figure 4.1: Voltage at constant current for gas humidified by flash vaporization and membrane humidification, flow rates are given as (liquid water equivalent in mL $hour^{-1}$).

The voltage in the humidified case was seen to be fluctuating at a regular interval of close to an hour. This fluctuation was found to be caused by a change in flow rate of the air supplied to the anode. The flow of air increased periodically, due to the pumping systems in the building, causing a lower voltage.

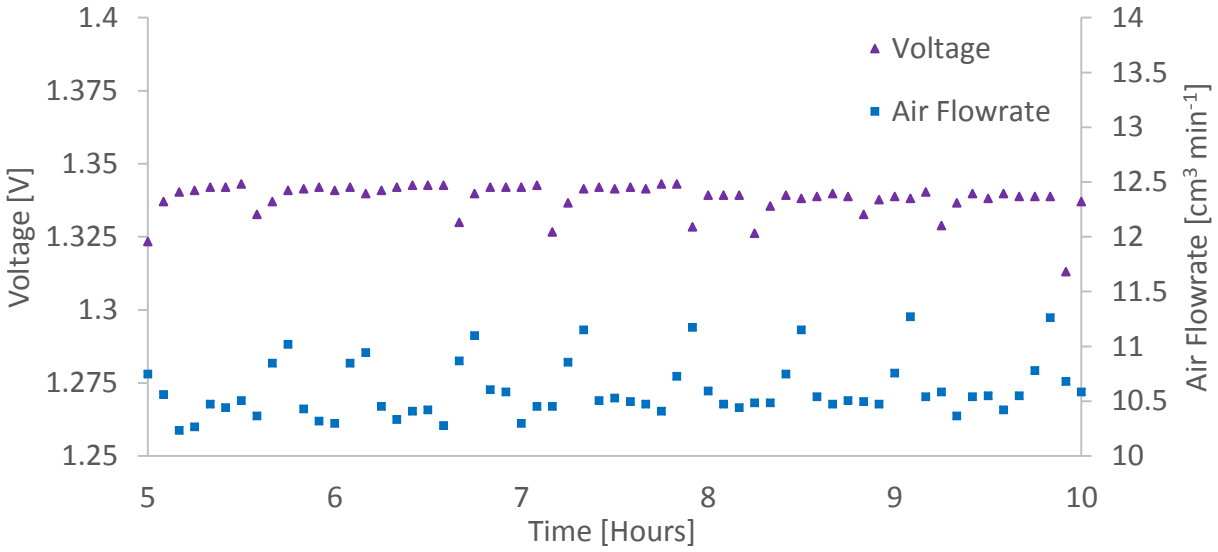

Figure 4.2: Voltage fluctuation during electrolysis with large air flow fluctuation, the apparatus conditions were as follows; i = -530 mA cm^{-2}, $T_{furnace}$ = 800 °C, F_{H2O} = 0.43 mL hr^{-1}

At the time of the test showing periodic air flow increases, a pressure regulator and mass flow meter not a mass flow controller (MFC) were being used to control the supply of air. The air flowrate was seen to fluctuate by 1 SCCM (10% of the total flow) leading to the 40 mV fluctuation.

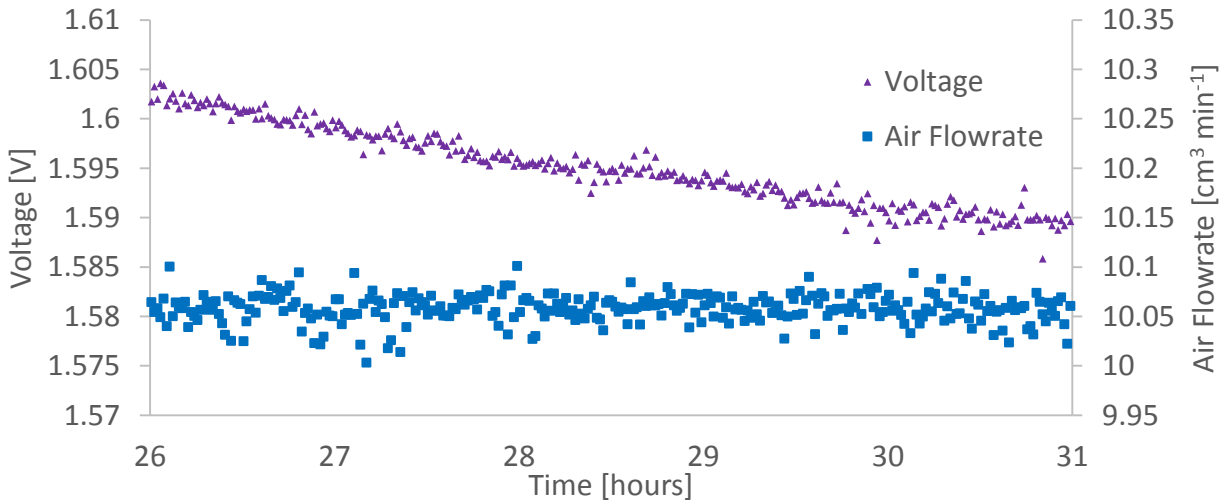

Figure 4.3: Voltage fluctuation during electrolysis with decreased air flowrate fluctuation using a MFC, the apparatus conditions were as follows; i = -0.464 mA cm^{-2}, $T_{furnace}$ = 800 °C, F_{H2O} = 0.43 mL hr^{-1}.

When a MFC was added the fluctuation in air flowrate was reduced to 0.1 SCCM (1% of the total flow) and the voltage fluctuations were seen to decrease to less than 10 mV. This is the first use of a Nafion® membrane humidifier in a ProboStat™ testing system for SOEC studies. Experiments in the literature using a ProboStat™ for steam electrolysis testing have used commercially available humidifiers, which were shown to give stable results [1]; as well bubbled nitrogen carrier gas through a heated bath, however this was shown to be unstable at high steam concentrations and therefore only used for steam concentrations below 15 mol% [2].

4.1.2: Electrochemical Reactor (ProboStat™) Setup

The apparatus used to complete experiments was the ProboStat™ button cell test station (NorECs). This system uses a spring loaded mechanism to keep the cell being tested under compression and create a seal between anode (external) and cathode (internal) chambers. A schematic of the setup can be seen in Figure 4.4. The top of ProboStat™ apparatus was encased in an electrical furnace (Pottery Supply House) to heat it to operating temperature.

In this setup the current is supplied to the cell by passing through the base of the Probostat™ and then through electrical leads travelling the height of the reactor to the cell. In the cathode chamber the electrons reach the cathode through a nickel mesh (current distributor) attached to a mushroom cap on top of the copper tube that travels the height of the reactor. The humidified gas was supplied to the cathode through a stainless steel tube with a 1/16 inch inner diameter that was inside the copper tube carrying the current. A hole in the centre of the mushroom cap and flow channels on its surface in contact with the mesh distribute the humidified gas across the cathode. The copper tube was loaded on a spring to ensure the nickel mesh made good contact with the cathode. In the anode chamber two separated platinum (Pt) electrical leads from the base connected to a Pt electrode mesh were used, one to transport current (working lead) and one to measure the voltage (sensing lead).

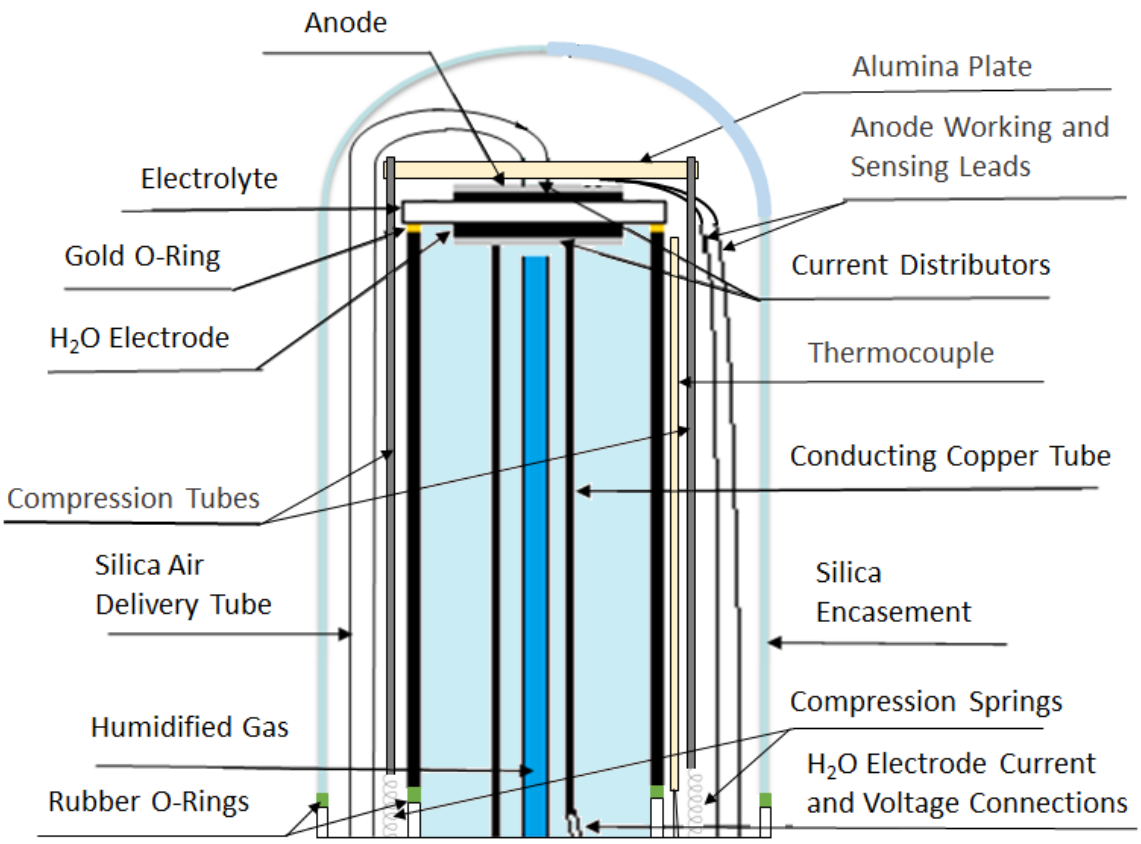

Figure 4.4: Schematic of Cell in ProboStat™ with supply and electrical connections.

The anode mesh was held in place by an alumina plate, which was compressed by the spring loaded assembly. The air was supplied to the anode through a bent silica tube outside of the alumina tube. To distribute sweep gas the alumina plate had flow channels on its surface in contact with the electrode mesh. The lead wires were connected to the Pt mesh and both were compressed in a hydraulic press to ensure a uniform thickness.

The compression force on the alumina plate was also needed to create a seal between the anode and cathode chambers. A seal was placed at the top of the alumina tube between the tube and the electrolyte, separating the anode chamber and cathode chamber (light blue area in Figure 4.4). A gold O-ring (Fuel Cell Materials) was found to be the best seal. As the apparatus was heated the gold softened while under

compression adhering to the alumina tube and the electrolyte creating a seal. Sealing using silver O-rings was also tested and although they initially appeared to create a good seal, micro-cracks formed in the silver. These cracks were not visible at first but evidence of oxidation (green sections, NiO) on the cathode could be seen such as in Figure 4.5. After numerous heating and cooling cycles with the silver seals the cracks grew and could be clearly seen.

At the base of the alumina tube a Viton® rubber O-ring (green O-ring in Figure 4.4) separated the anode and cathode chambers. A silica tube closed at one end was placed around the setup encasing the active components. At the base of the silica tube a Viton® rubber O-ring was used to seal the anode chamber from the external environment.

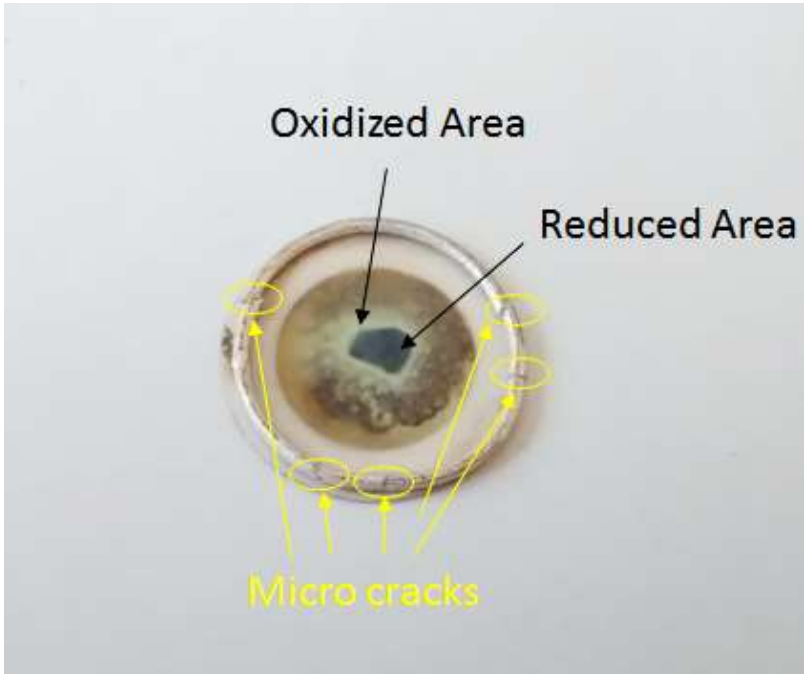

Figure 4.5: SOEC cathode showing micro cracks in seen in the silver O-ring and oxidation (green section, NiO).

The water electrolysis reaction and humidification of the cathode gas stream are both strongly dependent on temperature. Control and monitoring of temperatures to ensure stability throughout the experiment is very important. The temperature in the humidifier was controlled by setting the temperature

of the circulating water bath. A thermocouple connected to the data acquisition unit (DAQ) was used to measure the temperature of the water in the humidifier. To prevent condensation of water in the gas feed line (which could cause unstable voltages as in the case of the liquid water injection) the temperature at all points between humidifier and the cell were maintained above 100 °C. To sustain these temperatures the ProboStat™ setup was modified. The gas feed line in the base was wrapped with a resistance heater connected to an adjustable power supply.

Above the base extending into the furnace to distribute heat to the section above the base that was outside of the furnace (maintaining its temperature above 100 °C) a copper tube was placed around the silica tube encasing the anode chamber.

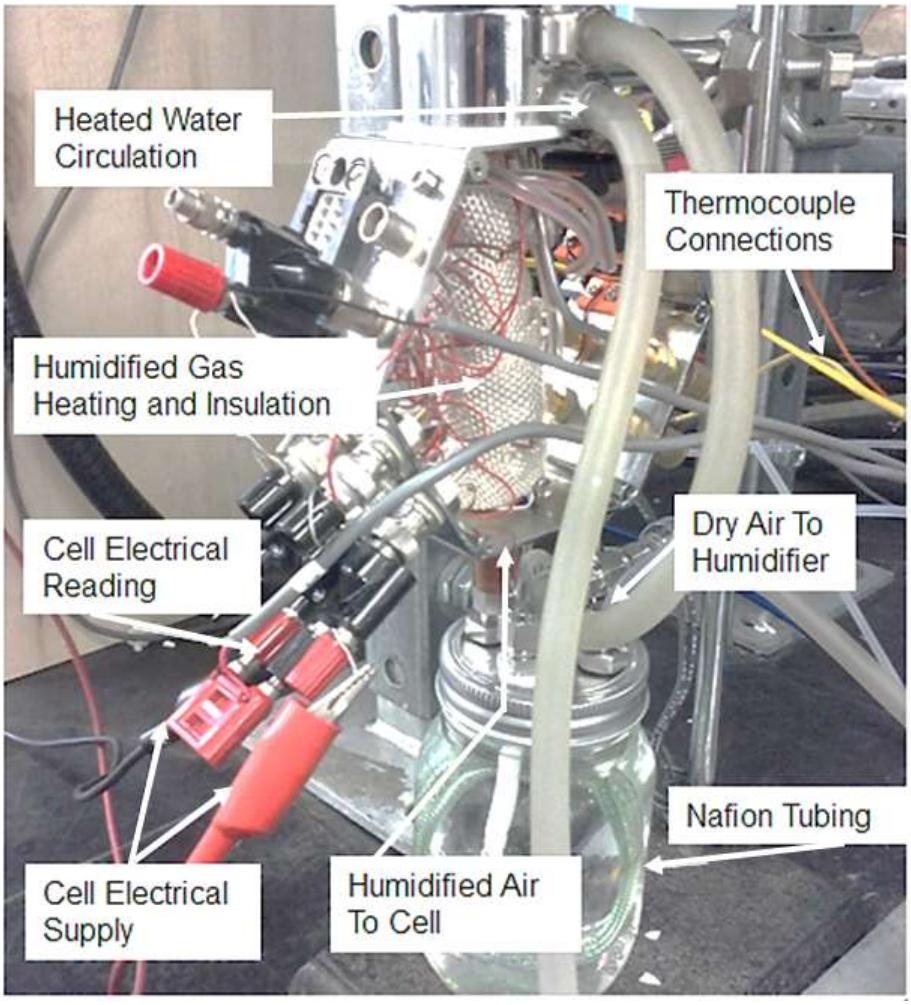

Figure 4.6: ProboStat™ base with humidifier, thermocouples, and electrical connections

This copper tube was initially also wrapped with resistance heaters and insulation; however, this was found to create too high of a temperature (over 140 °C) for some heat sensitive components in the ProboStat™ base. The temperatures in the base, between the base and the furnace, and in the anode chamber near the cell were also monitored with thermocouples connected to the DAQ. The temperature in the anode chamber was controlled by adjusting the temperature of the furnace. Temperature, flow and polarization data was collected with the combination of the DAQ (34970A Data Acquisition/Switch) and BenchLink software, both from Agilent Technologies. Signals from the MFCs, thermocouples, and power supply (galvanostat) were received by the DAQ unit, sent to the BenchLink software, amplified as needed, and recorded.

4.1.3: Polarization and EIS Measurements

The application of potential or current across the SOEC in the ProboStat™ was completed using a potentiostat/galvanostat 273A (pstat/gstat, Princeton Applied Research). For polarization measurements the potentiostat applied a voltage and the DAQ was used measure the current. For EIS measurements the galvanostat was used to supply a current and a gain-phase analyzer (1260-A Solartron Analytical) was used to record the impedance response.

The wiring setup for inducing and measuring current and voltage can be seen in Figure 4.7. The current supplied by the galvanostat or potentiostat was calculated by measuring the voltage across a 50 mΩ shunt resistor with the DAQ and multiplying by 20, based on Ohm's law ($I = V/R = V/0.05 = 20 \cdot V$). The voltage across the cell was measured between the anode sensing lead and the cathode lead connection. Measuring with a sensing lead on the anode side reduces the voltage added by the apparatus because the majority of the current is passed through the working lead wire. The very small current in the sensing wire produces a very small additional voltage in the wire according to Ohm's law.

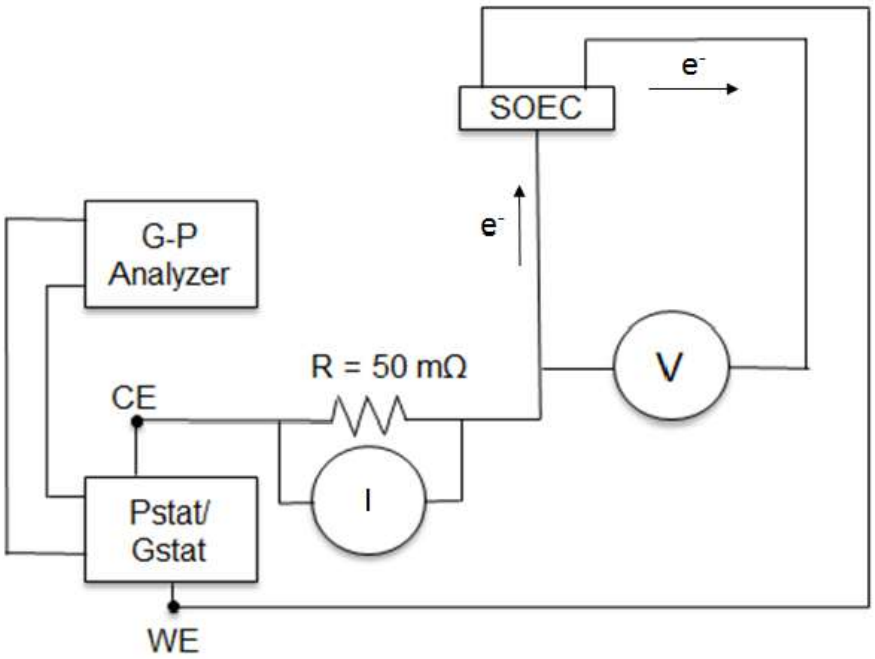

Figure 4.7: Wiring scheme for electrochemical measurements, where CE and WE are the counter and working electrodes respectively.

4.2: Experimental Design

To determine the experimental procedure for testing of SOECs different testing methods were compared on commercially available NextCell (NC) solid oxide cells (Fuel Cell Materials). The quantity of steam supplied during polarization measurements were compared. As well as methods of adjusting the power supplied to the cell. The commercially available cells were tested under various conditions for a comparison to cells with anodes prepared for this work.

4.2.1: Data Collection Parameters

Polarization and constant current measurements were completed on purchased NCs to develop the experimental method for testing SOECs. The first factor in the experimental method studied was the rate

of steam delivery relative to the rate of hydrogen production. The rate of steam electrolysed is dependent on the current supplied to a cell according to Faraday's law of electrolysis,

$$\frac{dN}{dt} = \frac{I}{nF} \tag{4.2}$$

where dN/dt is the rate of steam electrolysis, I is the current, n is the number of electrons participating in the reaction (2 in the cathode reaction), and F is Faraday's constant. As the current increases so does the steam reduction rate (electrolysis). Supplying steam at a constant stoichiometric ratio to the rate of steam reduction will maintain a steady-state gas composition in the cathode chamber of a SOEC. However, for simplicity, SOEC studies supply steam to cells at a constant rate during polarization. To understand what effect the steam supply rate had on voltage during polarization, a comparison study was completed. Steam was supplied at a constant rate, a stoichiometric ratio to conversion, the results can be seen in Figure 4.8. The polarization with the stoichiometric ratio of steam supplied was completed first.

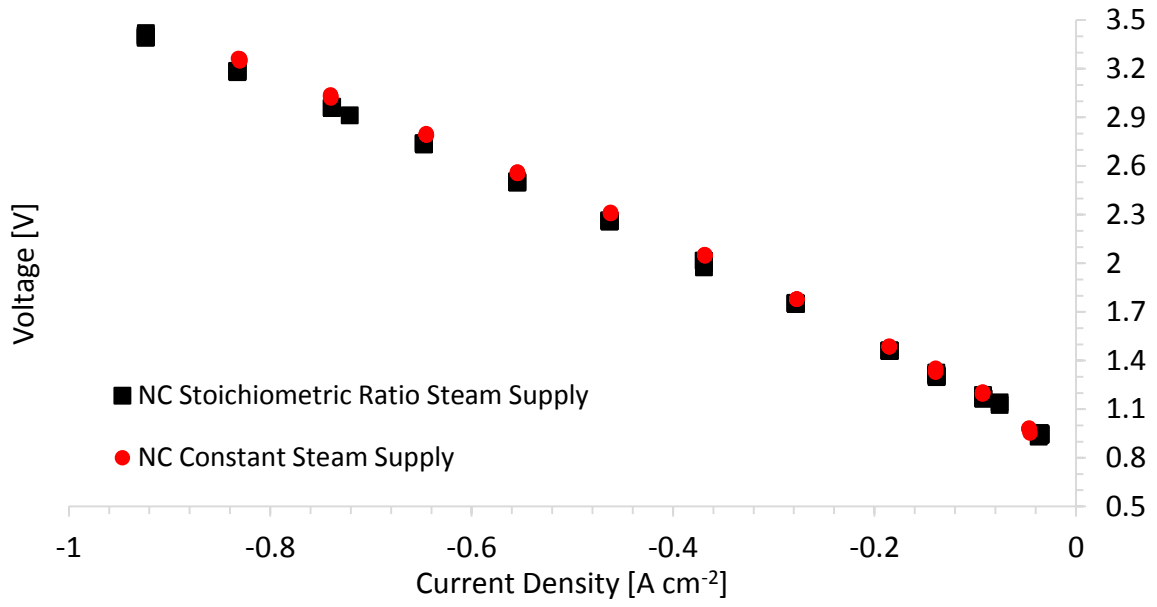

Figure 4.8: Polarization comparison of constant steam supply and supply at a stoichiometric ratio.

The required steam in moles was calculated using Farday's law (assuming all electrons were consumed in the reduction reaction) and multiplied by three to give the desired supply of steam, resulting in a steam conversion rate of 33% (an 67% excess of steam). The temperature of the humidifier, and the flow rate of carrier gas were adjusted to supply the desired amount of steam to the cell according to the Antoine equation. After adjustment to the desired steam delivery rate, five minutes were given to allow equilibration of the steam concentration, temperature, and current. For the constant steam supply case, three times the stoichiometric steam supply for a current density of -300 mA cm^{-2} was delivered to the cell for the full polarization measurement.

As expected, at low current densities, the voltage for both cases were very similar, with the constant steam flow case having a voltage 7 mV greater at -90 mA cm^{-2}. As the current density decreased the voltage of the constant steam supply case was seen to increase more than the stoichiometric ratio case. This was due to steam limitation, which decreases the reaction quotient ($p_{H2O}/(p_{H2}\times p_{O2}^{0.5})$) in the Nernst equation leading to an increased voltage. The difference in voltages reached a maximum of 70 mV at a current density of -830 mA cm^{-2}. Although this difference in voltage is significant, adjustment of the rate of steam delivery between each current density adds the possibility of variability between experiments. All subsequent experiments were completed with constant steam supply rates to reduce variability between experiments and simplify the data collection process.

In the literature there are studies where the current was adjusted manually and given time to equilibrate similar to the above tests [3]. However, there were also studies where current or voltage were swept at a constant rate [4-6]. A constant sweep rate reduces potential error caused by variation of current density and equilibration time between experiments with manual adjustment. It also allows for measurements to be preprogrammed for simplification of the experiment (reduction in experimenter time). The comparison of the two methods can be seen in Figure 4.9 below.

Both of these measurements were taken on the same NC with the manual adjustment measurements completed first. It can be seen in Figure 4.9 that the manual adjustment voltage is slightly lower than the potentio-dynamic case.

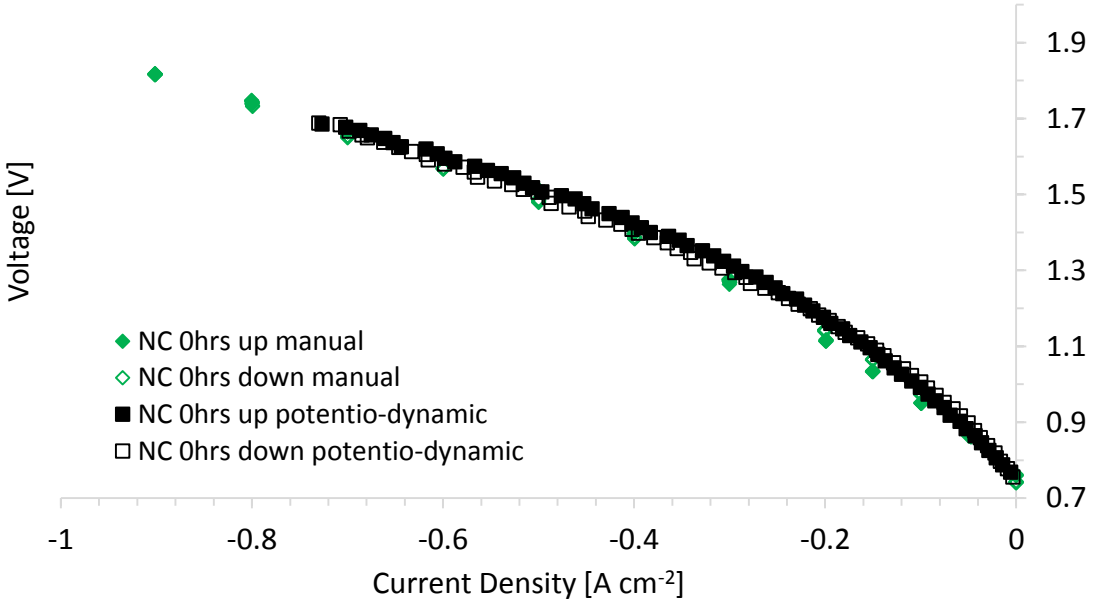

Figure 4.9: Comparison of manual current adjustment and programmed voltage sweep, the manual adjustment was equilibrated for five minutes at each current density and voltage swept at a constant scan rate of 5 mV min^{-1} (potentio-dynamic).

A maximum difference of 26 mV was seen at -200 mA cm^{-2} declining to a 15 mV difference at -700 mA cm^{-2}. Without time to equilibrate at each voltage this result (higher voltage for potentio-dynamic) is expected. However, this difference in voltage is small compared to the 1000 mV difference seen over the course of the polarization and the experimental repeatability is improved by using a programmed scan rate. The remainder of polarization measurements were completed using potentio-dynamic scan with a scan rate of 5 mV min^{-1}.

4.2.2: Reference Cell Testing

Once the measurement parameters had been chosen, more extensive testing was completed on the purchased NCs. This testing consisted of polarization curves, EIS, and short-term electrolysis operation. In Figure 4.10 polarization results for a NC can be seen.

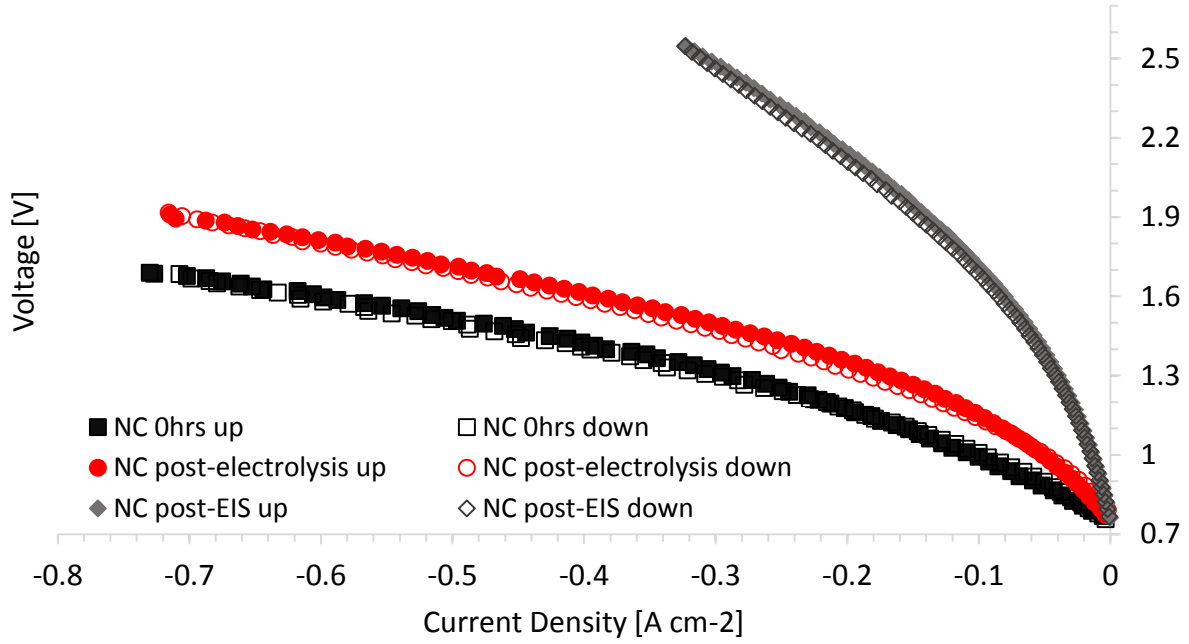

Figure 4.10: Polarization of Nextcell (NC) after 0 and 20 hrs of electrolysis (at a current density of-460 mA cm-2) and after 15 hours of EIS measurements (for experimental parameter testing) with a reduced steam supply.

The zero hours (0hrs) data was collected before any steady-state electrolysis was completed on the cell. Following the initial polarization, a current density of -460 mA cm^{-2} was applied to the cell for 20 hours followed by a second polarization measurement. The voltage was seen to decrease by 18 mV during the first five hours of constant current electrolysis then increase by a total of 37 mV in the following 15 hours. The voltage decrease at the beginning of electrolysis has been attributed to "activation" (conditioning of the electrode) [5-8]. The process of conditioning will be discussed further in the results section. The subsequent increase in voltage is attributed to cell degradation as was discussed in Section 2.4. The performance of the cell after 20 hours of constant current (-460 mA cm^{-2}) electrolysis was noticeably worse

than the initial performance. At a current density of -700 mA cm^{-2} the voltage after 20 hours of electrolysis was 1.9 V compared to 1.65 V before.

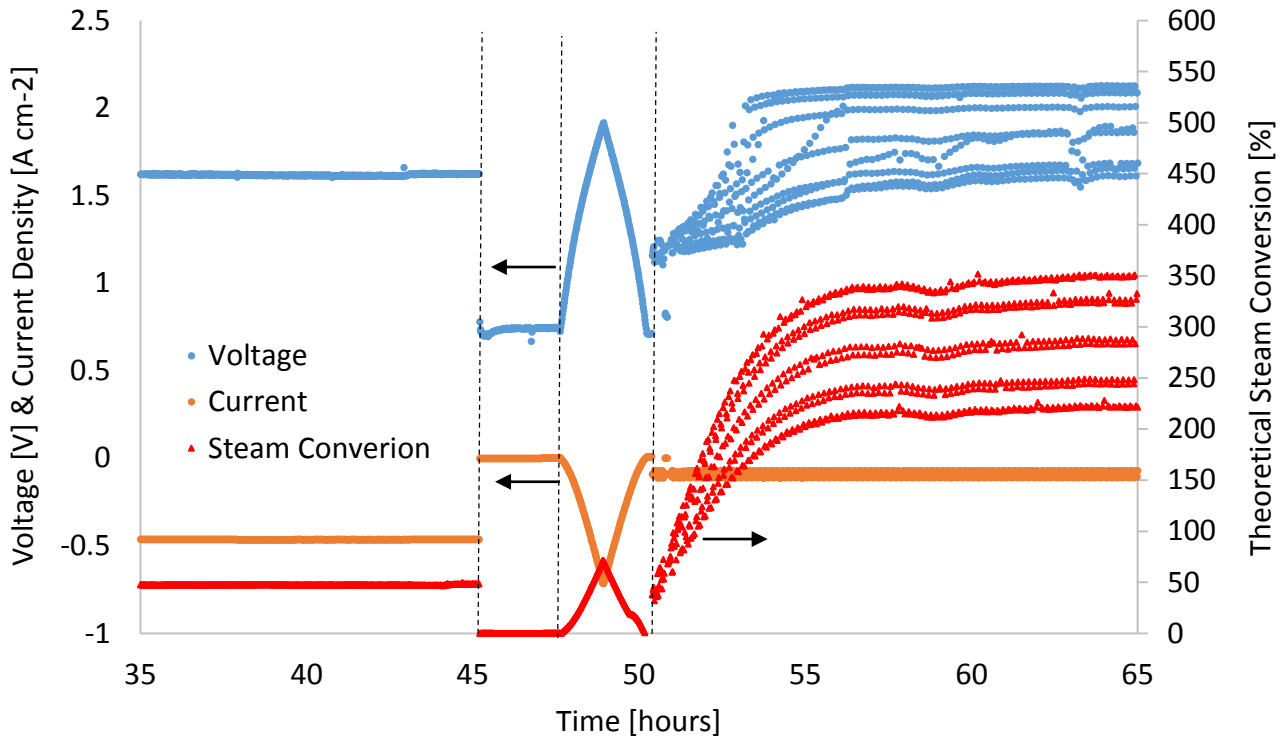

Figure 4.11: Current, voltage and steam conversion for NextCell during electrolysis, polarization, and EIS with steam starvation. Showing constant current electrolysis (-460 mA cm^{-2}) from 35-45 hours, OCV from 45-48 hours, polarization from 48-50 hours, EIS from 50-65 hours.

EIS measurements were completed on the cell with a DC of -90 mA cm^{-2} and an amplitude of -20mA cm^{-2} following the second polarization. During this EIS the humidifier temperature dropped to room temperature due to a restriction in the flow from the circulating heated bath. This reduced temperature lowered the steam supply to $1.43x10^{-5}$ mol min^{-1} instead of the $4.07x10^{-4}$ mol min^{-1} that should have been delivered, leading to steam starvation and a high voltage. This steam starvation and high voltage caused significant cell degradation, negatively affecting cell performance.

The increase in voltage during EIS can be seen to start after the 50 hour mark in Figure 4.11. The correlation of the increase in voltage to the increase in steam conversion rate is evident in this figure. The significant cell degradation led to a maximum voltage of 2.55 V at a current density of -323 mA cm^{-2} during the polarization curve taken after the EIS, once the steam supply had been corrected (Figure 4.10). Before the EIS during steam starvation a voltage of 1.53 V was recorded at -326 mA cm^{-2}, roughly 1 V lower then after the steam starvation event during EIS.

4.3: Results

SOECs with anodes prepared by spray deposition were tested, and compared to the purchased NCs. All cells with prepared anodes that were tested had the same cathode and electrolyte as the NCs. Cells with anodes of different thicknesses and morphologies were seen to have significantly varied results. The section will discuss the potential causes of the varied results, as well as the improved performance seen for anodes with a silver current collecting layer.

4.3.1: Comparison of Purchased SOECs to SOECs with Prepared Anodes

The NCs tested were useful for the selection of the experimental parameters; however, their anodes are very different from those produced for this work. The NCs have a LSM-GDC anode with a LSM current collecting layer (CCL). The prepared anodes are a LSM-YSZ composite and do not have a CCL. The higher ionic conductivity of GDC compared to YSZ (one order of magnitude [9]) and the CCL's ability to distribute electrons over the entire electrode area makes the NC's anode a poor comparison to the prepared anodes. The preparation details for the BL anode can be found in Section 3.2. The LSM-YSZ anode was applied to a half cell with the same electrolyte and cathode as the NC using a spray deposition method. The polarization performance of a cell with a prepared anode is compared to a NC in Figure 4.12.

Compared to the NC the BL cell voltage was seen to be higher at the same current density (even for the NC tested after degradation). The baseline cells were seen to have a much more significant hysteresis between the polarization curves of increasing and decreasing current (labelled up and down). The hysteresis is attributed to the anode because that was the only difference between the cells.

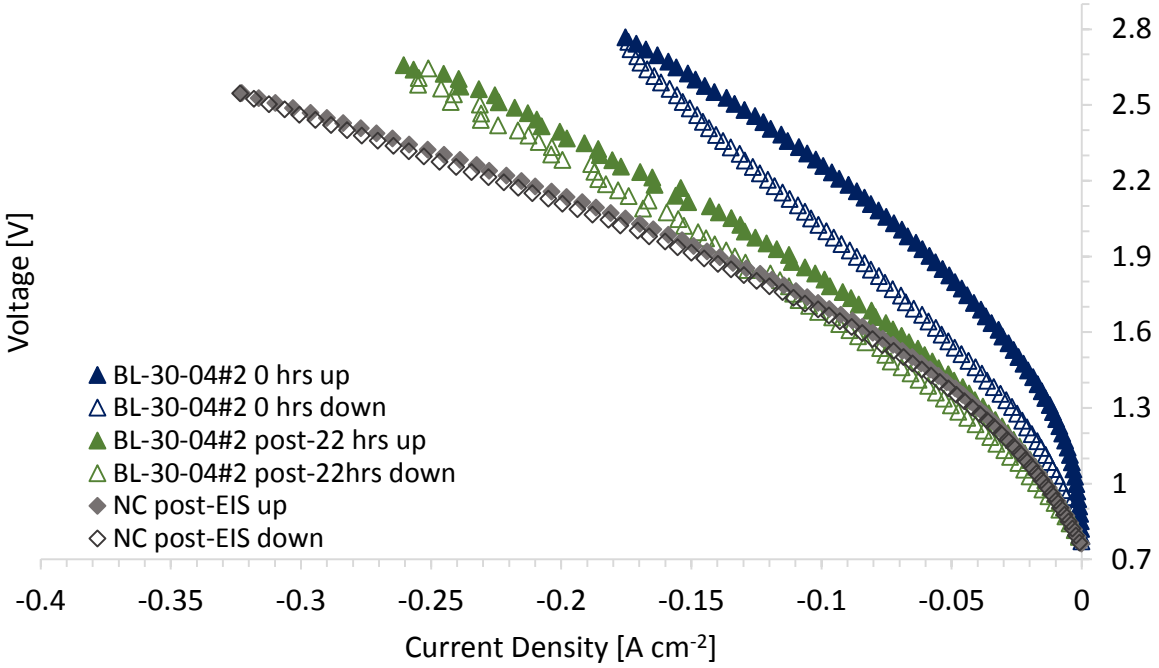

Figure 4.12: Polarization comparison of NextCell and prepared baseline anode cell.

Hysteresis during electrolysis polarization curves has been reported elsewhere in the literature [3-6]. The hysteresis was attributed to joule heating (heat produced from electrical resistance) in two of these studies [3, 5]. The joule heating is believed to increases the transport properties of the anode improving performance. In this work using the thermocouple in the anode chamber (located 10 cm from the anode) the temperature was seen to fluctuate by a maximum of 1 °C during the polarization measurements where hysteresis was seen. Hysteresis was even seen during tests where the temperature was lower during decreasing current density than increasing current density, suggesting the change in temperature at the

thermocouple was not related to the hysteresis. A thermocouple directly beside the cell would be much more useful for studying the temperature changes during testing and should be used in future tests.

Another potential cause for the hysteresis is the variation of species concentrations in the electrode, leading to increases in concentration overpotential. When the current is increased more reactant is consumed and more product is formed at the TPB locations than at a lower current (according to Faraday's Law), leading to a higher concentration overpotential. As discussed in Section 2.2 the concentration overpotential results from the concentration difference between the TPB and reactant source (O^{2-} concentration at the electrolyte interface) and product sink (current collector for e^- and gas channel for O_2 gas). After the current is increased the transport rates must increase to return the anode to steady state (rate of consumption or production equal to conduction or diffusion rate). In an anode with slow oxygen diffusion a steady state as quickly as the current is increased, unless the rate of current increase is sufficiently decreased. If steady state is not reached during increasing current and is reached during decreasing current the oxygen gas concentrations at the TPB, and therefore the concentration overpotential, will be greater during increasing current. A schematic representing the changes in product and reactant concentrations can be seen in Figure 4.13.

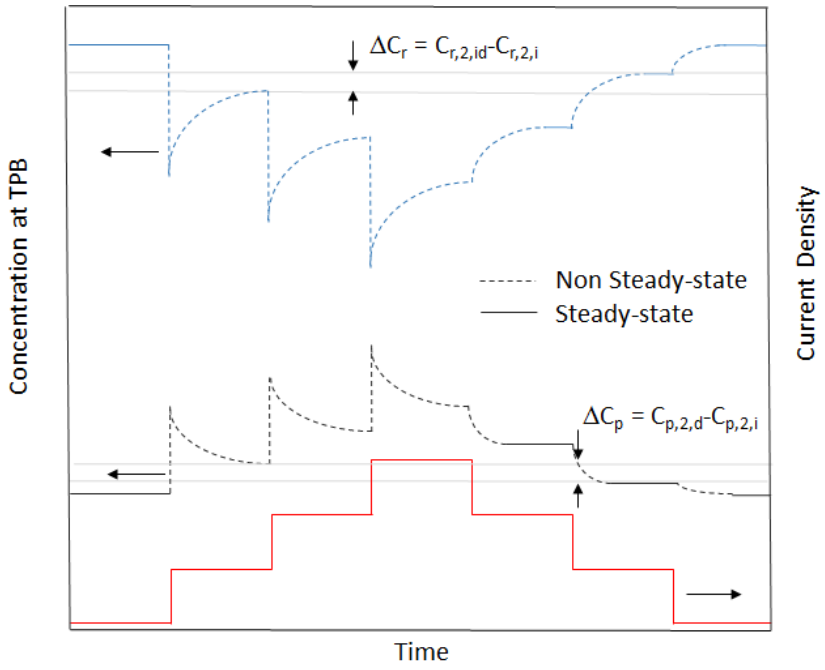

Figure 4.13: Schematic representation of product and reactant concentrations at the TPB in an anode during a polarization measurement. The exponential change in concentration depends on the rates of diffusion and conduction. The ΔC terms represent the difference in concentration between increasing and decreasing values of a certain current density.

The time for an anode system to reach steady state is dependent on the rate of diffusion or conduction (the exponential sections in Figure 4.13). In this study all polarization measurements were completed at the same scanning rate, therefore its effect on hysteresis is not known. In future studies polarization curves should be taken at multiple scan rates to understand if the hysteresis is caused slow adjustment to a new steady state, or another time related cause.

Hysteresis observed during polarization measurements in another study has been associated with oxygen partial pressure equilibration in the anode pores [5]. There has been no connection of polarization hysteresis in SOECs, however, to limitations of ionic or electronic conduction in the literature. The hysteresis and performance improvements seen in prepared anodes will be investigated further in the remainder of this chapter.

4.3.2: Polarization and Short Term Electrolysis Testing of SOECs with Prepared Anode

Anodes produced with the same batch of ink and the same spraying parameters were tested under a combination of polarization, EIS, and short term electrolysis conditions. In polarization measurements before any constant current electrolysis was completed two of the cells prepared with this ink formulation (BL-30-04#2 and BL-30-04#3) can be seen to have similar performance during the decreasing current measurement.

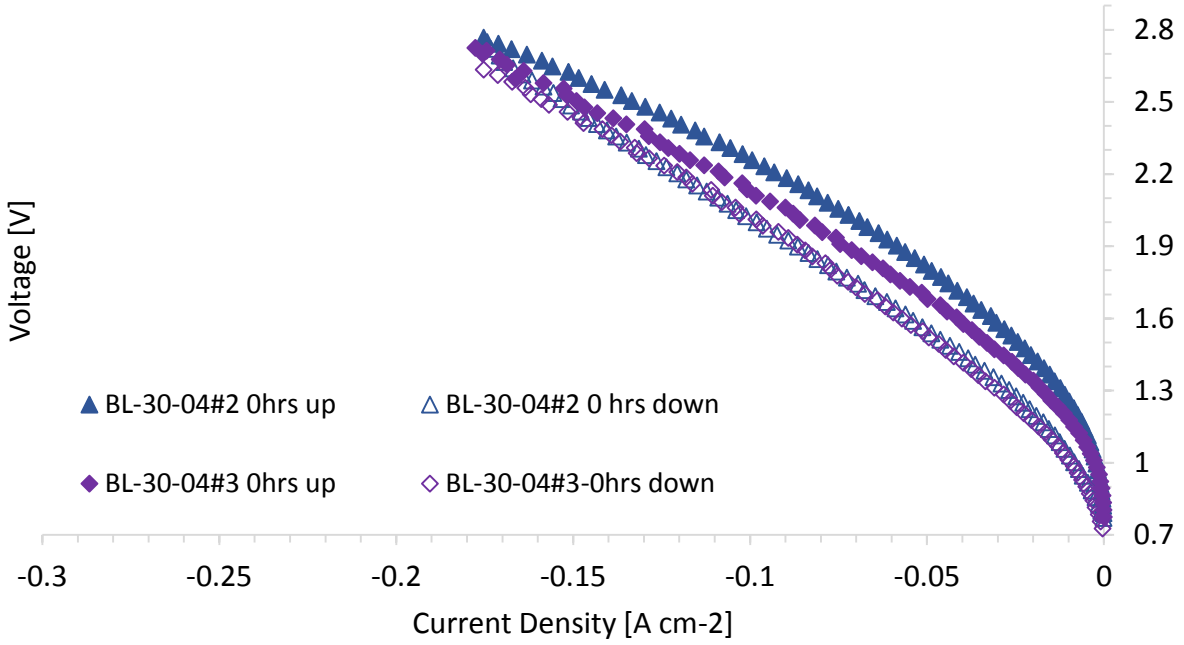

Figure 4.14: Polarization for three baseline cells produced with the same ink batch and spraying parameters, spray pulse, 0.2 s; pin height, 0.35 mm; nozzle height, 70 mm; and air flow rate, 9.5 LPM.

For increasing current; however, the voltage for BL-30-04#3 is noticeably lower than that of BL-30-04#2. To investigate the causes of this performance variation, SEM images of the electrodes were taken after testing and can be seen in Figure 4.15.

Inspecting the SEM images of the BL-30-04#2 and BL-30-04#3 cells the thicknesses of the two anodes are seen to be the most significant difference. The thicknesses were measured with ImageJ software, given as a mean ± a standard deviation based on nine measurements. Cell BL-30-4#3 had a thickness of

3.18 ± 0.46 µm, while cell BL-30-04#2 had a thickness of 17.64 ± 0.52 µm. They major difference between the two cells (greater than a factor of 5) was caused by the different volume of ink in the spray cup. The importance of ink volume in the cup is discussed in more depth in Section 3.3.

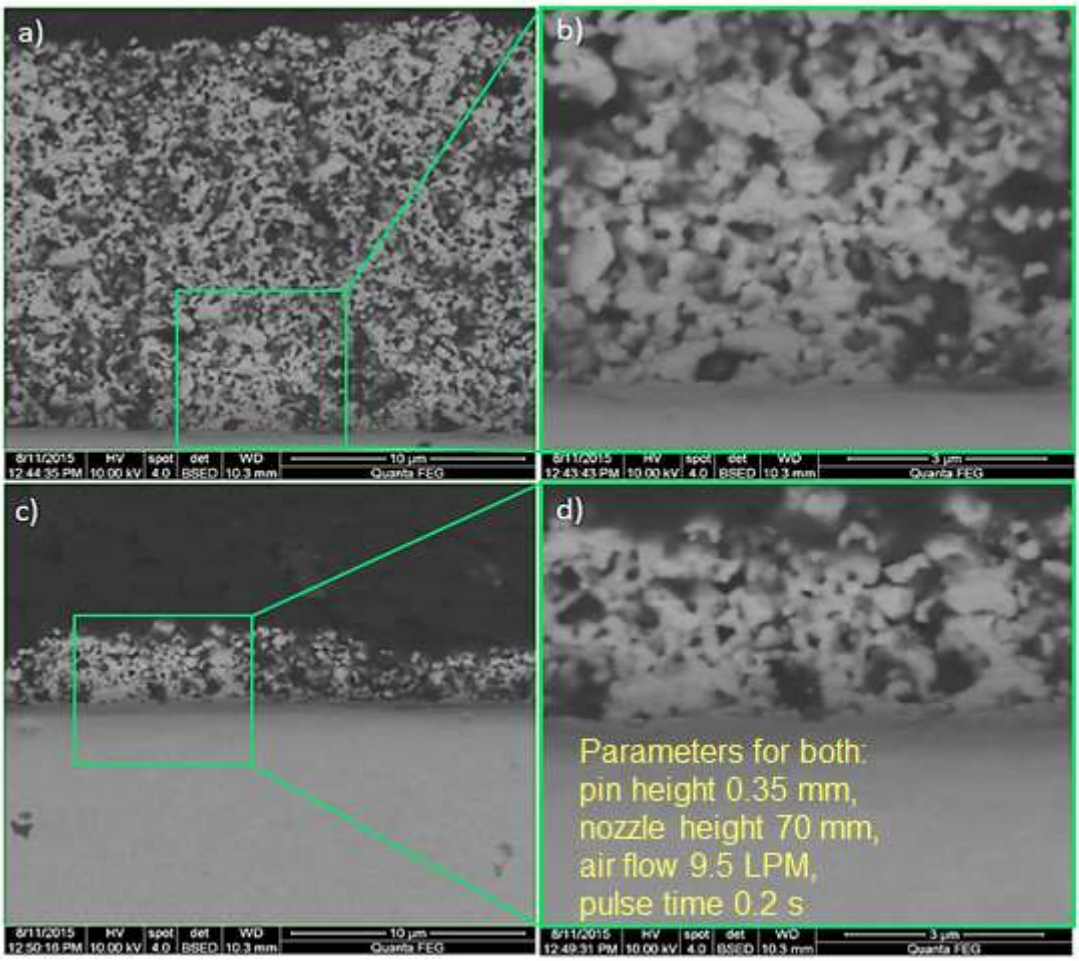

Figure 4.15: SEM comparison of baseline cell morphologies (a-b) cell BL-30-04#2, thickness 17.64 ± 0.52 µm; (c-d) cell BL-30-04#3, 3.18 ± 0.46 µm.

The longer oxygen diffusion pathway and greater hysteresis of the thicker anode supports the hypothesis that the hysteresis is caused by oxygen partial pressure equilibration. In the future, the importance of oxygen partial pressure equilibration could be studied by testing with sweep gases of varying oxygen concentrations. The differences in cell performance cannot be reliably related to the particle size

because the bulk area of the electrode (area that is not interface or surface) is too small to be statistically relevant.

After the initial polarization curve the BL-30-04#2 cell was left at OCV for 12 hours to allow equilibration. Following equilibration an electrolysis current of -30 mA cm^{-2} was applied for a total of 3.5 hours including EIS measurement with an amplitude of 10 mA. The cell was left at OCV to equilibrate for 80 hours and then operated under a constant current density of -200 mA cm^{-2} for 22 hours. In the polarization curves collected for cell BL-30-04#2 the current density at 2.6 V was seen to improve from -156 mA cm^{-2} (0 hours) to -295 mA cm^{-2} after the 3.5 hours of current application. After 22 hours of electrolysis the performance was seen to decrease slightly from the second polarization curve, with a current density of -251 mA cm^{-2} at a voltage of 2.6 V. Both of the polarization curves taken after electrolysis operation had a reduced hysteresis in comparison to the zero hours case as can be seen in Figure 4.16.

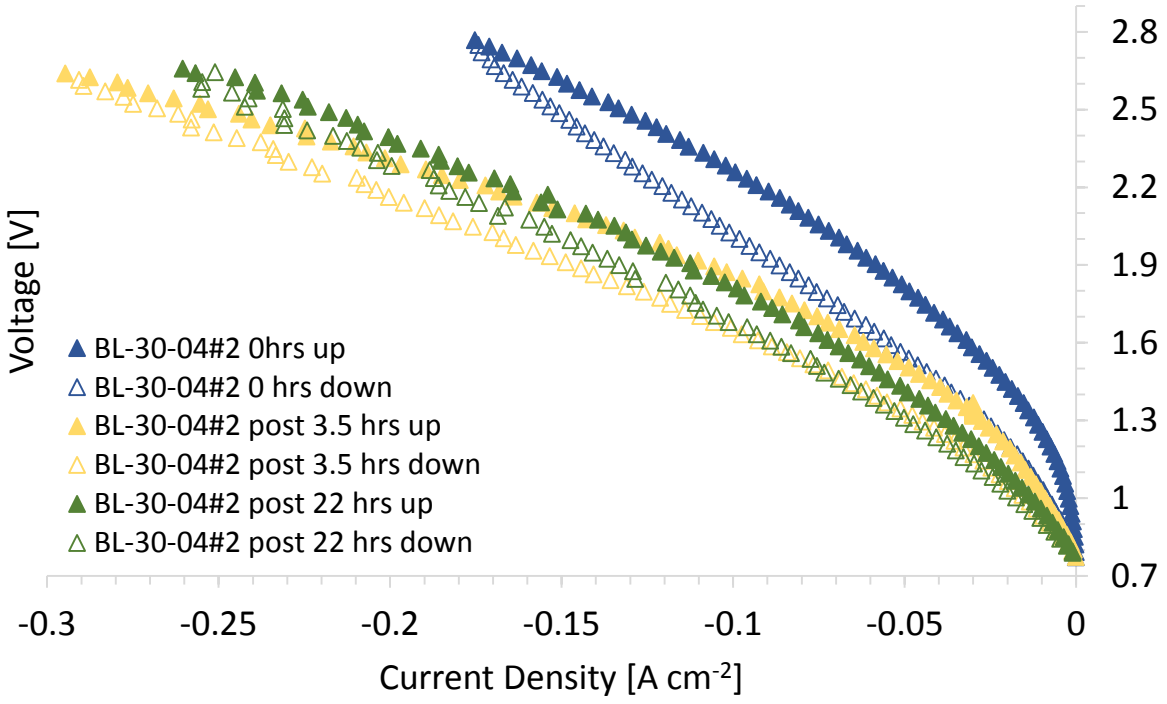

Figure 4.16: Polarization curves for cell BL-30-04-#2 showing performance improvement after electrolysis.

The voltage and current behaviour over time for the first two polarization curves can be seen in Figure 4.17. In this figure from 0 to 3 hours the cell was still below operating temperature (no OCV), from 3 to 5 hours the voltage was seen to decrease as the furnace temperature was increasing. During the first electrolysis (22 to 25 hours) the voltage was seen to decrease from 1.5 to 1.32 V, while a current density of -30 mA cm^{-2} was applied for 3.5 hours, including impedance measurement (AC amplitude of 10 mA cm^{-2}) around 25 hours.

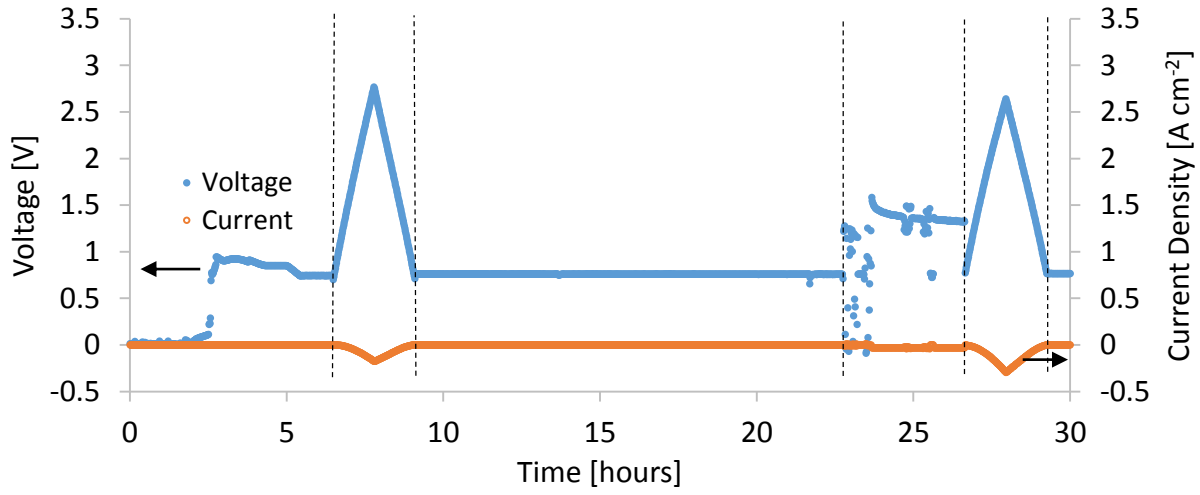

Figure 4.17: Current and voltage data for the first 25 hours of operation for cell BL-30-04#2. 3-5 hours increasing to operating temperature, 7-9 hours polarization, 9-22 hours OCV, 22-28 hours EIS and constant current electrolysis (-30 mA cm^{-2}), 27-29 hours polarization.

During the second constant current application (-200 mA cm^{-2} for 22 hours) the voltage was seen to decrease sharply from 3.1 V to 2.6 V in the first hour, as can be seen in Figure 4.17. The voltage decreased further to 2.1 V over the next 15 hours.

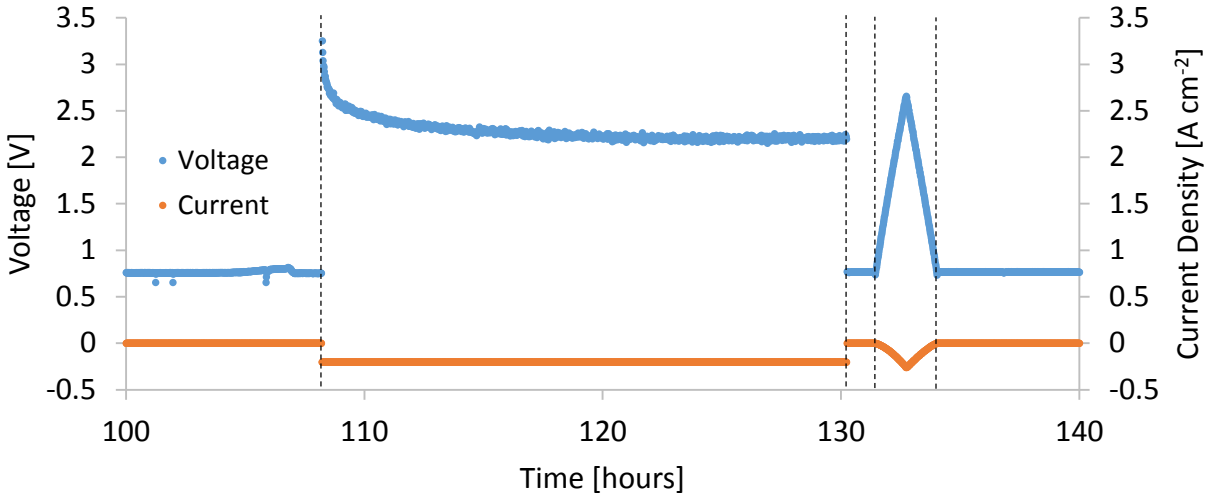

Figure 4.18: Short term electrolysis and polarization of cell BL-03-04#2 (22hours at a current density of -200 mA cm^{-2}). 100-108 hours OCV, 108-130 constant current electrolysis (-200 mA cm^{-2}), 130-131 OCV, 131-133 Polarization, 133-140 OCV.

These decreases in voltage over time during electrolysis are attributed to conditioning of the anode. Other instances of SOEC anode conditioning during electrolysis operation have been reported in the literature [5-8]. In these instances in literature the conditioning occurred during the first 1-30 hours of operation. Increased oxygen vacancies in the LSM lattice and enhanced oxygen transport are proposed as the causes of improved performance in a study by Liang *et al.* [7]. In another paper by Chen *et al.* [8] reasoned that enhanced surface diffusion of oxygen species is responsible for the improvements in performance based on EIS completed throughout electrolysis. The cell conditioning was explained as temperature equilibration of the cell in a study by Schefold *et al.* [5]. In the experiments completed in this work no usable EIS data could be collected and no trend of increasing temperature (measured by the thermocouple in the anode chamber) during electrolysis was seen.

In the polarization curve taken after 22 hours of electrolysis operation, Figure 4.16, the performance had decreased slightly compare to the polarization measurement after 3.5 hours of -30 mA cm^{-2} current application but was still much better than the zero hours performance.

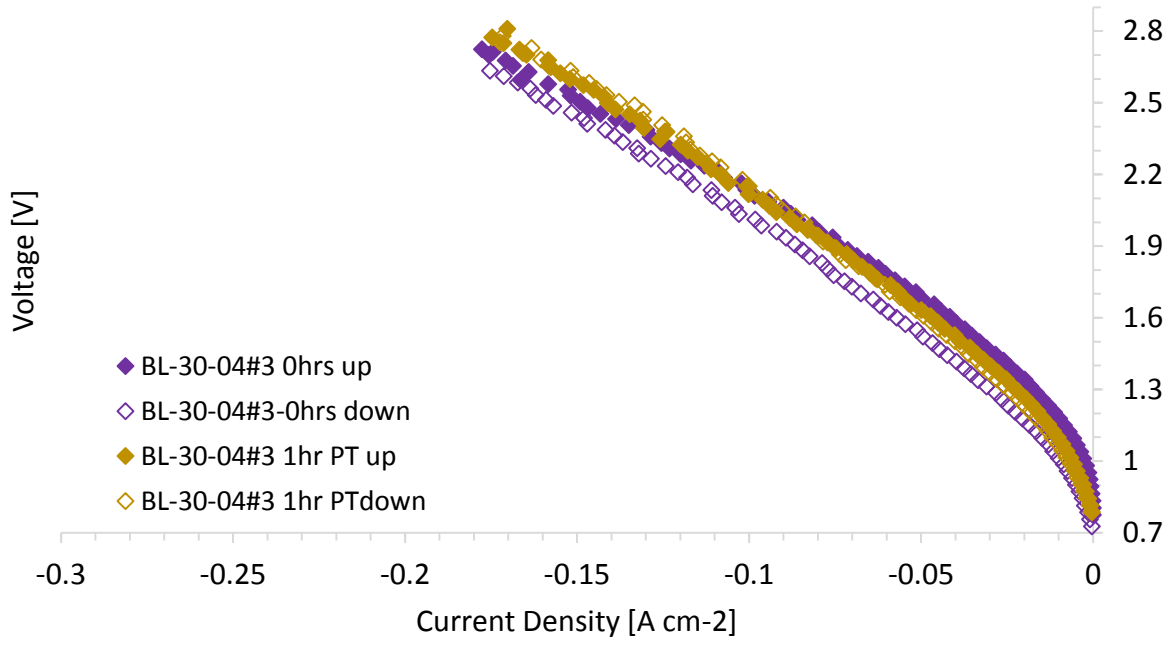

Figure 4.19: Polarization curves for BL-30-04#3 cell taken before and after an hour of electrolysis operation.

As seen in Figure 4.14 the hysteresis for the BL-30-04#3 cell at zero hours was much lower than that of the BL-30-04#2 cell. Correspondingly, in short term electrolysis the voltage of the BL-30-04#2 cell was not seen to decrease (no conditioning), instead it was seen to increase (Figure 4.20).

A polarization curve taken after one hour of -30 mA cm^{-2} current application, Figure 4.19, shows a lower voltage (than the increasing current curve of the zero hours polarization measurement) until about -120 mA cm^{-2} after which, the voltage is higher than the zero hours case. The second polarization curve also shows much less hysteresis than the zero hours case, a maximum of 23 mV.

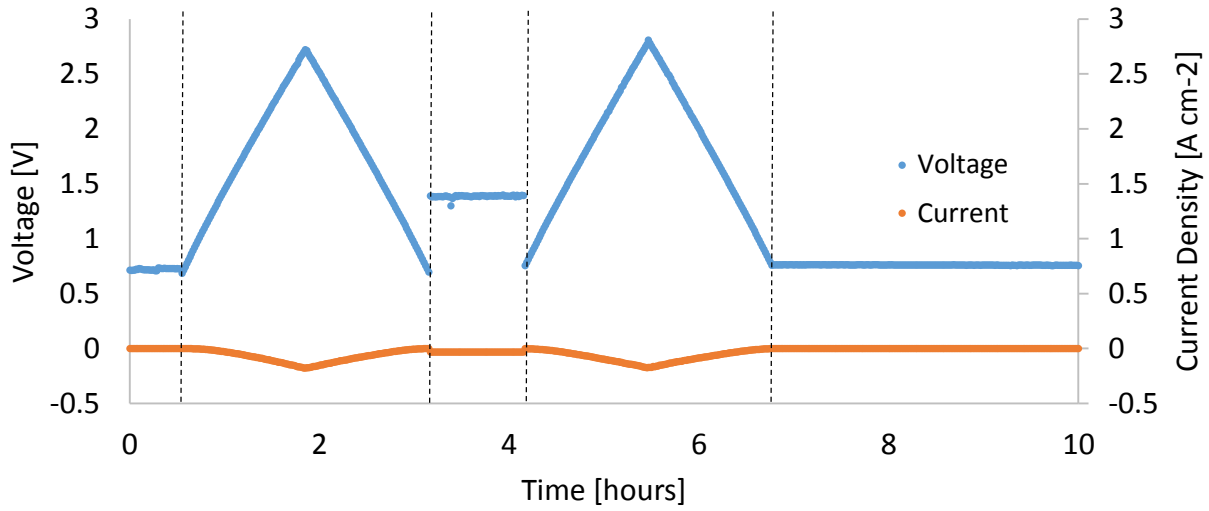

Figure 4.20: Polarization and Short Term Electrolysis of Cell BL-30-04#3. 0-1 hours OCV, 1-3.2 hours polarization, 3.2-4.2 hours OCV, 4.2-6.5 hours polarization, 6.5-10 hours OCV

The partial pressure of oxygen in the thinner anode (cell B-30-04#3) will equilibrate more quickly than the thicker anode because it has a shorter diffusion length. The anodes lower porosity (greater YSZ fraction) will also improve the ionic conductivity, allowing the ionic concentration to equilibrate more quickly. The hypothesis that conditioning is caused by the equilibration of species (oxygen gas or oxygen ions) is supported by the fact that no conditioning was measured, suggesting that it occurred to rapidly to be recorded.

The conditioning during electrolysis operation seen in this work and others is hypothesized to be caused by the same phenomenon responsible for the hysteresis seen during electrolysis polarization. Either both results were seen or neither was seen in the experiments completed for this work. If theses phenomena are related to oxygen partial pressure equilibration as has been hypothesized, they could give insight into oxygen transport in an operating SOEC cell. As has been discussed in Section 2.4, internal oxygen partial pressure is thought by many to be a cause of anode degradation and delamination. A strong understanding of oxygen transport limitations would therefore be beneficial to preventing SOEC degradation.

Both hysteresis during polarization and conditioning during electrolysis have also been seen in the published literature; however, no connection between them has been made. Schefold *et al.* [5] associated

hysteresis with equilibration of oxygen partial pressure and the cell conditioning with temperature equilibration. Hauch *et al.* [6] presented both phenomena but did not hypothesize the causes or connect the two. In other studies showing electrolysis polarization hysteresis no constant current electrolysis results were presented [3]; or the scale was so large, over 5000 hours, and the voltage response was so noisy that the period where conditioning would occur could not be seen [4]. In the latter case it is expected that the conditioning would have been small based on the small hysteresis, roughly 15 mV only seen at current densities between -800 and -1100 mA cm^{-2} [4]. In the other literature that presented conditioning at the beginning of electrolysis operation; either no polarization was completed or the polarization was only in one direction [7, 8].

A major difference between the prepared anodes and those of the NCs (a possible reason for the NCs better performance) is the current collecting layer (CCL). To simulate the CCL a silver paste was applied to a prepared anode and the platinum current distributing mesh was attached to the paste. The cell, paste, and mesh were heated to 110 °C for one hour to harden the paste and ensure attachment.

The polarization behaviour of the cell with silver paste acting a current collector, compared to the prepared cells without the paste can be seen in Figure 4.21. The cell with the current collector has a voltage of 1.87 V at a current density of -300 mA cm^{-2}, compared to a voltage of 2.64 V at -295 mA cm^{-2} for the best performing cell without silver paste and maximum voltage of 2.7 V at a current density of -176 mA cm^{-2}. This voltage of the cell with the CCL is still higher than the purchased NC which had a voltage of 1.3 V at a current density of -308 mA cm^{-2}.

Prior to the polarization of the cell with silver paste short term electrolysis and EIS were completed on the cell. No decline in voltage (conditioning) was seen during electrolysis. Also minimal hysteresis is visible in the polarization plot other than that seen near the disruption in electrical connection around 1 V.

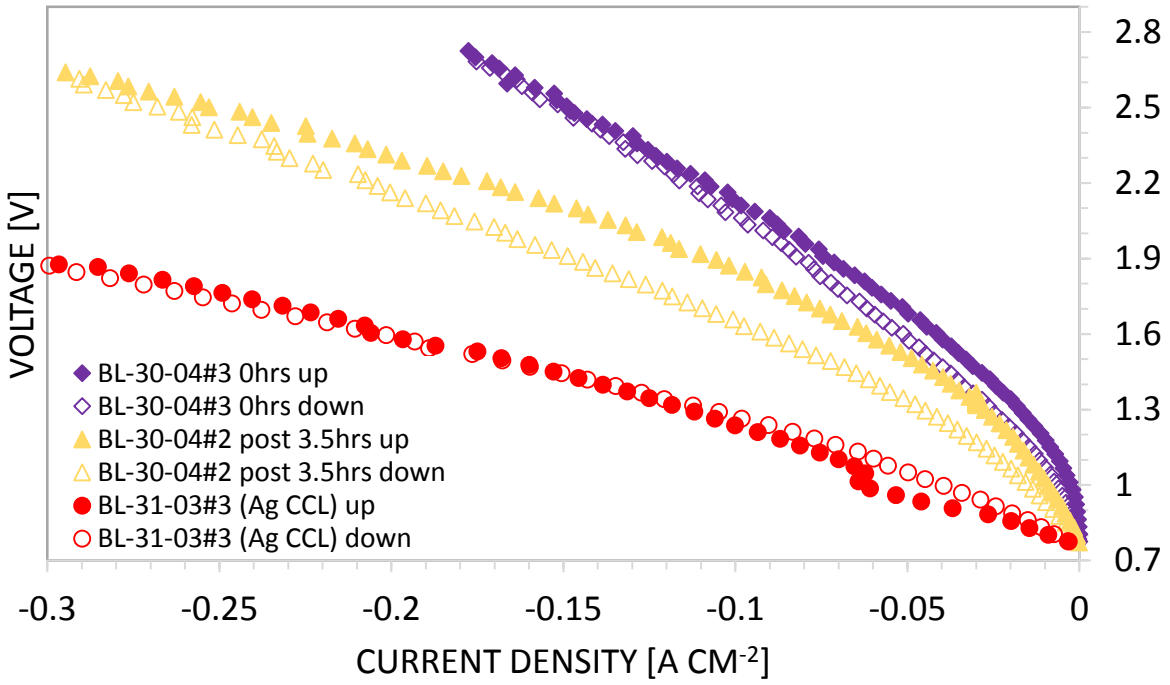

Figure 4.21: Polarization of BL cell with silver paste acting as a CCL compared to cells without a CCL , the discontinuity seen for the BL-31-03#3 up at 1 V was caused by a disruption to the electrical connections between the power supply and the testing station

The thicknesses and particle sizes of the three anodes varied significantly. The thicknesses of the anode with the silver CCL (7.34 ± 2.91 μm) was greater than the BL-30-04#3 anode (3.18 ± 0.46 μm) but smaller than that of the BL-30-04#2 anode (17.6 ± 0.52 μm). The removal of the platinum mesh during preparation for SEM is thought to have caused the non-uniform thickness by separating portions of the anode. The mean particle sizes (measured using ImageJ) were found to be 0.86 ± 0.74 μm for anode BL-30-04#2, 0.81 ± 0.54 μm for anode BL-30-04#3 (the confidence in this value is low because of the small sample size used), and 0.70 ± 0.41 μm for anode BL-31-03#3.

The improved performance of the cell is attributed to the silver paste acting as a current collector. The different thickness of the anode with the silver CCL is not assumed to be responsible for the improved performance compared to the cells without the CCL. The thickness of the anode with the CCL is between the thicknesses of the two anodes whose cell performance are both worse the cell with the CCL. The smaller

particle size may have also been a factor as it has been shown to increase TPB length in a modelling study of composite electrodes [8].

The smaller hysteresis in the BL-31-03#3 cell compared to the BL-30-04#2 cell is thought to be the result of the smaller thickness (faster diffusion) of the anode, as was the case for cell BL-30-04#3. The CCL may have aided in preventing hysteresis by reducing the resistance, and therefore any joule heating occurring in the anode. No further studies could be completed on cells of different thicknesses and morphologies with silver paste acting as a current collector as a result of time limitations on this work.

4.3.2: Impedance Spectroscopy

In order to better understand the changes occurring in the SOECs an attempt to complete EIS measurements was made. The electrical connections in the ProboStat™ testing station used for these measurements were very sensitive and the humidity in the cathode chamber interfered with the lead connections. With this setup SOFC operation under dry conditions gave smooth EIS data in comparison to measurements taken during SOEC. These factors prevented the collection of reliable and useful EIS data for SOEC operation.

4.4: Conclusions

An SOFC button cell testing apparatus (ProboStat™) has been modified to test cells in electrolysis operation. An adjustable membrane gas humidifier has been developed to provide steam for electrolysis, this is the first membrane gas humidifier used with a ProboStat™. To ensure controlled supply of humidified gas without condensation, the ProboStat™ has been adjusted with resistance heaters, insulation, and additional thermocouples. After investigation of scan and steam delivery rates an experimental method for testing SOECs has been prepared. Steam limitation was shown to increase voltage during electrolysis.

Polarization measurements completed under a constant voltage sweep rate were shown to give a higher voltage than manual adjustment with time allowed for equilibration.

Different levels of hysteresis during polarization, and conditioning during electrolysis operation were seen for cells with anodes prepared by controlled spray deposition. A correlation of the two phenomena has been made, based on their related behaviour. Future testing should study cells using various scan rates to determine if hysteresis is related to reaching a steady-state during measurements. The use of silver paste as a current collector improved performance of prepared anodes. A system with the ability to more stably measure EIS and measure the temperature directly adjacent to the anode is needed for further investigation of the conditioning and hysteresis mechanism.

4.5: References

[1]Torrell M, García-Rodríguez S, Morata A, Penelas G, Tarancón A. Co-electrolysis of steam and CO_2 in full-ceramic symmetrical SOECs: a strategy for avoiding the use of hydrogen as a safe gas. Faraday Discuss. 2015;182:241–55.

[2] Cumming DJ, Elder RH. Thermal imaging of solid oxide cells operating under electrolysis conditions. Journal of Power Sources. 2015 Apr 15;280:387–92.

[3] Chauveau F, Mougin J, Bassat JM, Mauvy F, Grenier JC. A new anode material for solid oxide electrolyser: The neodymium nickelate Nd2NiO4+δ. Journal of Power Sources. 2010 Spring;195(3):744–9.

[4] Schefold J, Brisse A, Tietz F. Nine Thousand Hours of Operation of a Solid Oxide Cell in Steam Electrolysis Mode. J Electrochem Soc. 2011 Jan 1;159(2):A137–44.

[5] Schefold J, Brisse A, Zahid M. Electronic Conduction of Yttria-Stabilized Zirconia Electrolyte in Solid Oxide Cells Operated in High Temperature Water Electrolysis. Journal of the Electrochemical Society. 2009 Aug 1;156(8):B897–904.

[6] Hauch A, Jensen SH, Ramousse S, Mogensen M. Performance and Durability of Solid Oxide Electrolysis Cells. J Electrochem Soc. 2006 Sep 1;153(9):A1741–7.

[7] Liang M, Yu B, Wen M, Chen J, Xu J, Zhai Y. Preparation of LSM–YSZ composite powder for anode of solid oxide electrolysis cell and its activation mechanism. Journal of Power Sources. 20090515;190(2):341–5.

[8] Chen K, Jiang SP. Failure mechanism of (La,Sr)MnO3 oxygen electrodes of solid oxide electrolysis cells. International Journal of Hydrogen Energy. 2011 Aug;36(17):10541–9.

[9] Manoj K. Mahapatra, Singh Prabhakar. Fuel cells: Energy conversion technology. In: Future Energy: Improved, Sustainable and Clean Options for Our Planet. Second ed. Elsevier; 2014. p. 511.

[10] Gaweł DAW. The Development of a Coupled Physics and Kinetics Model to Computationally Predict the Powder to Power Performance of Solid Oxide Fuel Cell Anode Microstructures. [Kingston, Canada]: Queen's University; 2013.

Chapter 5: Conclusions and Recommendations

The goal of this research was to increase understanding of the processes leading to solid oxide electrolysis cell (SOEC) anode delamination. To reach this goal, a method for preparing and spraying inks to produce uniform SOEC anodes with varied morphologies was developed. The importance of sonication and deposition rate on anode morphology were observed. Cells fabricated by spray deposition were analyzed, showing that particle size distribution and porosity were adjusted by varying the ink deposition rate. Techniques for reliable estimation of particle size distributions and porosity using electron microscopy and image analysis software were established for anode characterization.

A ProboStat^{TM} SOFC button cell test station was modified to allow reliable testing in electrolysis operation. Numerous operating challenges were overcome resulting in stable operation using a membrane humidification system, the first use of membrane humidification system with the ProboSatat^{TM} testing system reported in the literature. An experimental method for testing SOEC button cell performance was successfully developed using commercially available electrolysis cells. The lack of current collecting layer (CCL) on the in house prepared anodes prevented direct comparison with commercially available cells. The importance of a CCL was demonstrated using a silver paste acting as a CCL on prepared anodes. Anodes of varied thicknesses were tested showing different performance. A thicker anode showed greater hysteresis during polarization measurements a thinner anode, with greater voltage during increasing current. The thicker anode also showed significant decrease in voltage over time during constant current electrolysis, while the thinner anode showed no decrease in voltage.

The limited number of prepared anodes was not sufficient to claim control of morphology in this work. In future studies using the spraying parameter range found to be ideal during this thesis (Air flowrate = 9.5 LPM, pulse time = 0.2 s, pause time = 1.0 s, nozzle height = 70 mm, and pin height = 0.35 mm, cup volume = 6.0 mL), should be used to produce 10 anodes to ensure repeatability of anode morphologies. In

addition 10 anodes should be produced with deposition rates on either side of that range, by using cup volumes of 5.5 and 6.5 mL, in order to improve the controllability of porosity and particle size. The 10 anodes produced using each of these spraying parameters should be split into two groups with spray times of 45 and 75 min, resulting in anodes of different thicknesses. Assuming a high level of repeatability during spraying, six different groups of anodes will be prepared. The six groups will consist of three distinct morphologies (porosity and particle size distribution, produced by varying the deposition rate) with two thicknesses for each morphology, due to the varied deposition time. These six groups will allow the effect of thickness on performance to be studies, and effect of porosity and particle size on performance to be studied.

During testing of these prepared cells anode sweep gases from low to high oxygen concentrations (0.1 % - 100%) should be used during polarization and long term constant current electrolysis. The different concentrations during polarization measurements will show whether or not oxygen partial pressure is responsible for the hysteresis seen. Using different oxygen concentrations during long term electrolysis testing will provide information on the role of oxygen partial pressure in anode degradation and delamination.

Electrical impedance spectroscopy measurements were not possible in the ProboStat™ setup due to the sensitivity of electrical leads and the effect of humidity. Future experiments should be completed using a ProboStat™ with electrical leads insulated from the humid environment of the cathode chamber. The ability to reliably complete EIS has the potential to provide information on the individual resistances changing during polarization and long term electrolysis testing. Additionally any further tests should include a porous LSM deposited on the anode, acting as a CCL, for better comparison to commercially available cells. In the future anodes with various particle size distributions and the same thickness could be studied to better understand the importance of particle size on performance.